Doctoral Thesis

Development of nanoporous gold films for electrochemical applications

Keon-U Lee

Department of Materials Science and Engineering

Graduate School of UNIST

2020

Development of nanoporous gold films for electrochemical applications

Keon-U Lee

Department of Materials Science and Engineering

Graduate School of UNIST

Development of nanoporous gold films for electrochemical applications

A thesis/dissertation
submitted to the Graduate School of UNIST
in partial fulfillment of the
requirements for the degree of
Doctor of Philosophy

Keon-U Lee

6. 15. 2020 of submission
Approved by

_____

Advisor
Hyung-Joon Shin

Development of nanoporous gold films for electrochemical applications

Keon-U Lee

This certifies that the thesis/dissertation of Keon-U Lee is approved.

6/15/2020 of submission

signature

Advisor: Hyung-Joon Shin

signature

Zonghoon Lee

signature

Jung-Woo Yoo

signature

Sang Hoon Kim

signature

Ji Young Byun

CONTENTS

LIST OF FIGURES AND TABLE

ABSTRACT

Development of nanoporous gold films for electrochemical applications

Keon-U Lee

Department of Materials Science and Engineering

Ulsan National Institute of Science and Technology (UNIST)

Nanoporous gold thin films on various substrates were prepared by co-sputtering method and used for electrochemical applications. Binary gold alloy was made with less noble element which was selectively dissolved from the alloy to make nanoporous structures. The composition of alloy was easily controlled by adjusting each power of targets. The size of ligaments and holes were under ~100 nm. We used conventional three electrode system, nanoporous gold film, Ag/AgCl (3 M NaCl), and platinum wire were used as working electrode, reference electrode, and counter electrode, respectively. The cyclic voltammetry and chorono amperometry were employed. We made nanoporous gold for amperometric aniline sensor, polyaniline coated nanoporous gold for supercapacitor, and nanoporous gold palladium for ethanol oxidation reaction.

First, we improved the fabrication process of nanoporous gold thin films. Previously, during the dealloying process, hydrofluoric acid (HF) solution was used for dissolving the Si the sacrificial element. Potassium hydroxide (KOH) solution were used instead of hydrofluoric acid solution due to its safety nature and more environmentally friendly method. For deposition, although silicon substrate is commonly used, glass substrate was chosen for availability and its lower cost. We conducted heat treatment for enhancing the adhesion between glass substrate and films. Furthermore, we used nanoporous gold as amperometric sensor for aniline. Constant voltage was applied to working electrode (nanoporous gold) and 10 μM of aniline were successively added. The current was linearly increased with the concentration of aniline and showed low detection limit (0.5 μM). The reaction was carried in both phosphate buffered saline (PBS) solution and tap water. Our nanoporous gold sensor

exhibited high sensitivity, wide sensing range, and low detection limit.

Secondly, we made polyaniline coated nanoporous gold for supercapacitor. For nanoporous gold, magnesium and acetic acid were used rather than silicon and hydrofluoric acid or potassium hydroxide. Then, polyaniline was uniformly coated on the nanoporous gold by electrochemical method. The electrolyte, concentration of aniline, and electrochemical techniques were optimized for uniform and compact coated polyaniline. The thickness of polyaniline was ~ 10 nm, which is confirmed by transmission electron microscopy (TEM). Our polyaniline-nanoporous gold supercapacitor showed high areal capacitance, fast charge-discharge rates, and good stability.

Thirdly, nanoporous gold palladium was fabricated for ethanol oxidation reaction. The ternary alloy of gold, palladium, and magnesium were made and magnesium from the alloy were dissolved to make nanoporous gold palladium. The magnesium was easily dissolved by diluted acetic acid, an easy and environmentally friendly/safe method. Optimization of the composition and porosity of nanoporous gold palladium were done by adjusting each power of sputtering targets. TEM and energy dispersive x-ray spectroscopy (EDS) results showed gold and palladium are homogeneously distributed and magnesium is almost removed by diluted acetic acid. X-ray diffraction (XRD) and fast Fourier transformation (FFT) data showed that the lattice spacing of nanoporous gold palladium is ~2.3 Å, confirmed that gold and palladium are alloyed. Our nanoporous gold palladium exhibited high current density and great stability toward ethanol oxidation reaction in alkaline media.

Nanoporous structures offer a number of advantages such as large surface area, high stability, and high catalytic activity. The nanoporous structures can be applied to not only gold but also other noble metals (platinum, palladium, etc.) or cheap metals (silver, copper, etc.) as well as bimetallic alloys. Using our co-sputtering method and nanoporous structures, versatile materials could be created for different research fields.

CHAPTER 1
INTRODUCTION

In this thesis, we will introduce the various applications of nanoporous gold using electrochemistry. First, we will address the basic information for understanding of this thesis. In this chapter, will briefly introduce the nanoporous gold, its fabrication methods, and properties. Also, we will address the basic of electrochemistry including electrode kinetics, Nernst equation, etc. Next chapter, we will introduce our equipment which are used in this thesis (sputtering, electrochemical potentiostat, x-ray diffraction, etc.). Finally, we will address our main works; electrochemical sensor, supercapacitor, and fuel cell using nanoporous gold.

1.1 Nanoporous gold

1.1.1 Introduction

Nanoporous gold(NPG) is corrosion derived bulk nanostructured material[1]. It is made from binary gold alloy with less noble element, such as silver or silicon. Immerse the alloy into a corrosive solution for dissolution of less noble element. Since gold is a noble metal, it does not dissolve and diffuses to form three dimensional continuous porous network of ligaments (figure 1.1)[2], which is dealloying process. Depending on the dealloying conditions such as type of corrosive solution or dissolution and diffusion rate, the size of ligaments and pores can be controlled, but typically they are ~ 100 nm. Because of its high surface-volume ratio, high porosity, great stability, and high conductivity, NPG has been widely used in many research fields such as sensor[3, 4], catalyst[5, 6], actuator[7, 8], energy system[9, 10], etc.[11] In this chapter, we will introduce the basic of NPG, fabrication method, and theories.

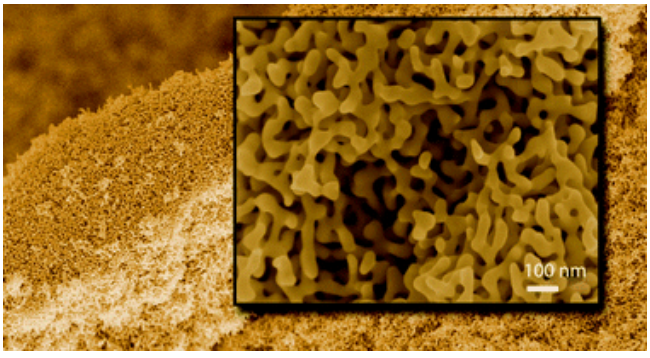

Figure 1.1. NPG from Au-Ag alloy[2]

NPG has many fascinating features as mentioned above, different from normal gold. Then, why the nano-sized gold is special? One important reason is increased surface to volume ratio of the material. The number of neighboring atoms called coordination number (CN) is decreased in surface atoms (figure 1.2) and the low-coordinated atoms are chemically unstable than normal atoms so that they play very important role in chemical reactions. In case of gold, it has face centered cubic (FCC) structure and CN of bulk, terrace, step and kink is 12, 9, 7, and 6, respectively. Every material has surface, however, nano-sized material has high surface to volume ratio. If surface ratio is very high, the influence of surface effect which is based on low-coordinated atoms increases. The NPG has a lot of step and kink sites (figure 1.3)[12].

The low-coordinated atoms enhance the reactivity of metal surfaces. For example, the adsorption and bonding of CO molecules on the gold surface is more easy at the low-coordinated atoms[13]. In case of transition metals, their d-bands are highly affect the activity of the surface because they are the highest electronic states. Generally, the low-coordinated atoms have higher d-band states (kink, step, etc.). Therefore, these low-coordinated atoms more strongly interact with adsorbate than high-coordinated atoms.[14] Not only catalysis effect, nano-sized gold has surface stress effect (actuator)[15], optimal effect (surface plasmon), etc. but they are not covered in this thesis.

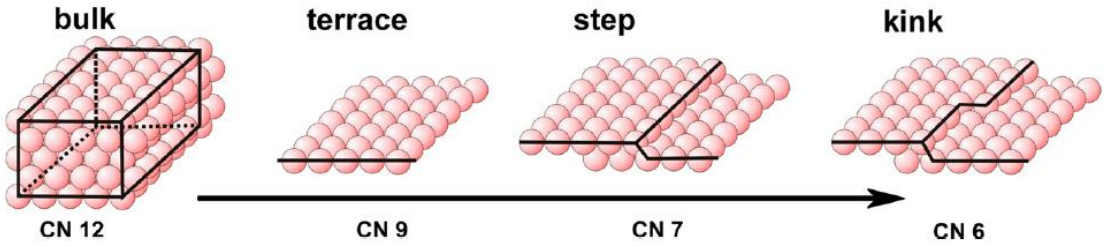

Figure 1.2. Coordination number depending on the sites[16]

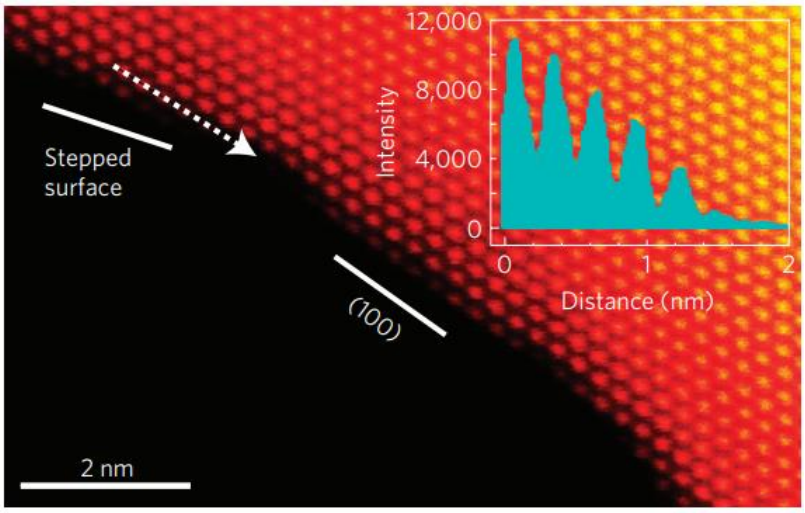

Figure 1.3. High density of atomic steps in curved region of NPG. Observed by TEM[12]

Figure 1.4. shows microstructure of NPG. The ligaments and holes are marked in figure. The size of ligaments and holes are up to ~ 100 nm in normal conditions. These ligaments and holes are very important in mechanical properties. Generally, stability is increasing with the size of ligaments. The size of ligaments and holes could be controlled by thermal annealing method. The annealing causes the diffusion of gold atoms and low-coordinated atoms which are located in step or kink sites to move and aggregate so that size of ligaments becomes large. Figure 1.5. shows annealing effect of NPG with different annealing conditions (annealing temperature, time)[17].

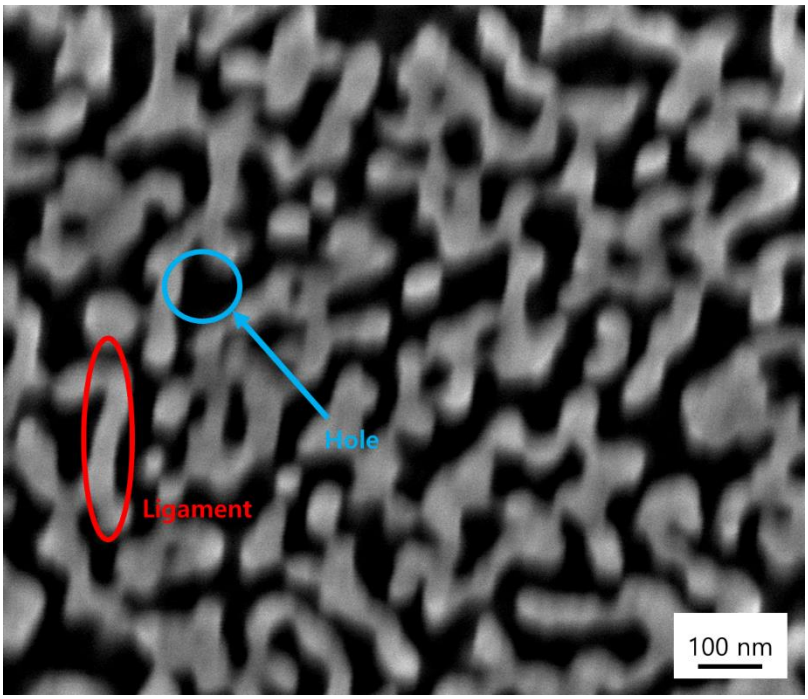

Figure 1.4. SEM image of NPG from Au-Mg alloy. Dealloyed by acetic acid

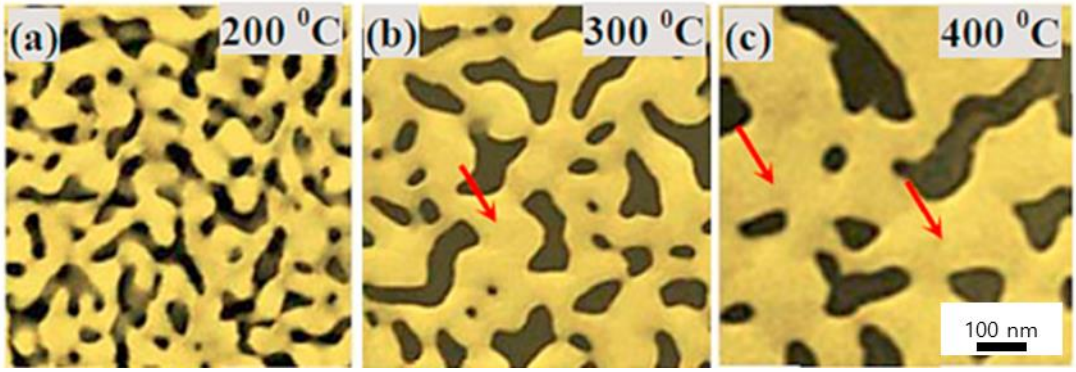

Figure 1.5. Coarsening of nanporous gold with different temperature[17]

1.1.2 Fabrication method : Dealloying

NPG is made by dealloying process. Gold alloy with less noble element is etched by free corrosion or electrochemical method. Silver is widely used for making NPG. For that, we will address the dealloying process in this chapter with Au-Ag alloy while we did not use it and used Au-Si, Au-Mg alloys. Au-Ag alloy system has been widely used because Au-Ag phase diagram shows simple solid solution system i.e. there is no intermetallic phase. However, the same concept could be applied to other alloy systems. Actually, there are a number of sacrificial elements for making nanoporous structure such as nickel, copper, aluminum, etc. The intrinsic alloy can affect to the properties of nanoporous gold and it is mainly depending on the phase diagram of the alloy. We described the phase diagrams of Au-Ag, Au-Si, and Au-Mg and explained how they affect to the nanoporous structures and differences in chapter 6 (Figure 6.4, p.92).

During the dealloying, there are two important phenomena occur at the alloy/electrolyte interface, dissolution and diffusion. Silver atoms are dissolved while gold atoms diffuse and aggregate to each other. Both phenomena are closely related to dealloying conditions, we will address these issues below.

1.1.3 Parting limit and percolation

To occur the dealloying phenomena, silver content should be at least ~55 % called parting limit. The parting limit can be addressed by percolation theory. Figure 1.6. shows the basic notions of percolation theory. For dissolving of silver, the percolation channel should be formed. The acid solution attacks the alloy through percolation channel. In figure 1.6 (a), the percolation channel is formed which silver can percolate and plays as a passage through acidic solution (gold and silver atom are drawn as orange and gray circles, respectively). On contrast, in figure 1.6 (b), the silver atoms are much less than figure 1.6 (a) and they are not connected each other. In this case, silver atoms are surrounded by gold atoms and acid cannot attack the silver.

In structural consideration, the threshold composition of silver below which silver atom cannot percolate is around 0.2 for faced center cubic (FCC) structure[18]. However, in real, it is around ~ 0.55 which is called parting limit. This large discrepancy can be addressed by high-density-percolation (HDP) thresholds[18]. Silver atoms which are located on kink or step sites are dissolvable while 10 or 11 coordinated atoms are not. Kinetic Monte Carlo (KMC) simulations tested this model[18] and observed parting limit as 0.5 which is close to the real parting limit.

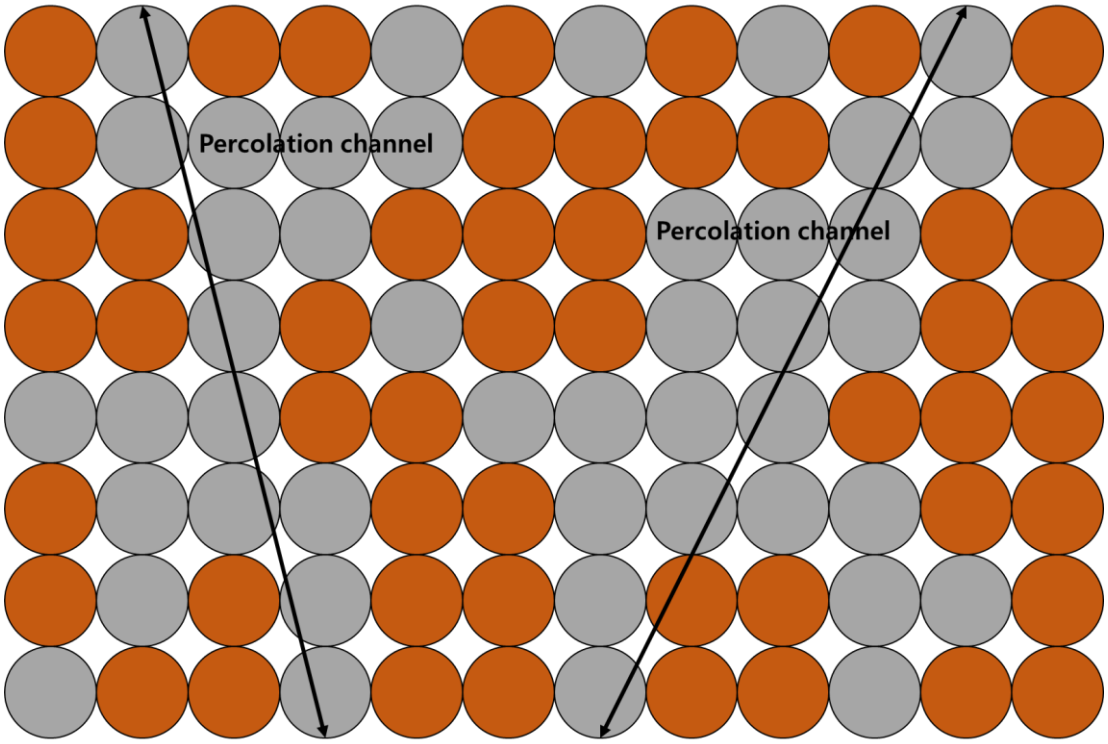

Figure 1.6 (a) Au-Ag alloy structure with percolation channel

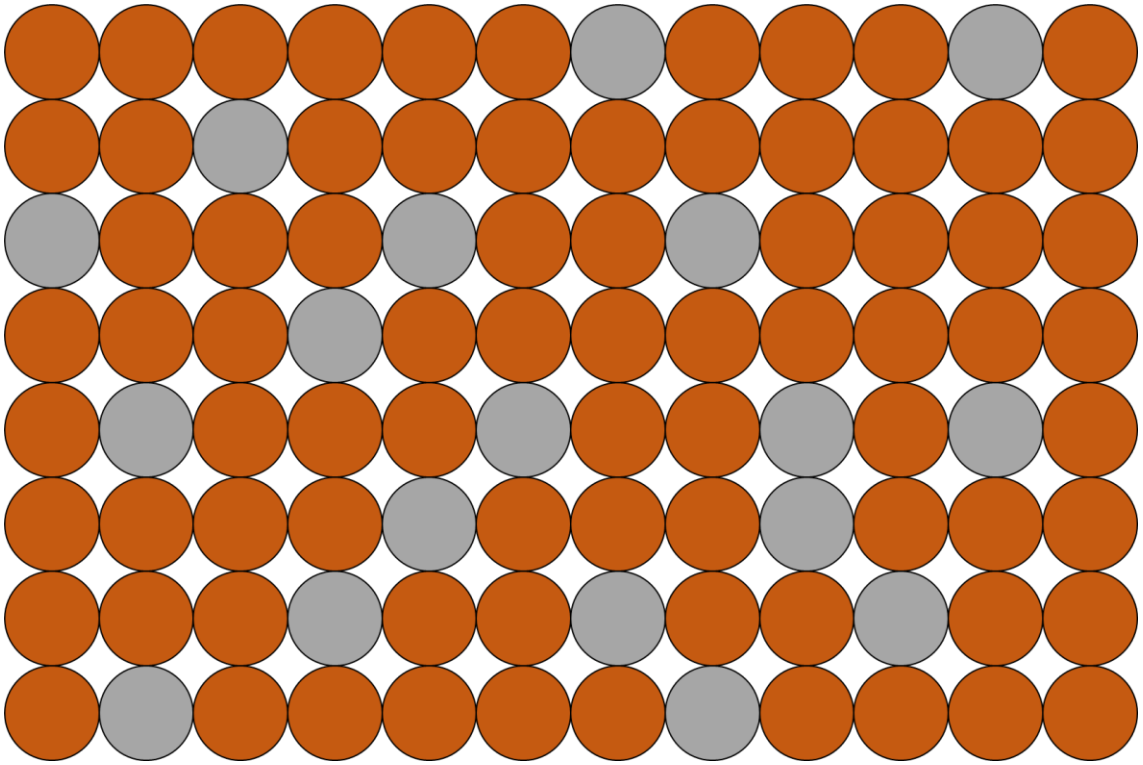

Figure 1.6 (b) Au-Ag alloy structure with no percolation channel

1.1.4 Dealloying by free corrosion

Free corrosion method is that immerse the alloy into acidic solution such as concentrated nitric acid (70 %), hydrofluoric acid, etc. During the dealloying, silver atoms are dissolved while gold atoms diffuse. The diffusion strongly depends on the temperature. Therefore, the temperature of acidic solution plays very important role in delloying. In high temperature acidic solution, diffusion of gold increases and gold atom will accumulate low-coordinated sites and size of ligaments becomes large. As a result, the catalytic activity is decreased while stability is increased. Dealloying time also can affect the result. Gold atoms can move further as dealloying time increased so that size of ligaments is increased. Concentration of solution is also important factor in dealloying. This is especially important when using weak acid (e.g. CH_3COOH) because too low concentration of weak acid could not dissolve the sacrificial elements while too high concentration dissolve it too fast so that the structure of NPG becomes weak. One should optimize the dealloying condition of type of acidic solution, temperature of solution, dealloying time, and concentration of acid solution.

1.1.5 Dealloying using electrochemical cell and critical potential

Electrochemical method is that apply the voltage to alloy in acidic solution and drive the dissolution of sacrificial element. The conventional thee electrode cell is commonly used for dealloying and the alloy is used as working electrode. The basic of electrochemistry will be discussed in below. When the potential is scanned with constant rate, at first, small current is measured. When the potential is over some threshold, current is rapidly increased and dealloying is very quickly done. (figure 1.7) The threshold potential which is called critical potential is affected by composition of alloy; it is increased with composition of silver. In case of electrochemical dealloying, the dealloying rate is very fast (dealloying is done in few minutes) so that nanoporous structure could be very weak. Indeed, we made gold-silicon alloy thin film by sputtering and dealloyed by electrochemical method, however, the thickness of film is reduced as half because the dealloying rate is too fast so that films are detached during the dealloying.

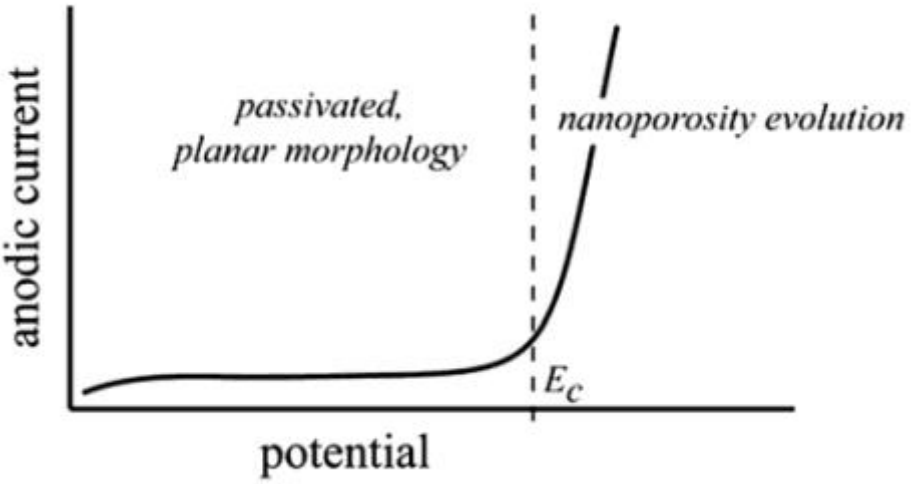

Figure 1.7. Typical current-potential plot of electrochemical dealloying[18]. E_c is the critical potential

1.1.6 Applications of NPG

NPG is a very versatile material. There are a number of applications of NPG including catalyst, sensor, actuator, and electrochemical system. The NPG is used by itself as well as combined with other materials such as metal or metal oxide nanoparticles[19], polymer, etc. Besides, many researchers have been studied with NPG for hierarchical structures[20], molecular functionalization, microfabrication, etc. NPG can be applied to many research fields. We will address our applications of NPG as non-enzymatic sensor for aniline in chapter 3, charge carrier with polyaniline for supercapacitor in chapter 4, and combined with palladium for direct ethanol fuel cell in chapter 5.

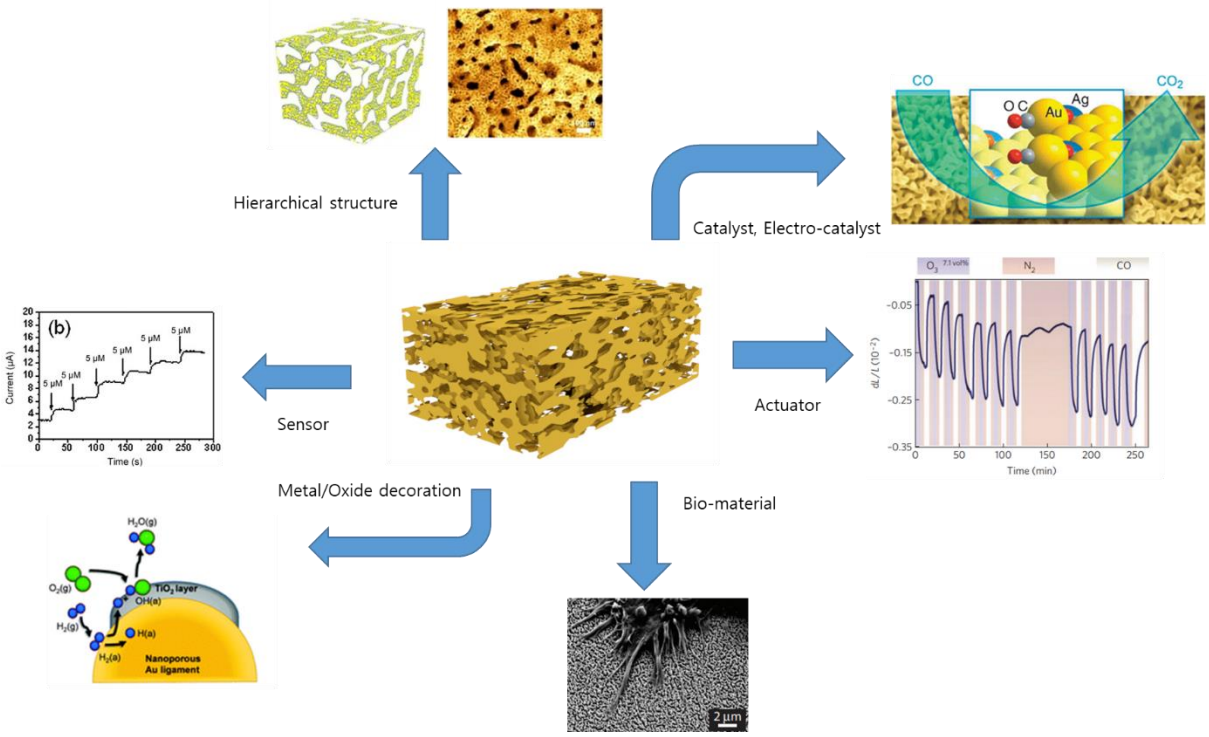

Figure 1.8. NPG: A versatile material. Various applications of NPG including hierarchical structure, catalyst[21], bio material[22], actuator[23], etc.

1.2 Basic of electrochemistry

1.2.1 Electrochemical systems

Electrochemistry is an area of chemistry dealing with the inter-conversion of electrical energy and chemical energy. In electrochemical processes, electric current could be either produced from chemical reactions or used to drive chemical reactions.

The electrochemical system is commonly composed of two electrodes, called cathode and anode, in contact with an electrolyte as shown in figure 1.9 (a). When the potential is different between two electrodes, electrons are produced at the anode by oxidation reaction and move to cathode and consumed by reduction reaction.

Researchers usually use conventional three electrode system which is composed with working electrode, reference electrode, and counter electrode (figure 1.9 (b)). Working electrode is where interested reactions occur. The potential of working electrode is controlled with respect to the reference electrode. The reference electrode has a constant makeup so that the potential of reference electrode is fixed. The counter electrode receives or generates electrons from or to the working electrode and makes complete electric circuit.

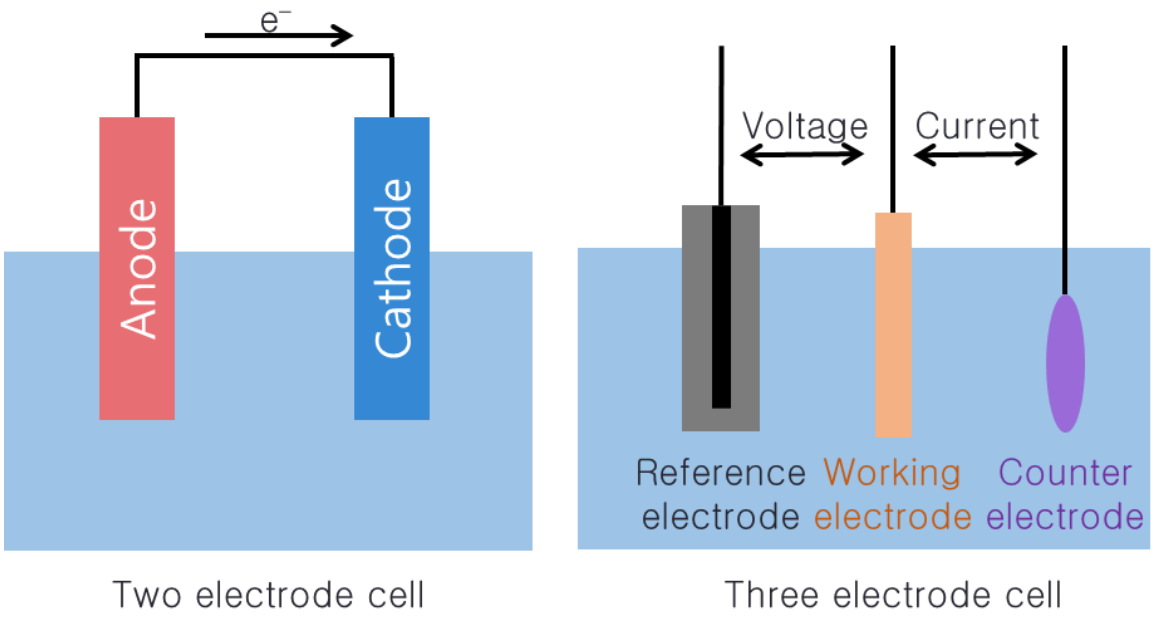

Figure 1.9. Electrochemical cell. (a) Two electrode cell and (b) conventional three electrode cell

1.2.2 Nature of electrode/electrolyte interface

When the potential is charged to electrode immersed in electrolyte, an electric double layer is made on the electrode. Schematic of electric double layer is shown in figure 1.10.[1] Imagine that the positive voltage is charged to electrode. Because of the positive charge, anion in the electrolyte firstly absorbed on the electrode, which is inner Helmholtz plane (IHP). After that, due to the gathered anions, cations are absorbed on the IHP and form an outer Helmholtz plane (OHP). Since this second plane is loosely absorbed on the first plane, ions could freely move in the fluid. The charge density at the electrode side is balanced by the total charge density at the solution side. Based on this, behavior of the electrode-solution interface is analogous to that of a capacitor. Indeed, electric double layer capacitance (EDLC) is widely used for supercapacitor. We will address the supercapacitor in chapter 4 in detail.

The formation of electric double layer causes a potential gradient across the interfacial region (figure 1.11). As a results, the molecules in the electrolyte may experience different potential from the real potential difference between the electrode and the electrolyte. For instance, when an electroactive species, that is not specifically adsorbed, can reach the electrode only to the OHP, the total potential it experiences is less than the potential between the electrode and the electrolyte by an amount $\phi_2 - \phi^s$ due to the potential drop. It can affect to the reaction rates. The researcher should bear in mind in respect to potential drop and design the experiment conditions.

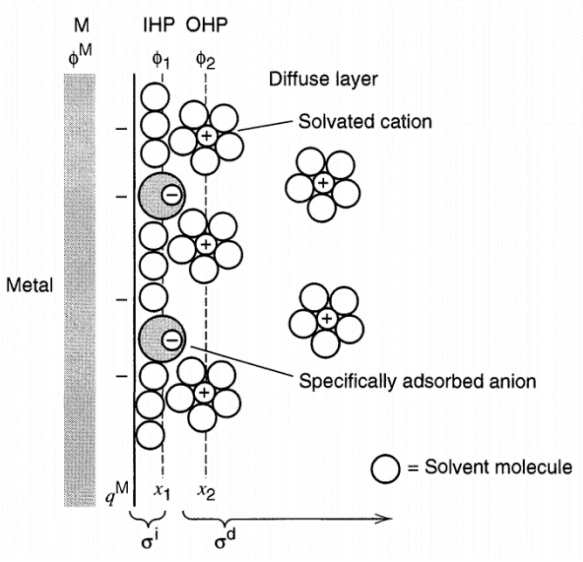

Figure 1.10. Schematic of electric double layer[24]

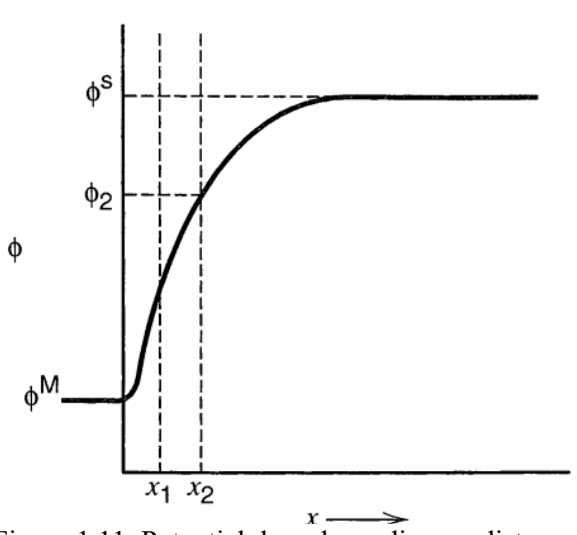

Figure 1.11. Potential drop depending on distance between electrode surface[24]

1.2.3 Current in electrochemistry

The current occurred at an electrode/electrolyte interface originates from faradaic processes (desired electrochemical reactions) or/and non-faradaic processes (double layer, adsorption, desorption, etc.). In case of faradaic processes, the quantity of charge passed across an interface is proportional to the amount of material that has undergone chemical reaction according to Faraday's Law as govern by the following equations:

$$q = nFAN \qquad (1.1)$$

And therefore, the current is calculated via

$$i = \frac{dq}{dt} = nFA\frac{dN}{dt} \qquad (1.2)$$

Where, q is the charge passed (C), n is the number of electrons transferred, F is Faraday constant ($1F = 96{,}485\ C/mol$), A is geometric area of electrode (cm^2), N is the number of moles electrolyzed, i is the current (A), and t is time passed (s).

According to equation (1.2), current represents the rate of electrochemical reactions.

1.2.4 Nernst equation

The Nernst equation is an important equation which relates reaction equilibrium potential and concentration of redox species. It can determine the cell potential under non-equilibrium conditions.

From the standard thermodynamics, the relation between actual free energy (ΔG) and standard Gibbs free energy(ΔG^o) is written as

$$\Delta G = \Delta G^o + RTlnQ \qquad (1.3)$$

Where, R is the universal gas constant (R=8.31 $JK^{-1}mol^{-1}$), Q is the reaction quotient.

And the Gibbs free energy is related to the electrode potential E(V) via

$$\Delta G = -nFE \qquad (1.4)$$

Here, n is the number of electrons transferred, F is Faraday's constant (1F = 96485 C/mol).

At the standard condition,

$$\Delta G^o = -nFE^o \qquad (1.5)$$

Where, E^o(V) is the standard electrode potential, ΔG^o(J/mol) is the standard Gibbs free energy change. From the equation (1.3), (1.4), and (1.5), the Nernst equation is expressed as follow:

$$\mathrm{E} = E^o - \frac{RT}{nF} lnQ \qquad (1.6)$$

1.2.5 Electrochemical oxidation/reduction reaction depending on energy of electrons

Figure 1.12 shows that how an electrochemical reaction occur according to the energy of electrons. In this case, the energy of electrons is opposite to applied potential. At the equilibrium, in the absence of an external potential, an equilibrium potential will be set up (figure 1.12 (a)). At this point, equilibrium potential is considered to be equal to the Fermi level. When the negative potential is applied to the electrode, the energy of electrons is raised (figure 1.12 (b)). The energy level can reach a high enough to transfer into LUMO (lowest unoccupied molecular orbital) of molecules in electrolyte. In that case, electrons transfer to molecules in electrolyte and reduction occurs. Similarly, when the positive potential is applied to the electrode, the energy of electron is lowered. The energy level can reach a low enough to transfer into HOMO (highest occupied molecular orbital) of molecules in electrolyte. The electrons can transfer from electrolyte to electrode and oxidation occurs.

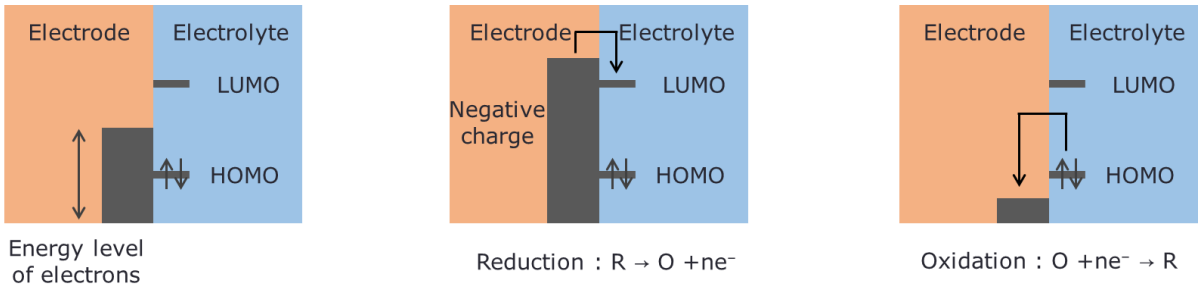

Figure 1.12. Schematic of energy level and molecular energy states during the oxidation and reduction reactions.

1.2.6 Electrochemical kinetics

The electrochemical kinetics has two parts, charge transfer and mass transfer. The charge transfer relates to an electrochemical reaction (Faradaic reaction) in electrode/electrolyte interface. The mass transfer concerns with a phenomena active molecules comes from the bulk electrolyte to the electrode.

When the mass transfer rate is fast enough, overall reaction rate is depending on the charge transfer rate and the current is given as Butler-Volmer equation.

$$i_{net} = i_0[e^{-\frac{\alpha nF\eta}{RT}} - e^{\frac{(1-\alpha)nF\eta}{RT}}] \qquad (1.7)$$

Where, i_{net} is net current, i_0 is exchange current, α is symmetry factor, and η is over potential ($\Delta E = E - E_{eq} = \eta$). Detailed driving is easily found in reference[ref]. The Butler-Volmer equation describes the relationship between current (reaction rate) and applied potential.

In case of mass transfer, there are three kinds of driving force as follows

1) Diffusion : movement of ions and molecules by concentration gradient. It depends on the Fick's law.
2) Convection : movement of ions and molecules by stirring or hydrodynamic transport.
3) Migration : movement of charged ions under the influence of an electric field.

The mass transfer phenomenon is governed by Nernst-Plank equation, written by

$$J = -D\frac{\partial C}{\partial x} - \frac{zF}{RT}DC\frac{\partial \phi}{\partial x} + Cv(x) \qquad (1.8)$$

Where, J is the flux of species at the distance x from the surface, D is the diffusion coefficient, $\partial C/\partial x$ is the concentration gradient, $\partial \phi/\partial x$ is the potential gradient, z is charge and C is concentration of species, and $\upsilon(x)$ is the velocity of species, respectively. Each terms in Nernst-Plank equation are corresponding to diffusion, migration, and convection, respectively.

1.2.7 Electrochemical methods

There are a number of electrochemical technique using potentiostat and three electrode system, however, in this chapter, we will briefly introduce cyclic voltammetry and chorono amperometry which are very widely used and important electrochemical methods.

Cyclic voltammetry

In cyclic voltammetry technique, voltage applied to working electrode is increased with a constant scan rate from set low value to high value, and voltage is decreased to low value, this called one cycle. During the voltage cycle, the current response is continuously recorded (figure 1.13). It is beneficial to study the redox reaction, which can observe one or more than two of redox reactions. Potential range, scan rate, and cycle number are important parameters in cyclic voltammetry.

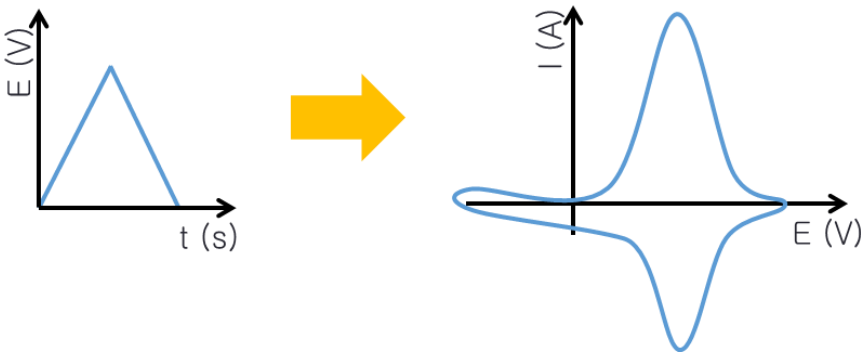

Figure 1.13. Cyclic voltage sweep and resulting current response.

In case of reversible reaction, and the R=298 K, the peak current is described as the following

$$i_p = (2.69 \times 10^5) n^{\frac{3}{2}} A D^{\frac{1}{2}} C \nu^{\frac{1}{2}} \qquad (1.9)$$

Where i_p is the peak current, and ν is scan rate. The current is proportional to root of scan rate.

The cyclic voltammetry is very widely used in overall electrochemistry systems. For example, it is used to study for a various redox processes including stability of reaction products, presence of

intermediates, etc.

Chrono amperometry

Chrono amperometry also records the current responses during the reaction while potential is fixed (figure 1.14 (a)). At the first time, current shows very high value, however, it becomes rapidly decreased. The species near the electrode is firstly consumed and there will be a concentration gradient. Further reaction can occur by diffusion of species and the equilibrium is achieved between diffusion and consumption of species. (figure 1.14 (b), (c)).

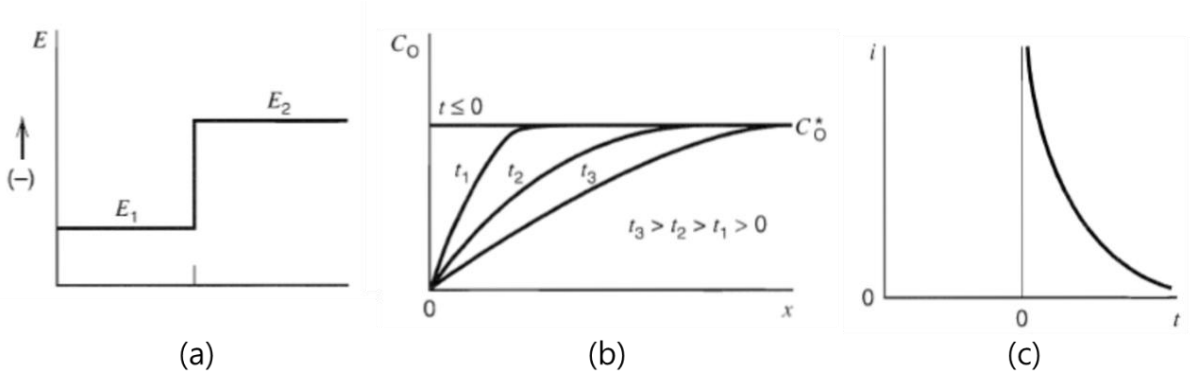

Figure 1.14. (a) Potential change during the chrono amperometry. (b) Concentration difference for various time during the reaction. (c) Recorded current during the experiment.

The current is described by Cottrell equation (equation 1.10). The Cottrell equation is deduced from planner electrode according to the diffusion law and Laplace transformation. The detailed derivation is omitted.

$$i = \frac{nFA\sqrt{D}C}{\sqrt{\pi t}} \qquad (1.10)$$

The chrono amperometry is used to study the kinetics of electrochemical reactions, sensing applications, long-time stability test for energy devices, etc. The chrono amperometry and cyclic voltammetry are usually used together. The peak potential is defined by cyclic voltammetry and the peak potential is used in chorono amperometry.

1.3 References

1. Wittstock, A.; Biener, J.; Bäumer, M., Chapter 1 Introduction to Nanoporous Gold. In *Nanoporous Gold: From an Ancient Technology to a High-Tech Material*, The Royal Society of Chemistry: 2012; pp 1-10.
2. Wittstock, A.; Biener, J.; Bäumer, M., Nanoporous gold: a new material for catalytic and sensor applications. *Physical Chemistry Chemical Physics* **2010,** *12* (40), 12919-12930.
3. Lee, K.-U.; Tran, T. H.; Kim, S. H.; Shin, H.-J., Fabrication of nanoporous gold thin films on glass substrates for amperometric sensing of aniline. *Journal of Alloys and Compounds* **2017,** *713*, 132-137.
4. Quynh, B. T. P.; Byun, J. Y.; Kim, S. H., Nanoporous gold for amperometric detection of amino-containing compounds. *Sensors and Actuators B: Chemical* **2014,** *193*, 1-9.
5. Wittstock, A.; Zielasek, V.; Biener, J.; Friend, C. M.; Bäumer, M., Nanoporous Gold Catalysts for Selective Gas-Phase Oxidative Coupling of Methanol at Low Temperature. *Science* **2010,** *327* (5963), 319-322.
6. Guo, H.; Yin, H.; Yan, X.; Shi, S.; Yu, Q.; Cao, Z.; Li, J., Pt-Bi decorated nanoporous gold for high performance direct glucose fuel cell. *Scientific Reports* **2016,** *6* (1), 39162.
7. Wang, K.; Stenner, C.; Weissmüller, J., A nanoporous gold-polypyrrole hybrid nanomaterial for actuation. *Sensors and Actuators B: Chemical* **2017,** *248*, 622-629.
8. Li, X.; Liu, M.; Huang, B.; Liu, H.; Hu, W.; Shao, L.-H.; Wang, Z. L., Nanoporous-Gold-Based Hybrid Cantilevered Actuator Dealloyed and Driven by A Modified Rotary Triboelectric Nanogenerator. *Scientific Reports* **2016,** *6* (1), 24092.
9. Lee, K.-U.; Byun, J. Y.; Shin, H.-J.; Kim, S. H., A high-performance supercapacitor based on polyaniline-nanoporous gold. *Journal of Alloys and Compounds* **2019,** *779*, 74-80.
10. Lang, X.; Hirata, A.; Fujita, T.; Chen, M., Nanoporous metal/oxide hybrid electrodes for electrochemical supercapacitors. *Nature Nanotechnology* **2011,** *6* (4), 232-236.
11. Ding, Y.; Kim, Y.-J.; Erlebacher, J., Nanoporous Gold Leaf: "Ancient Technology"/Advanced Material. *Advanced Materials* **2004,** *16* (21), 1897-1900.
12. Fujita, T.; Guan, P.; McKenna, K.; Lang, X.; Hirata, A.; Zhang, L.; Tokunaga, T.; Arai, S.; Yamamoto, Y.; Tanaka, N.; Ishikawa, Y.; Asao, N.; Yamamoto, Y.; Erlebacher, J.; Chen, M., Atomic origins of the high catalytic activity of nanoporous gold. *Nature Materials* **2012,** *11* (9), 775-780.
13. Yim, W.-L.; Nowitzki, T.; Necke, M.; Schnars, H.; Nickut, P.; Biener, J.; Biener, M. M.; Zielasek, V.; Al-Shamery, K.; Klüner, T.; Bäumer, M., Universal Phenomena of

CO Adsorption on Gold Surfaces with Low-Coordinated Sites. *The Journal of Physical Chemistry C* **2007,** *111* (1), 445-451.

14. Nørskov, J. K.; Bligaard, T.; Hvolbæk, B.; Abild-Pedersen, F.; Chorkendorff, I.; Christensen, C. H., The nature of the active site in heterogeneous metal catalysis. *Chemical Society Reviews* **2008,** *37* (10), 2163-2171.
15. Biener, J.; Wittstock, A.; Zepeda-Ruiz, L. A.; Biener, M. M.; Zielasek, V.; Kramer, D.; Viswanath, R. N.; Weissmüller, J.; Bäumer, M.; Hamza, A. V., Surface-chemistry-driven actuation in nanoporous gold. *Nature Materials* **2009,** *8* (1), 47-51.
16. Biener, J.; Biener, M. M.; Madix, R. J.; Friend, C. M., Nanoporous Gold: Understanding the Origin of the Reactivity of a 21st Century Catalyst Made by Pre-Columbian Technology. *ACS Catalysis* **2015,** *5* (11), 6263-6270.
17. Chen, A. Y.; Shi, S. S.; Liu, F.; Wang, Y.; Li, X.; Gu, J. F.; Xie, X. F., Effect of annealing atmosphere on the thermal coarsening of nanoporous gold films. *Applied Surface Science* **2015,** *355*, 133-138.
18. Erlebacher, J.; Newman, R. C.; Sieradzki, K., Chapter 2 Fundamental Physics and Chemistry of Nanoporosity Evolution During Dealloying. In *Nanoporous Gold: From an Ancient Technology to a High-Tech Material*, The Royal Society of Chemistry: 2012; pp 11-29.
19. Qadir, K.; Quynh, B. T. P.; Lee, H.; Moon, S. Y.; Kim, S. H.; Park, J. Y., Tailoring metal–oxide interfaces of inverse catalysts of TiO2/nanoporous-Au under hydrogen oxidation. *Chemical Communications* **2015,** *51* (47), 9620-9623.
20. Guo, X.; Han, J.; Liu, P.; Chen, L.; Ito, Y.; Jian, Z.; Jin, T.; Hirata, A.; Li, F.; Fujita, T.; Asao, N.; Zhou, H.; Chen, M., Hierarchical nanoporosity enhanced reversible capacity of bicontinuous nanoporous metal based Li-O2 battery. *Scientific Reports* **2016,** *6* (1), 33466.
21. Moskaleva, L. V.; Röhe, S.; Wittstock, A.; Zielasek, V.; Klüner, T.; Neyman, K. M.; Bäumer, M., Silver residues as a possible key to a remarkable oxidative catalytic activity of nanoporous gold. *Physical Chemistry Chemical Physics* **2011,** *13* (10), 4529-4539.
22. Seker, E.; Berdichevsky, Y.; Staley, K. J.; Yarmush, M. L., Microfabrication-Compatible Nanoporous Gold Foams as Biomaterials for Drug Delivery. **2012,** *1* (2), 172-176.
23. Biener, J.; Wittstock, A.; Zepeda-Ruiz, L. A.; Biener, M. M.; Zielasek, V.; Kramer, D.; Viswanath, R. N.; Weissmüller, J.; Bäumer, M.; Hamza, A. V., Surface-chemistry-driven actuation in nanoporous gold. *Nature Materials* **2009,** *8* (1), 47-51.
24. Bard, A. J.; Faulkner, L. R., *Electrochemical methods: fundamentals and applications*. wiley New York: Vol. 2.

CHAPTER 2
EQUIPMENT AND EXPERIMETNL

In this chapter, we will introduce our equipment and their principle. Sputtering is a main equipment of this thesis so that we will intensively describe its working principle and applications. Other analytical equipment (XRD, XPS, AES, etc.) will be briefly addressed. If someone want to know the details of them, please see the references.

2.1 Sputtering

2.1.1 Introduction

Sputtering is first reported by W. R. Grove in 1852[1, 2]. It is a process which occurs at the surface of target, irradiated to the ion beam. The ejected atoms from the target by impinging ions become gas-like phase. Some of sputter-eject target atoms are deposited on the substrate, formation of a thin film[3]. Sputtering can make a film with not only conducting materials but also insulating materials such as metal oxides as well as nitrides because of its basic principle. The advantages of sputtering are written in below.

- Able to deposit a wide variety of metals, insulators, alloys and compounds
- Replication of target composition in the deposited films
- Capable of in-situ cleaning prior to film deposition
- Better film quality than evaporation
- Can use large area targets for uniform thickness over large substrates
- Reproducible deposition control

Due to these fascinating advantages, sputtering is widely used in many kinds of industries as well as labortorys[4].

2.1.2 Glow discharge and plasma

Let us consider the system of figure 2.1. Cathode and anode are in the sealed quarts with argon gas and they are connected to a power supply. There are two reasons why we use argon, one is its relatively inexpensive price and the other is the mass of argon (39.95 amu) is suitable for collision with many kinds of metals[2]. When the direct current is applied to both electrode, the background electrons which are naturally ionized are accelerated by electric field and move to the anode. During that time, the electrons will give up energy to an orbital electron of the argon atom. If this energy is less than ionization energy, the orbital electron will be excited to a higher energy level and then returned to the ground state with emission of photons of light. This ionized state is called plasma. If the energy is high enough to ionize the argon, the orbital electron will be separated from the argon, becoming a free electron (second electron). These argon ions (positive ions) are also accelerated by electric field and move to the cathode. At that time, the collision between positive ions and cathode makes an ejection of a number of electrons (second electron). These second electrons undergo as same manner, and increase the number of electrons and argon ions, resulting sustaining the plasma. The ions and electrons in the plasma are accelerated by electric field and move to cathode, and anode, respectively, however, mass of ion is relatively heavy compared to electron so that electrons can move to anode very quickly while ions are relatively slow, resulting plasma has generally positive charged. These overall process is called glow discharge (Figure 2.2). There are normal glow discharge and abnormal glow discharge and the plasma is subdivided by many regions, however, we think they are beyond the scope of this thesis. If you are curious about that, see the references.[5]

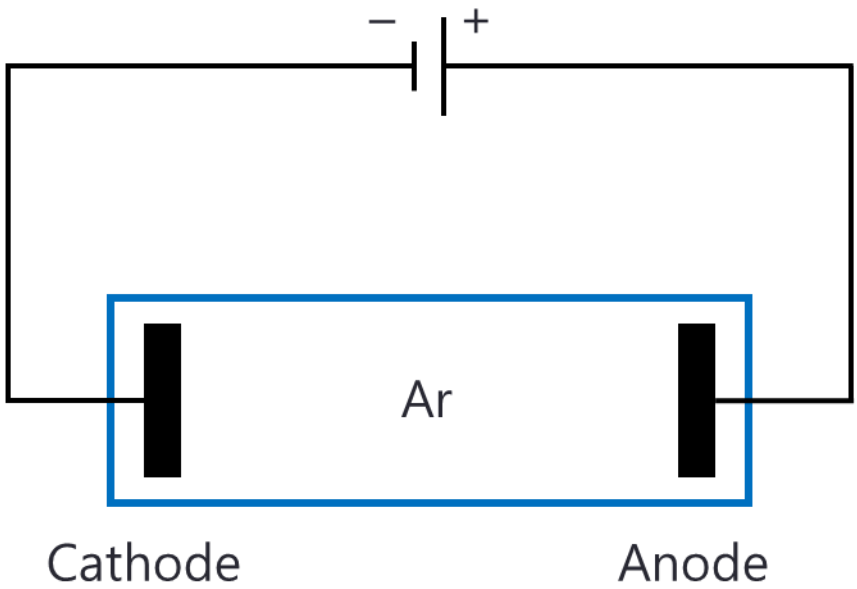

Figure 2.1. Glow discharge system

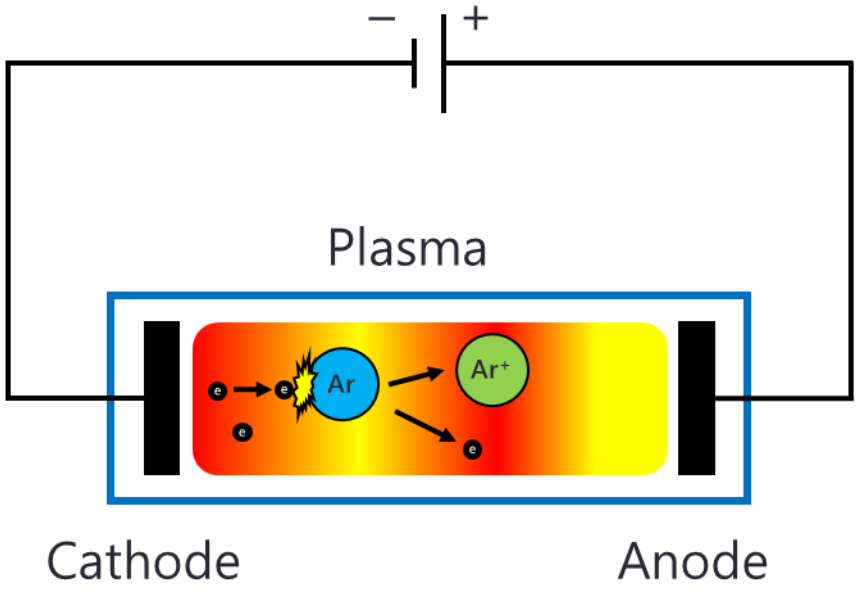

Figure 2.2. Generation of secondary electrons during glow discharge

2.1.3 The cathode region

After the glow discharge occur, we need to consider the cathode region (figure 2.3). The ionized argons are accelerated and move to the cathode. At that time the argon ion can be neutralized by collusion with electron. The neutralized argon atoms are not affected by electric field, however, they are already accelerated and sputter the cathode. Even argon ions can reach the cathode without collusion with electron, they are neutralized by electron in the cathode. These neutralized argon ions diffuse into plasma and ionized again, repeat as same manner.

The applied voltage is one of the very important parameters in sputtering. When the applied voltage is high, the energy of accelerated argon will be high. Figure 2.4 shows ejection of atoms depending on the energy of argon. If the energy of accelerated argon is low, the atoms will be ejected. If the energy is higher, the molecules or clusters will be ejected. The high energy will be better to fast deposition, however, it may be not good for uniform film surface. The researcher should optimize the deposition condition with film surface and applying voltage.

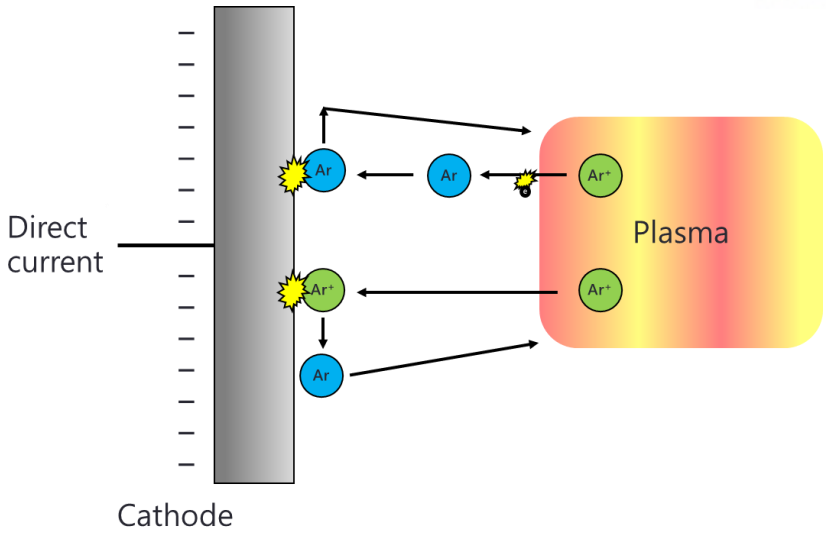

Figure 2.3. Phenomenon that occurs around the cathode during the sputtering

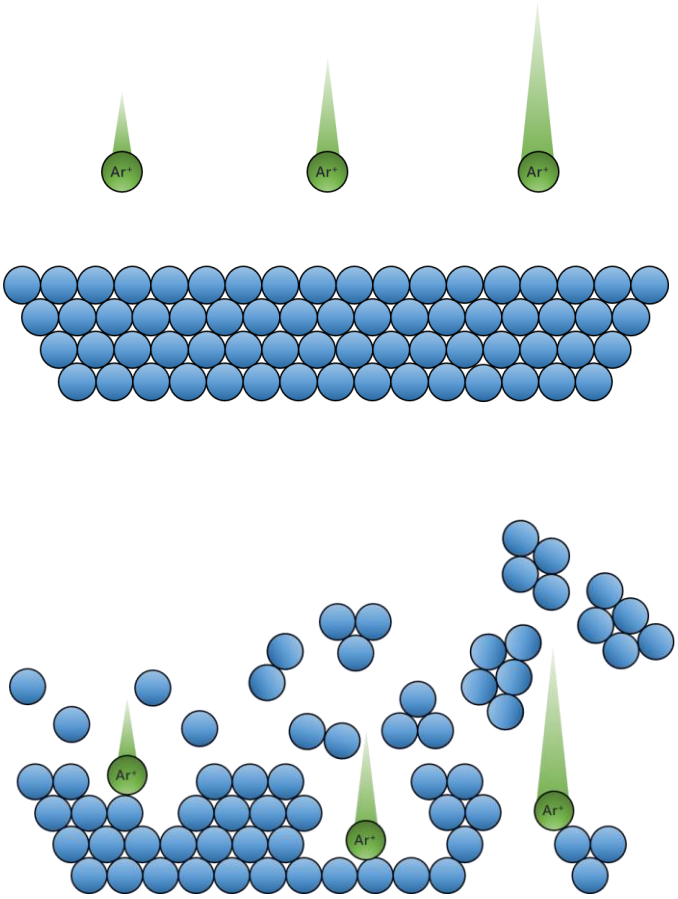

Figure 2.4. Ejection of target atoms depending on the energy of argon ion

2.1.4 Magnetron sputtering

Basically, the efficiency of ionization form energetic collision between the electrons and gas atoms is very low. Most electrons lose their energy in non-ionization collisions or are collected by the electrodes. Therefore, the deposition rate will be also low. To resolve this drawback, to increase deposition rate, magnets are used to increase the percentage of electrons that take part in ionization events, increasing the ionization efficiency. A magnetic field is applied at right angles to the electric field by placing large magnets behind the target (figure 2.5). This traps electrons near the target surface and causes them to move in a spiral motion until they collide with an argon atom (figure 2.6). Then the ionization and sputtering efficiencies are significantly increased. Only the electrons will be affected; the ions are too massive.[5] The orbital motion of electrons increases probability that they will collide with natural species and create ions. There are so many magnetically enhanced sputtering systems but we think these are beyond the scope of this thesis. See the reference[6].

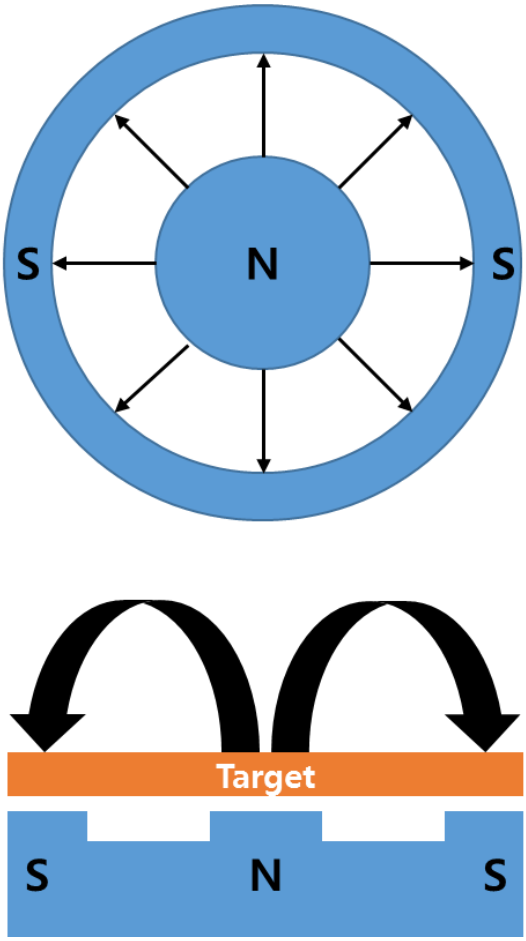

Figure 2.5. Magnetron sputtering system

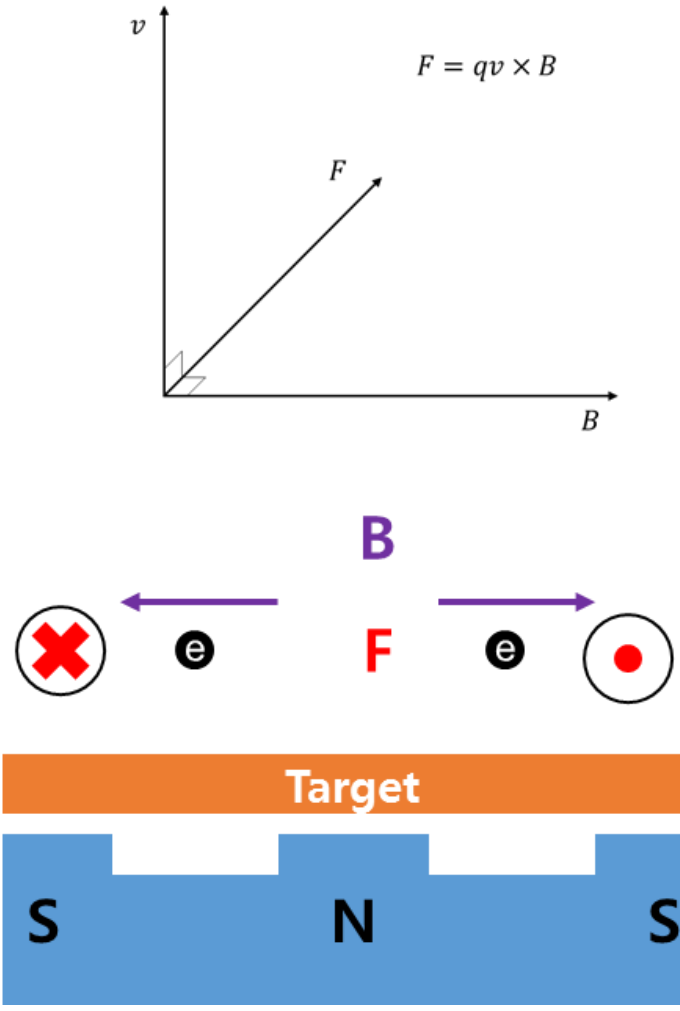

Figure 2.6. Schematic of force the electron receives in magnetron sputtering

2.1.5 Reactive sputtering

The sputtering uses a target of pure material is desired, and an inert gas, usually argon. If the material is a single pure chemical element, the atoms are simply ejected from the target and deposit in that form. However, it is also possible to use a reactive gas such as oxygen or nitrogen with the inert gas (argon). The ionized reactive gas can react chemically with the target material and produce a compound which then becomes the deposited film (figure 2.7). For example, a cerium target reactively sputtered with oxygen gas can produce a cerium oxide film[7], or an aluminum target with oxygen gas can produce an aluminum oxide film[8].

The control of the ratio of inert gas (argon) and reactive gas is very important for chemical reactions which make compound[9]. The reactive gas flow should be adjusted to get good composition without incorporating excess gas into film (e.g. SiO_2 rather than SiO_{2-x}).

The reactive gases are typically injected by mass flow controller (MFC) system which can control the flow of gases. Commonly used reactive gases are oxygen and nitrogen. A mixture of inert gas and reactive gases used for sputtering is shown in below

Oxides : Al_2O_3[10], SiO_2[11], Ta_2O_5[12], NiO[13] – O_2 mixed with Ar

Nitrides : Ta_xN[14], TiN[15], SiN_x[16] – N_2, NH_3, mixed with Ar

Carbides : TiC[17], WC[18], SiC[19] – CH_4, C_2H_2, C_3H_8, mixed with Ar

Reactive sputtering is very attractive because it can directly make compound films, however, it also can poison the target if chemical reactions are faster than sputter rate.

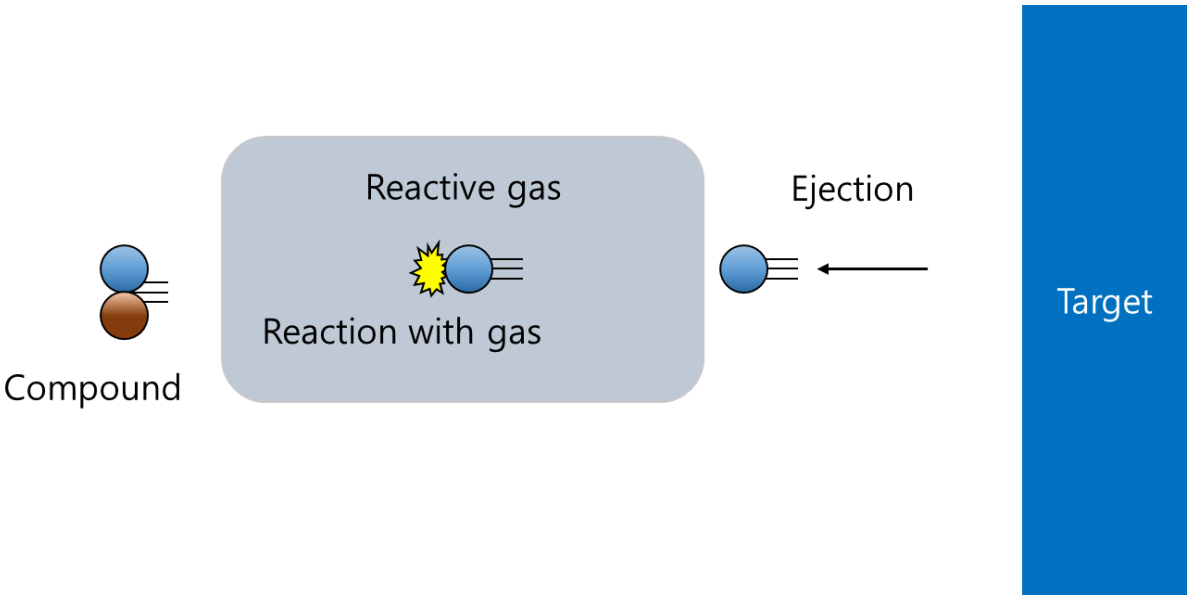

Figure 2.7. Reactive sputtering processes

2.1.6 *Radio frequency (RF) sputtering*

If the target is insulating, the plasma is not occurred by direct current glow charge process because the cation will accumulate on the target surface (figure 2.8). Therefore, there will be no more secondary electrons and no more collision and ionization so that plasma is not sustained. Consequently, we cannot sputter the insulating target by direct current power supply.

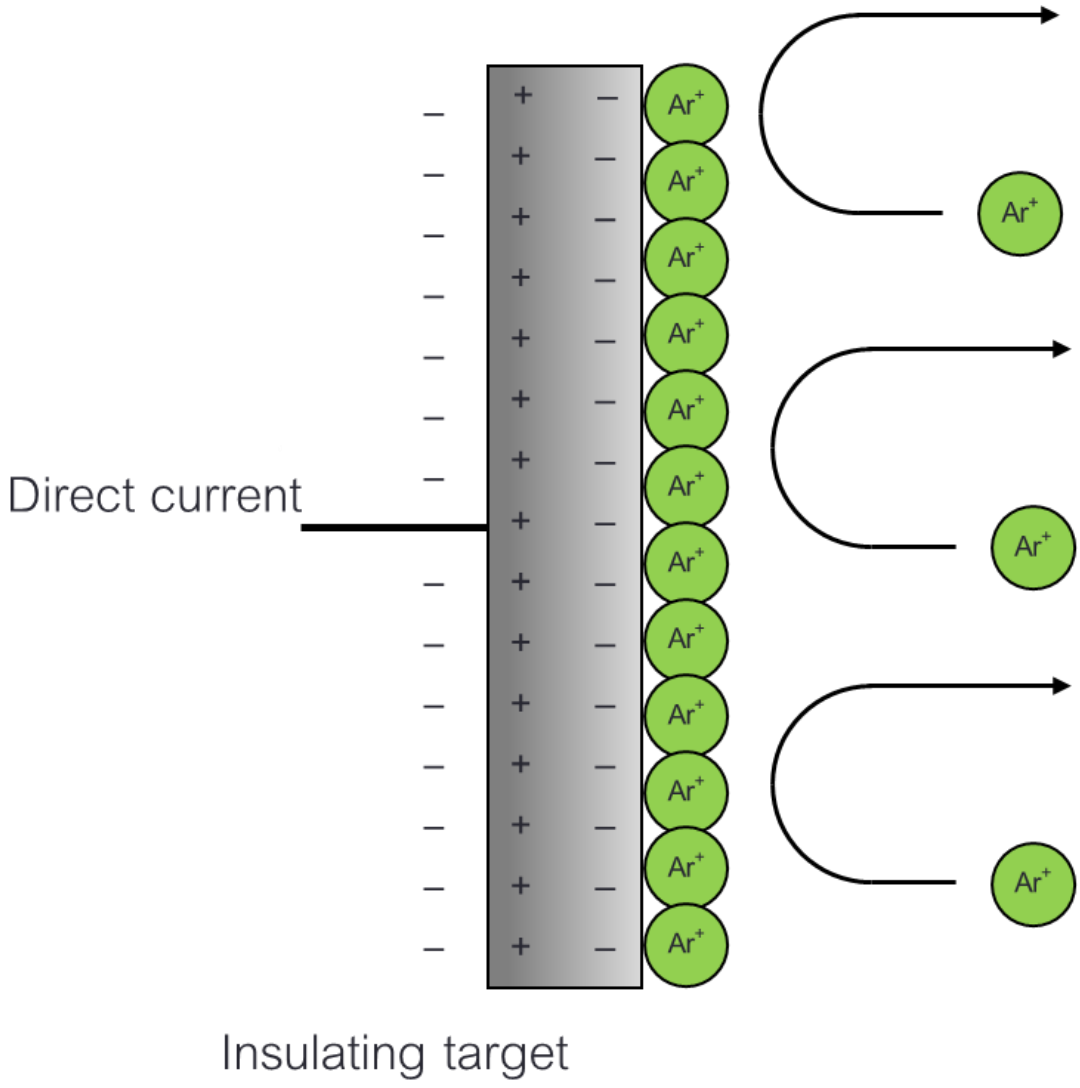

Figure 2.8. When the direct current is applied to insulating target – Argon ions are accumulated on the target surface

In order to this problem, researchers developed radio frequency (RF) sputtering technique which can sputter both conducting and insulating target. A conductive plate is placed behind an insulating target (figure 2.9). RF sputtering technique is using alternative power supply, which makes cations continuously collide with the target. This called RF glow charge.

Let us consider the RF glow charge process in detail. When the negative potential is charged to target, the cation will collide with surface and accumulate, which is similar to that negative DC power is charged. Secondly, the potential will change to negative and cations accumulated on surface will be ejected from the surface (figure 2.10). Therefore, cation can collide with surface again and the target will be sputtered.

One can wonder that how can the target sustain its charge as negative. The answer is self-bias effect. When the positive/negative charge is applied, the electron/cation moves to the target. In that case, the mobility of electron is much faster than cation. Accordingly, the number of electrons become larger than that of cations so that target becomes negatively charged. The RF power system controls the current as zero, however, there are more electrons. Therefore, RF power system makes the target as negative for an increased influx of cations (figure 2.11). Finally, target can sustain negative charge and sputtering can occur. This called self-bias effect[20].

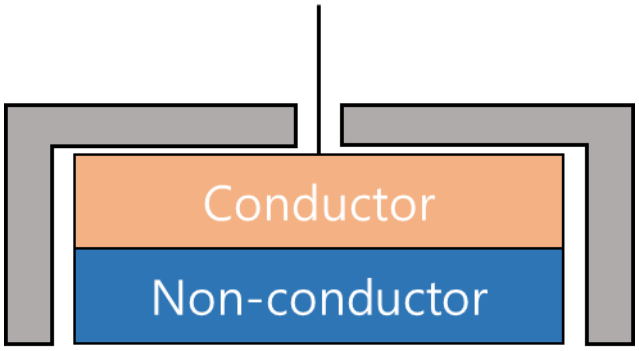

Figure 2.9. Radio-frequency sputtering target for non-conductors.

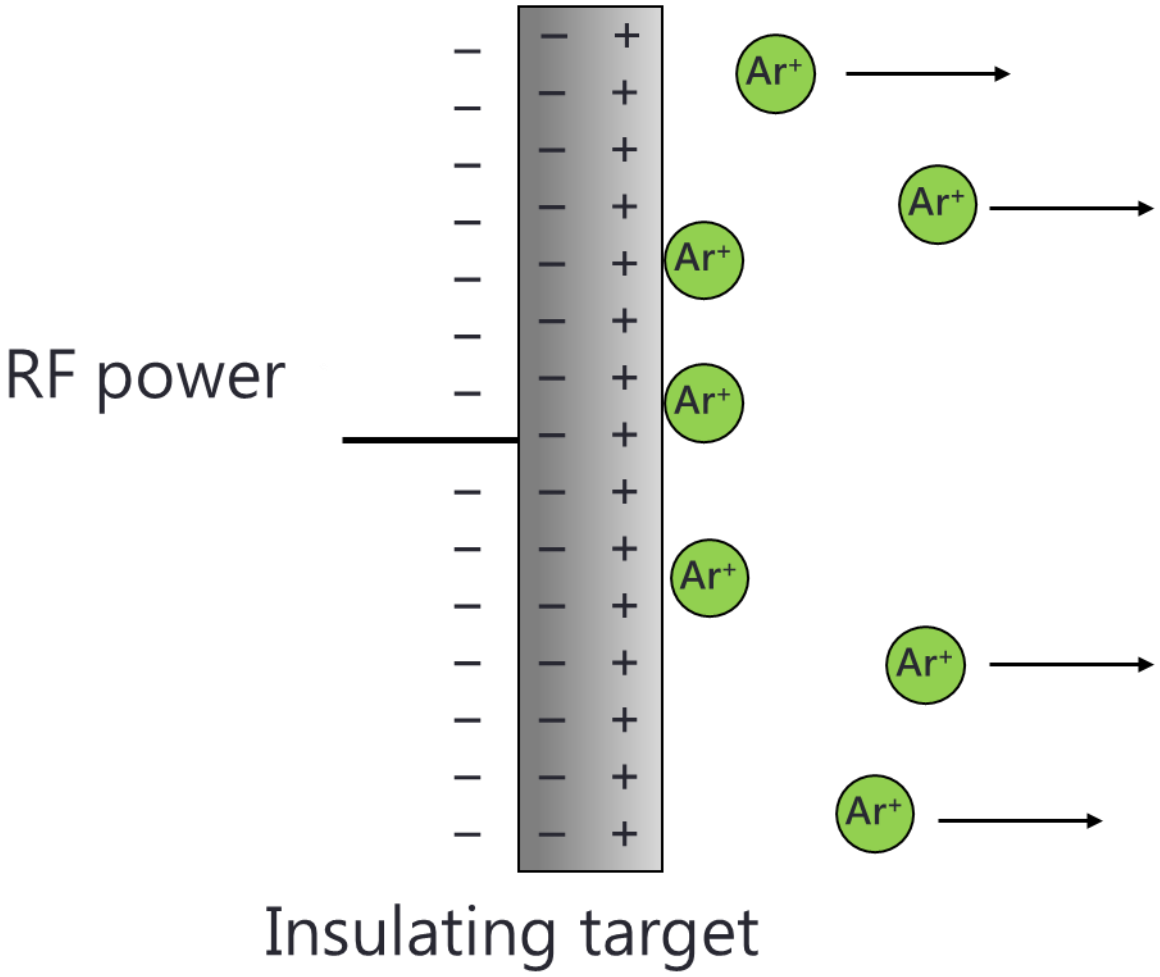

Figure 2.10. Cathode region during the RF sputtering

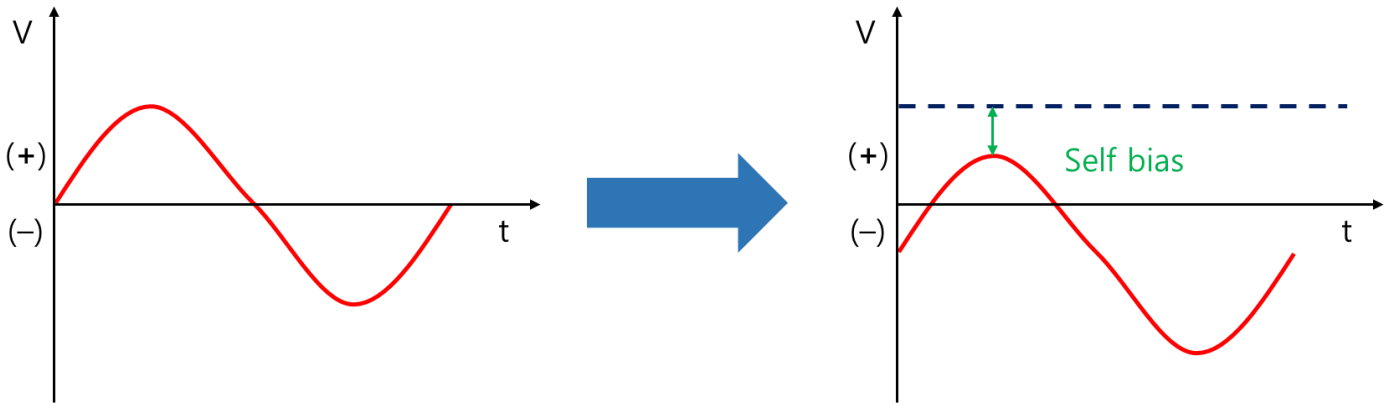

Figure 2.11. Self-bias effect during the radio frequency sputtering

2.1.7 Sputtering equipment

Figure 2.12 shows our sputtering machine and figure 2.13 is schematic of our sputtering systems. There are two chambers; main chamber and load-lock chamber. Each chambers are connected to pumps, main chamber has turbo molecular pump and rotary pump and load-lock chamber has only rotary pump. In front of the turbo molecular pump, there is a butterfly valve which can control the flow of fluid. In the main chamber, there are ion gauge and pirani gauge which can record the pressure while load-lock chamber has only pirani gauge. The mass flow controller (MFC) is connected to main chamber which can control the flow of gases such as argon, oxygen, nitrogen, etc. Each connection is closed or opened by gate valves.

Details of main chamber is described in figure 2.14. The main chamber is quiet simple, there are guns, and sample stage. The sample stage can rotate for uniform deposition of films and it can also move up and down for loading a sample or sputtering position. Under the stage, there is a heater which can heat the sample stage and enhance the mobility of deposited atoms for uniform thickness of films. In the sputtering gun, the target is fixed and connected to power supply. We have four guns and two direct current (DC) power supply and one radio frequency (RF) power supply.

Figure 2.15 shows schematic of sputtering gun. There is water line inside the gun for cooling of target during the sputtering. The target is fixed and power line is connected to target. Under the target there are magnets for enhancing the yield of sputtering but figures of magnets are omitted. We can easily connect to DC or RF power supply.

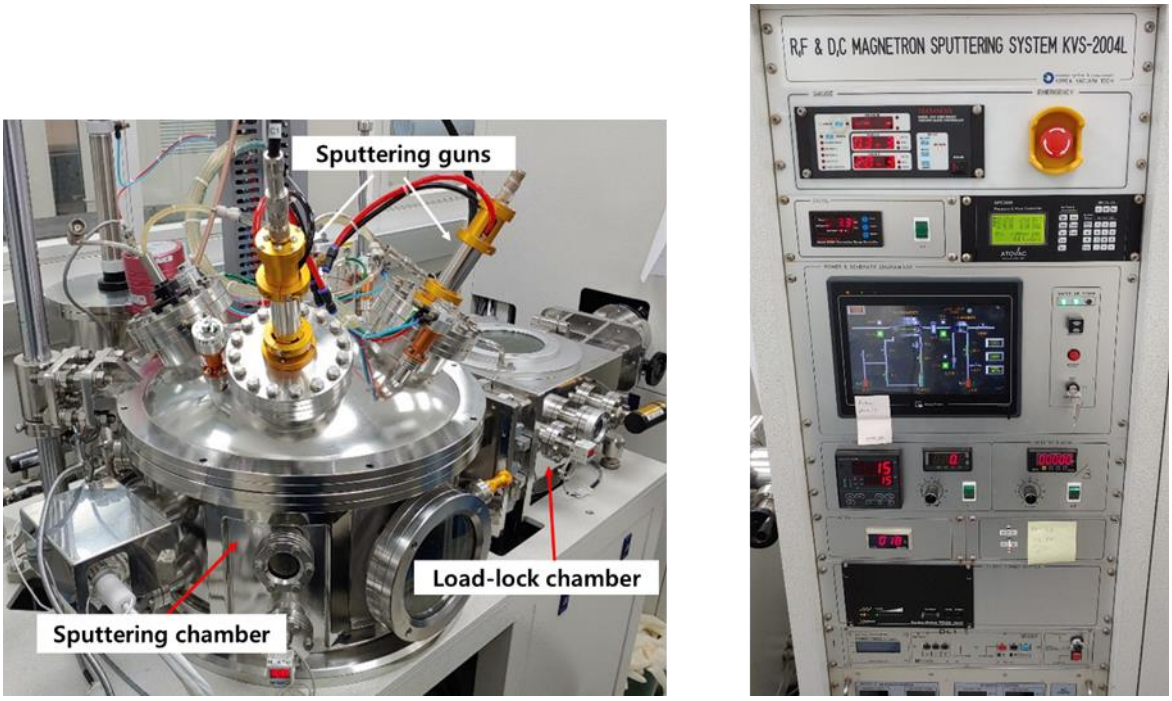

Figure 2.12. Pictures of our sputtering machine and control tower

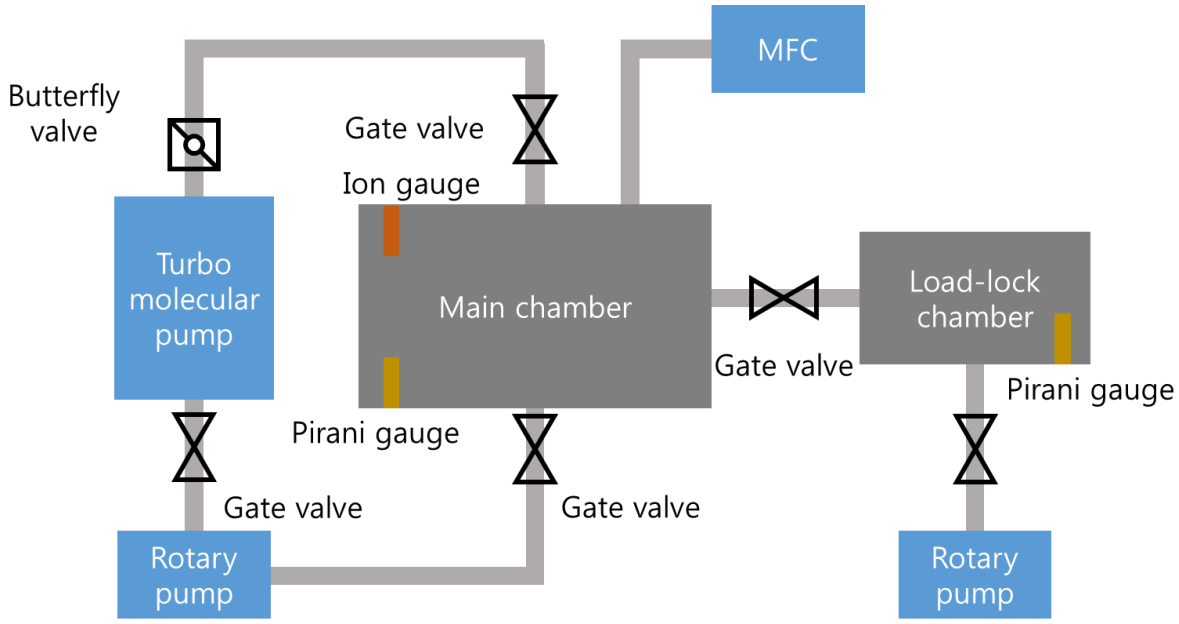

Figure 2.13. Schematic of our sputtering systems

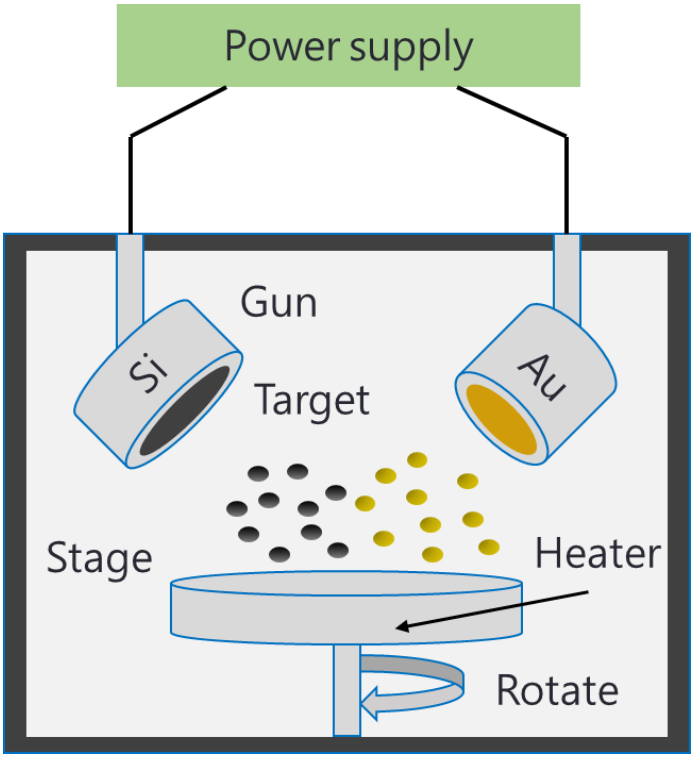

Figure 2.14. Schematic of main chamber

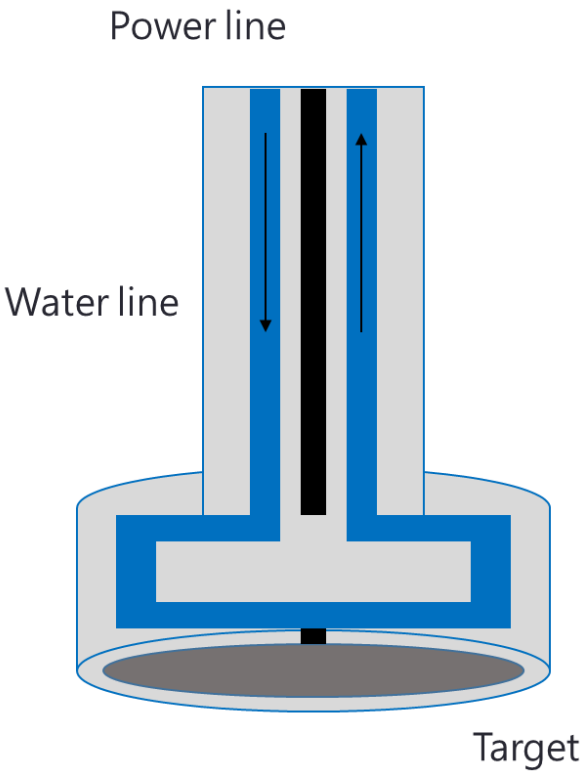

Figure 2.15. Sputtering gun

2.2 Analytical equipment

2.2.1 X-ray diffraction (XRD)

X-ray diffraction (XRD) is a powerful tool for analyzing the structure of materials with non-destructive method[21]. X-ray is a form of light with wavelength of ~ nanometers which is comparable with the lattice spacing of materials. In this thesis, XRD is used to determine the phase of sputtered alloy films and dealloyed films.

When the x-ray is directed toward a material, the x-ray interferes with the atomic planes of crystal, resulting in a pattern of higher or lower intensities which relies on the Bragg's law. As shown in figure 2.16, the constructive interference occur when $n\lambda = BD + CD = 2d\sin\theta$ is satisfied. Where, n is an integer, λ is the wavelength of ray, θ is an incident angle, and d is a lattice spacing. The x-ray is scanned from low angle to high angle and the intensity of reflected ray is recorded. The peaks will appear when the Bragg's rule is satisfied and they could be used to determine the lattice spacing and characterize the material and its crystal structure. The stress or defect can shift the position of the peaks.

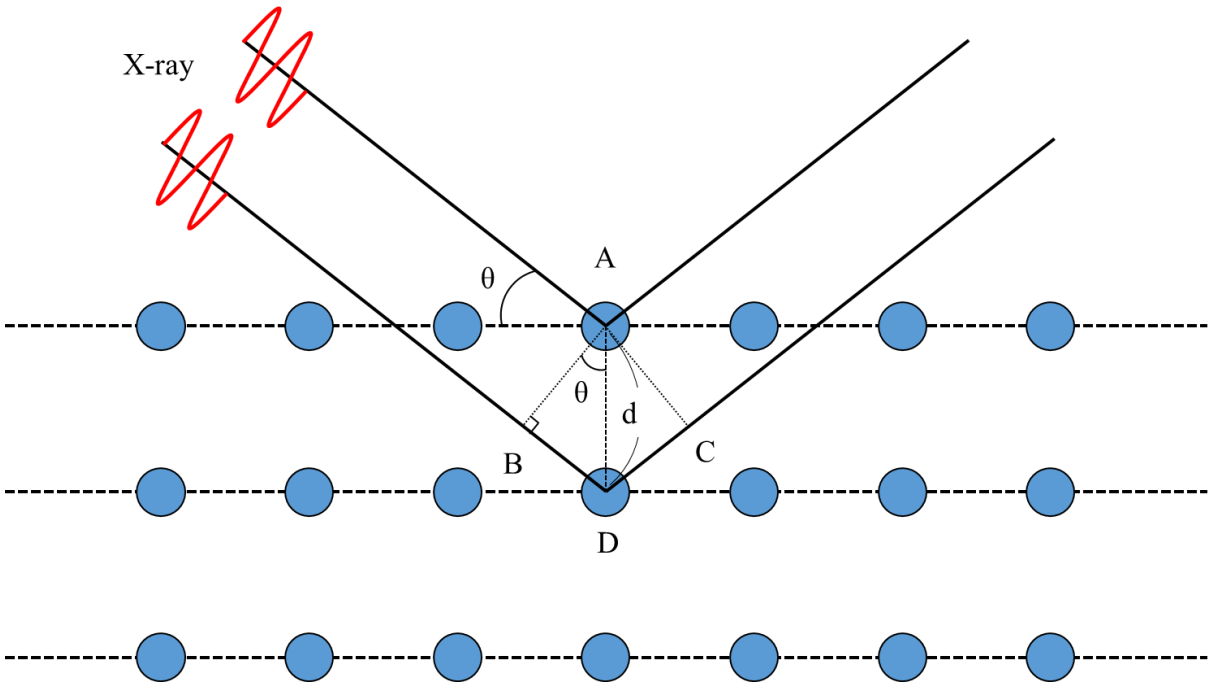

Figure 2.16. Schematic diagram of Bragg's law

2.2.2 X-ray photoelectron spectroscopy (XPS)

X-ray photoelectron spectroscopy (XPS) is widely used technique to investigate the chemical state and electronic state of materials[22]. It is based on the photoelectric effect which is the emission of an electron or other carriers when the light is radiated to the material (figure 2.17). When the electron is ejected from the surface by radiation of x-ray, the kinetic energy of electron is expressed as equation (2.1).

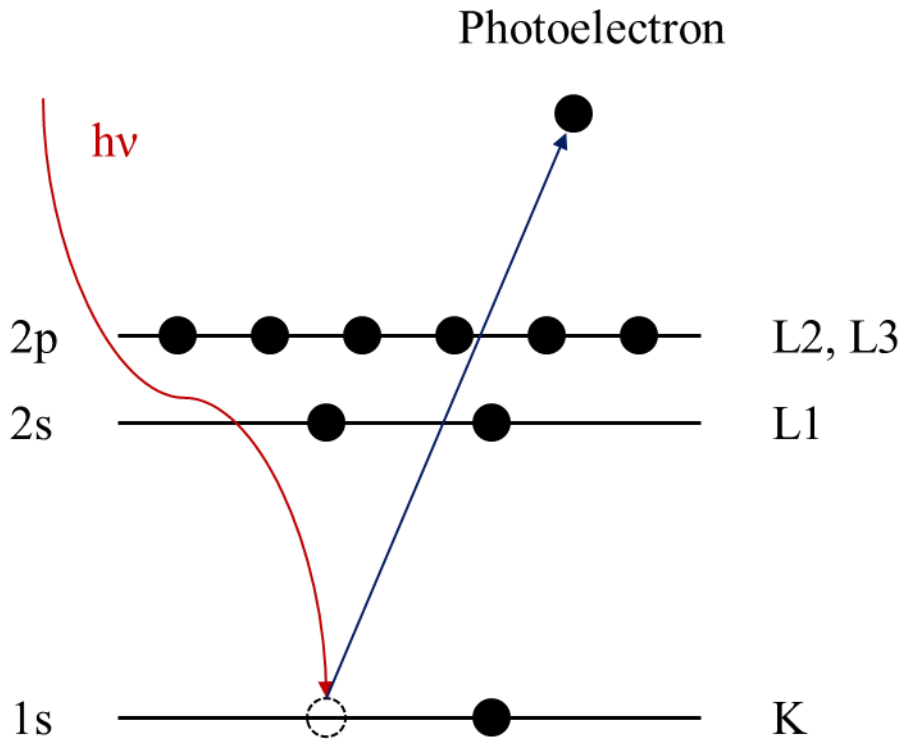

Figure 2.17. Photoemission of electrons

$$KE = h\nu - BE - \phi \qquad (2.1)$$

Where, KE is kinetic energy of ejected electron, hν is energy of x-ray, BE is the binding energy of electron, and ϕ is the work function. A photoelectron spectrum is acquired by counting photoelectrons over a range of kinetic energies. The energies and intensities of the photoelectron peaks can be used as quantification and identification of surface elements. By measuring the kinetic energy, we could calculate the binding energy of electron and obtain the information of chemical state. The binding energy is affected a number of factors including element, orbital, and chemical environments. XPS is therefore very useful to identify the chemical states of elements.

2.2.3 Auger electron spectroscopy (AES)

AES is most widely used technique for analyzing the surface chemical composition by recording the energies of Auger electrons[22, 23]. AES uses Auger effect and it is shown in figure 2.18. A core state electron in the atom is removed leaving behind a vacancy in the K shell by incident high-energy electron beam. As the atom is unstable, the vacancy can be filled by an electron from L shell falling down without radiation of x-ray. The excess energy can be removed by ejection of outer shell electron if the energy is greater than the binding energy (figure 2.18)

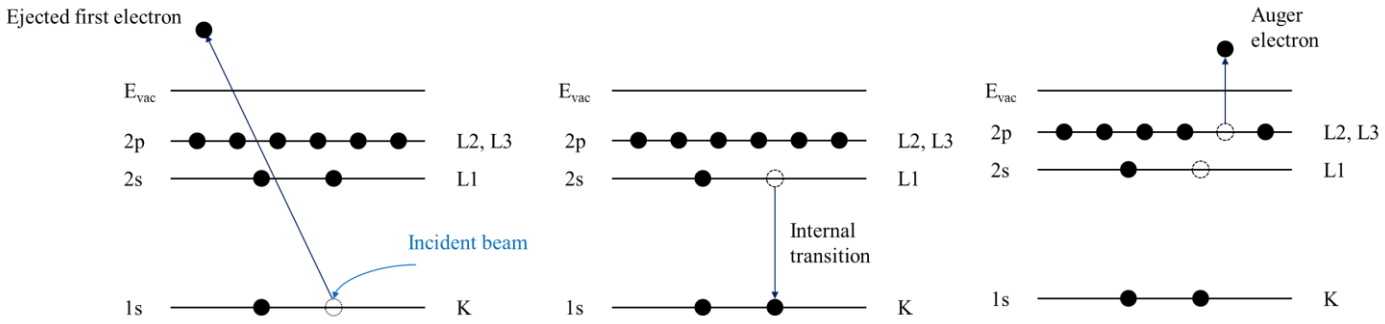

Figure 2.18. Schematic of Auger process. Ionization (left), relaxation (middle), and emission (right).

The ejected electron is called Auger electron. In this case, the kinetic energy(E_{KE}) of Auger electron will approximately be equation (2.2)

$$E_{KE} = E_K - E_M - E_L \quad (2.2)$$

Where E_K, E_M, and E_L are respectively the core level energy of each levels. As it can be seen that the kinetic energy of Auger electron is independent of the primary electron beam therefore the kinetic energies of Auger electron are characteristic of the elements.

X-ray emission is a competing with Auger emission because the energy difference can be released by x-ray emission. The yield of Auger emission is higher for light elements while x-ray yield is higher for higher atomic numbers. Therefore, AES is much great in low atomic numbers.

2.3 References

1. Stuart, R. V., CHAPTER IV - SPUTTERING. In *Vacuum Technology, Thin Films, and Sputtering*, Stuart, R. V., Ed. Academic Press: San Diego, 1983; pp 91-135.
2. Greene, J. E., Review Article: Tracing the recorded history of thin-film sputter deposition: From the 1800s to 2017. *Journal of Vacuum Science & Technology A* **2017,** *35* (5), 05C204.
3. Gulbiński, W., Deposition of Thin Films by Sputtering. In *Chemical Physics of Thin Film Deposition Processes for Micro- and Nano-Technologies*, Pauleau, Y., Ed. Springer Netherlands: Dordrecht, 2002; pp 309-333.
4. Sigmund, P., Introduction to sputtering. *Mat. Fys. Med. Dan. Vid. Selsk* **1993,** *43*, 7-26.
5. Chapman, B. N., Glow discharge processes : sputtering and plasma etching. Wiley: New York :, 1980.
6. Kelly, P. J.; Arnell, R. D., Magnetron sputtering: a review of recent developments and applications. *Vacuum* **2000,** *56* (3), 159-172.
7. Kabir, M. S.; Zhou, Z.; Xie, Z.; Munroe, P., Scratch and wear resistance of hydrophobic CeO2-x coatings synthesized by reactive magnetron sputtering. *Ceramics International* **2020,** *46* (1), 89-97.
8. Rahman, M. A.; Vivek, S. M. K.; Kim, S. H.; Byun, J. Y., Polarizonic-interference colouration of stainless steel surfaces by Au-Al_2O_3 nanocomposite thin film coating. *Applied Surface Science* **2019**, 144428.
9. Sproul, W. D.; Christie, D. J.; Carter, D. C., Control of reactive sputtering processes. *Thin Solid Films* **2005,** *491* (1), 1-17.
10. Bobzin, K.; Lugscheider, E.; Maes, M.; Piñero, C., Relation of hardness and oxygen flow of Al_2O_3 coatings deposited by reactive bipolar pulsed magnetron sputtering. *Thin Solid Films* **2006,** *494* (1), 255-262.
11. He, L.-N.; Xu, J., Properties of amorphous SiO_2 films prepared by reactive RF magnetron sputtering method. *Vacuum* **2002,** *68* (2), 197-202.
12. Cho, S.-D.; Paik, K.-W., Study on the amorphous Ta_2O_5 thin film capacitors deposited by dc magnetron reactive sputtering for multichip module applications. *Materials Science and Engineering: B* **1999,** *67* (3), 108-112.
13. Yoshimura, K.; Miki, T.; Tanemura, S., Nickel Oxide Electrochromic Thin Films Prepared by Reactive DC Magnetron Sputtering. *Japanese Journal of Applied Physics* **1995,** *34* (Part 1, No. 5A), 2440-2446.
14. Riekkinen, T.; Molarius, J.; Laurila, T.; Nurmela, A.; Suni, I.; Kivilahti, J. K., Reactive sputter deposition and properties of TaxN thin films. *Microelectronic Engineering* **2002,** *64* (1), 289-297.
15. Sproul, W. D., Very high rate reactive sputtering of TiN, ZrN and HfN. *Thin Solid Films* **1983,**

107 (2), 141-147.

16. Signore, M. A.; Sytchkova, A.; Dimaio, D.; Cappello, A.; Rizzo, A., Deposition of silicon nitride thin films by RF magnetron sputtering: a material and growth process study. *Optical Materials* **2012,** *34* (4), 632-638.
17. Samuelsson, M.; Sarakinos, K.; Högberg, H.; Lewin, E.; Jansson, U.; Wälivaara, B.; Ljungcrantz, H.; Helmersson, U., Growth of Ti-C nanocomposite films by reactive high power impulse magnetron sputtering under industrial conditions. *Surface and Coatings Technology* **2012,** *206* (8), 2396-2402.
18. Abdelouahdi, K.; Sant, C.; Legrand-Buscema, C.; Aubert, P.; Perrière, J.; Renou, G.; Houdy, P., Microstructural and mechanical investigations of tungsten carbide films deposited by reactive RF sputtering. *Surface and Coatings Technology* **2006,** *200* (22), 6469-6473.
19. Qamar, A.; Mahmood, A.; Sarwar, T.; Ahmed, N., Synthesis and characterization of porous crystalline SiC thin films prepared by radio frequency reactive magnetron sputtering technique. *Applied Surface Science* **2011,** *257* (15), 6923-6927.
20. Mahan, J. E., Physical vapor deposition of thin films. *Physical Vapor Deposition of Thin Films, by John E. Mahan, pp. 336. ISBN 0-471-33001-9. Wiley-VCH, January 2000.* **2000**, 336.
21. Bunaciu, A. A.; Udriştioiu, E. g.; Aboul-Enein, H. Y., X-Ray Diffraction: Instrumentation and Applications. *Critical Reviews in Analytical Chemistry* **2015,** *45* (4), 289-299.
22. Watts, J. F.; Wolstenholme, J., An introduction to surface analysis by XPS and AES. **2003**.
23. Gunawardane, R. P.; Arumainayagam, C. R., AUGER ELECTRON SPECTROSCOPY. In *Handbook of Applied Solid State Spectroscopy*, Vij, D. R., Ed. Springer US: Boston, MA, 2006; pp 451-483.

CHAPTER 3
NANOPOROS GOLD FOR SENSOR

3.1 Introduction

One most important goal of nanotechnology is to utilize the size effect of nanomaterial to improve and enhance the properties and performance of nanomaterial and discover the new functionalities which cannot be taken from bulk materials. Particularly, the size effect of nanomaterial depends on a surface-to-volume ratio. NPG has been attracted in a number of fields such as sensor,[1-3] catalysts,[4, 5] and actuators,[6-8] because of its outstanding properties, which are not realize in its bulk counterpart or nanoparticles. NPG has a lot of advantages including high surface-to-volume ratio, high conductivity, and no concern about loss of gold particles during experiment. Generally, NPG is fabricated by dealloying process.[9] An Au alloy with less noble element wire is prepared by drawing the molten bulk alloy. The wire is then drowned into a suitable etchant (most commonly nitric acid) to selectively dealloy the less noble elements. Many elements such as Ni, Zn, and Al are used as less noble elements,[10-12] but among them, silver is the very commonly used element for the dealloying. However, the diameter of the drawn wire is typically in the range of tens to hundreds of micrometers, which is larger than necessary for sensor or catalytic applications. Moreover, free standing NPG on the sub-micron scale is difficult to handle, requiring an additional conductive supporting substrate. In order to overcome this drawbacks, NPG electrode from Au-Si binary alloy (100–200 nm) in the form of a thin film on a Si wafer is widely used. Si is dealloyed from an Au-Si alloy by HF solution, which enables the preparation of uniform and crack-free NPG thin films with well-controlled porosity on Si wafers.[13] The NPG thin films from these processes have shown remarkable performance as electrochemical catalysts[2] and sensor. At first, NPG was used as sensor with enzymes. The enzymatic NPG sensor showed high sensing performance for detection of ethanol, hydrogen peroxide, and glucose.[14] For non-enzymatic sensing, NPG electrode also showed good performance of ascorbic acid, dopamine, hydrogen peroxide, glucose, cysteine, and environmental pollutants including hydrazine, *p*-nitrophenol, etc.[3, 15-18] In our previous studies, we successfully applied the NPG electrode to non-enzymatic direct detection of phenol, aniline, catechol, and hydroxylamine.[2, 19] For those pollution molecules, the NPG electrode showed specifically better stability for amperometric sensing with comparable sensing performance in terms of detection limits and linear range compared to other previously reported sensors made of other materials. We used HF solution for the dealloying process, however, it is very toxic so that an alternative etchant would be highly desirable. Moreover, readily

available and cheaper substrates could accelerate the widespread adoption of NPG thin films for the applications mentioned above, with all of the advantages of conventional NPG structures.

Herein, we made NPG electrode on glass substrates with potassium hydroxide (KOH) solution instead of using HF solution and Si substrate. Dealloyed Au–Si alloy thin films (NPG) on glass substrates using KOH solution as the etchant comprised good NPG structures with good adhesion to the substrate. After that, we applied our NPG thin films to the amperometric sensing of aniline. Our environmentally friendly fabrication method of NPG thin films on glass substrates showed great performance as aniline sensors with a wide sensing range and low detection limit.

3.2 Experimental methods

Preparation of NPG films

Figure 3.1 shows a schematic of preparation process of NPG films on glass substrates. Titanium, gold, and Au–Si (alloy layer) were deposited on glass substrates by sputtering. The base pressure in the sputtering chamber was 2×10^{-6} Torr. The glass substrates were cut into pieces of 1.0×2.6 cm^2 and cleaned by consecutive ultrasonication in acetone, ethanol, and distilled water for 20 min each. After deposition of the Ti layer, we annealed the samples at 300 °C for 30 min with a heating rate of 10 °C/min. The annealing treatment was done in the same chamber without breaking the vacuum ($P = 2 \times 10^{-6}$ Torr). After that, the samples were allowed to cool to room temperature (25 °C) before subsequent layers were deposited. The thicknesses of Ti, Au, and Au–Si alloy layers were approximately 5, 30, and 300 nm, respectively. Si was selectively etched from Au–Si alloy layer by KOH solution. The concentration of KOH, temperature and etching time were all optimized to the etching conditions, which were finally set to 30 wt%, 50 °C, and 150 min, respectively.

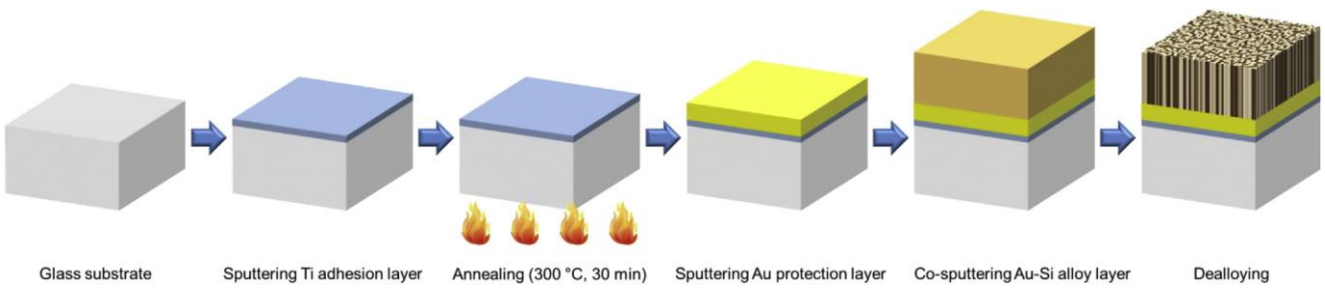

Figure 3.1 Schematic of preparation process of NPG films on glass substrate[20]

Electrochemical methods

Electrochemical experiments were carried out using a conventional three-electrode system. NPG films were used as working electrodes with 1 cm^2 exposed area, Pt wire was used as the counter electrode, Ag/AgCl (3 M NaCl) was used as a reference electrode, and all these electrodes were connected to a potentiostat (ZIVE SP1, WonATech Inc.). Cyclic voltammetry (CV) was conducted in 0.5 M H_2SO_4 solution to clean the NPG surface and calculate its surface area by the amount of reduction charge. Amperometric sensing of aniline was performed in both phosphate-buffered saline (PBS) solution and tap water.

Materials

All chemicals including aniline (>99.5%, Sigma-Aldrich), sulfuric acid (H_2SO_4) (>98%, DAEJUNG), KOH (>85%, Sigma-Aldrich), and PBS (Thermo Scientific) were used as received. Glass slides (MARIENFELD) were used as the substrates for NPG sensor fabrication.

3.3 Results and discussion

The NPG sensor is composed of a NPG thin layer (300 nm), an Au etch stop (30 nm), and a Ti adhesion layer (5 nm) on a glass substrate. Though the Ti is known to be a great adhesion metal that readily forms covalent bonds with sub-layers,[21] it did not provide strong adhesion between NPG films and glass substrates, resulting the delamination of the NPG layer from the substrate during electrochemical experiments in the beginning of this study. We also tested Cr, which is commonly used as an adhesion layer for glass substrates; however, Cr was improper here because it would be dissolved at cathodic potentials during electrochemical reactions.[21] The residual stress developed inside the film is one of the main reasons for the delamination of thin films; therefore, an annealing treatment is usually carried out during or after deposition. Furthermore, annealing treatment is known to make the surface of deposits smoother and more uniform, to increase the mobility of deposited atoms and to promote diffusion between the deposited layer and substrate, which can make adhesion stronger.[22] In order to improve adhesion, we annealed the sample at 300 °C for 30 min inside the sputtering chamber after sputtering of the Ti films. After that, the Au and Au–Si alloy layers were successively deposited. Figure 3.2(a) shows a SEM image of a NPG film on an annealed Ti layer. Compared to NPG films without the annealing step (Figure 3.2(b)), it shows a much more uniform and smoother surface. Additionally, the adhesion between the NPG film and the substrate is strong enough to carry out the electrochemical experiments with no delamination. A high-resolution SEM image (Figure 3.2(c)) shows that a number of pores are connected together and the distance between ligaments is around 80 nm.

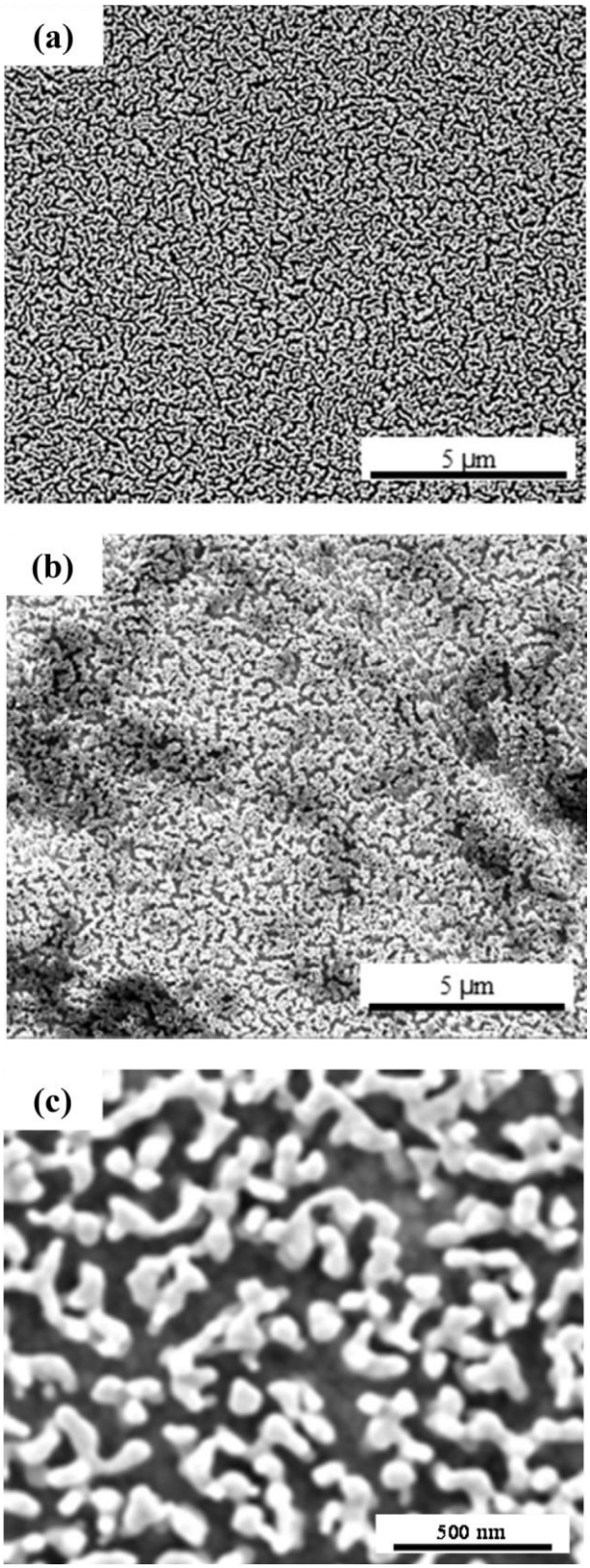

Figure 3.2 SEM images of the top view of NPG films. (a) Ti annealed NPG; (b) bare NPG (c) a high-resolution SEM image of (a).[20]

When we annealed the thin films grown on a substrate, one very important factor is the difference between the thermal expansion coefficients (TECs) of the materials.[23] If the TEC difference between the substrate and film is too large, residual stress occurs inside the film after the annealing treatment. Our NPG sensor contains three components: glass, Ti, and Au. The TECs of glass, Ti, and Au are 9.0×10^{-6} K^{-1}, 8.6×10^{-6} K^{-1} and 1.42×10^{-5} K^{-1}, respectively. The TECs of glass and Ti are similar and negligible, however, the difference in TECs between the Au layer and the Ti layer is large enough to develop the residual stress during the annealing treatment. Hence, it is very important to design an optimum heat treatment process for the preparation of durable NPG sensors. Figure 3.3 shows SEM images of multilayer films on glass made using two different heat-treatment processes. Sample **A** was prepared using the same annealing conditions as for Figure 3.2 (a), that is, only the Ti layer was annealed, followed by deposition of the Au and the Au–Si layers. The other sample (sample **B**) was annealed after the deposition of the Ti and the Au layers, and then the Au–Si layer was grown. Sample **A** has a very clean and smooth surface, whereas sample **B** has a rugged surface. Since the TEC of Au is larger than that of Ti, large tensile stress occurs inside the Au film when they are annealed and cooled together (sample **B**), resulting in weak adhesion between the Ti and the upper layers. As a consequence, the Au–Si and Au layers easily peeled off within a minute during the dealloying in KOH solution. Previously, we made NPG sensors on Au/Ti/Si, and annealed both Au and Ti layers simultaneously.[19] At that time, the NPG films annealed at high temperatures (>100 °C) showed poor sensing performance. For the same reason, the adhesion between the films and the Si substrate became weaker when the annealing temperature was too high. We believe that this is one of the reasons for the poor performance of those sensors.

In order to make a nanoporous structure, we dealloyed the Au–Si layers by immersing the sample into a 30 wt% KOH solution at 50 °C for 150 min. Figure 3.4 (a) and (c) show cross-sectional SEM images of NPG films before and after etching, respectively. The entire Au–Si layer was changed to a uniform and nanoporous structure by dealloying. Additionally, the thickness of the alloy layer was unchanged (～300 nm) after dealloying, indicating that there was no loss of Au. In order to confirm the composition of the films, we employed Auger electron spectroscopy (AES) depth profiling along the direction perpendicular to the substrate (figure 3.4 (b) and (d)). The AES depth profiling showed that Si was successfully removed by the KOH solution, forming NPG layers without considerable contamination.

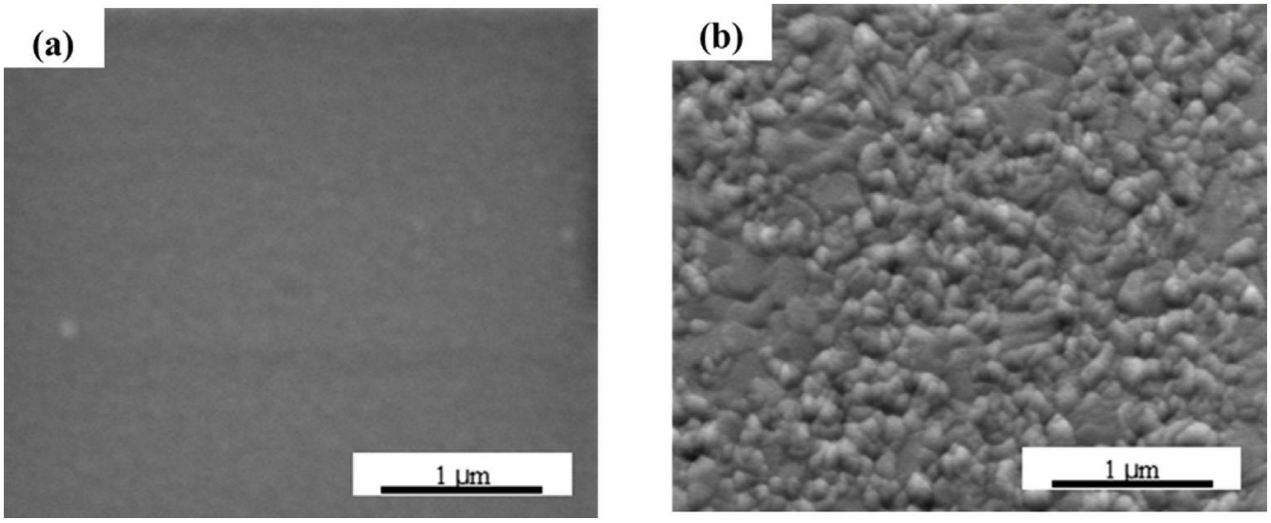

Figure 3.3 SEM images of Au-Si alloy films. (a) Sputtered on an annealed Ti layer (sample A) and (b) Sputtered after annealing both the Ti and the Au layers (sample B).[20]

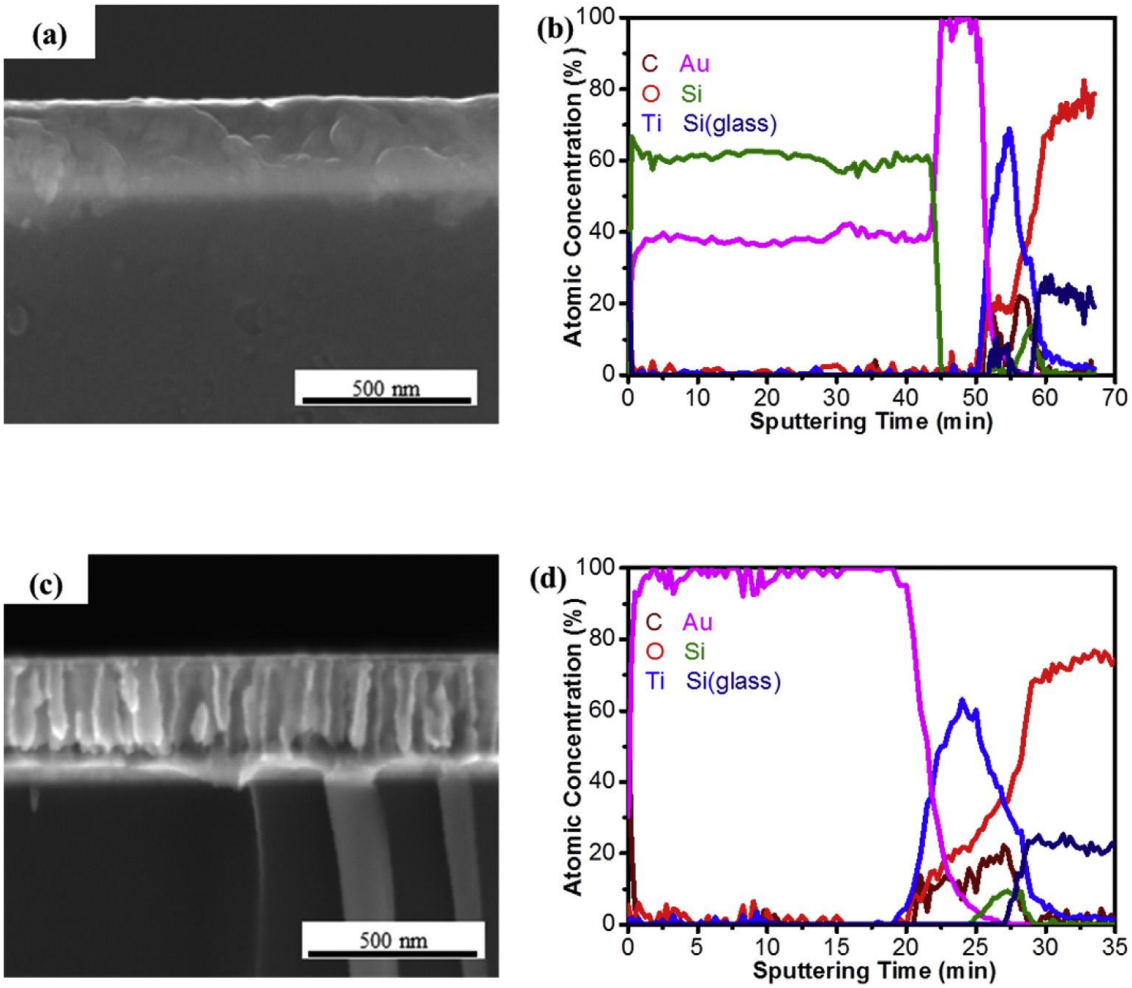

Figure 3.4 Cross-sectional SEM images and Auger depth profiles of Au-Si alloy films and NPG. (a, b) Before dealloying and (c, d) after etching.[20]

CV experiment is carried out in 0.5 M H_2SO_4 solution at a scan rate of 100 mV s^{-1} from −0.25 to 1.8 V and the roughness factor (real surface area/geometric surface area) of the NPG films was calculated from reduction area of CV. During the CV, oxidation and reduction reactions successively carried out at the surface of the NPG, which cleans the surface. We operated at least 10 cycles of CV for stabilization of the response. Figure 3.5 shows typical CV data taken from a NPG sample. The oxidation take place at approximately 1.1 V during the positive scan, which is lower than E^0 ($Au + 3H_2O = Au_2O_3 + 6H^+ + 6e^-$, E^0 = 1.457 V) because surface atoms are much more active than bulk atoms.[24] The broad peak of the oxidation is observed and it is attributable to the gradual changes in the nature of the oxide film formation.[24] On the other hand, the reduction peak occurred at approximately 0.9 V during the backward sweep, the area of which was used for calculating the roughness factor. The roughness factor of our NPG surface was around 33 (conversion factor = 450 μC/cm^2 [25]), which is larger than that of NPG surface made by etching in HF (～25).[2] When an Au-Si alloy is etching in HF, the dealloying reaction is very fast. It takes only a few seconds for entire dealloying of a 300 nm-thick Au–Si layer. As a results, the thickness of the NPG layer is reduced by 33% compared with Au–Si layer by partial dissolution of Au, because the diffusion of Au is not fast enough to catch up with the dissolution rate of Si atoms. In contrast, ethcing in KOH solution is a slow and moderate process that does not reduce the thickness of the alloy layer so that roughness factor is much more high.

Our NPG sensor was tested for sensing performance of detection of aniline. Aniline, which comprises a planar benzene ring with one amino group, is very commonly used in modern industrial materials such as dye, rubber, fungicides, and herbicides. Due to its high toxicity, treatment of aniline-containing waste is very important. Chromatography can detect the aniline in the water very sensitively,[26]; however, the equipment required for chromatography are very expensive and the analytical procedures are complicated. Sensing aniline with an amperometric sensor has the advantages of cost-effectiveness, sensitivity, simplicity, and compact size. Figure 3.6 shows cyclic voltammograms of NPG samples in PBS solution (pH 7.2), performed with a scan rate of 100 mV s^{-1} from 0 to 1.1 V in the absence and presence of 1.6 mM aniline. The oxidation of aniline is carried out and a broad anodic peak at 0.7–1.1 V for 1.6 mM aniline was observed. Aniline is oxidized to a free radical, which easily dimerizes to benzidine or *p*-aminodiphenylamine.[27-30] Hence, there is no corresponding reduction peak in the negative scan.

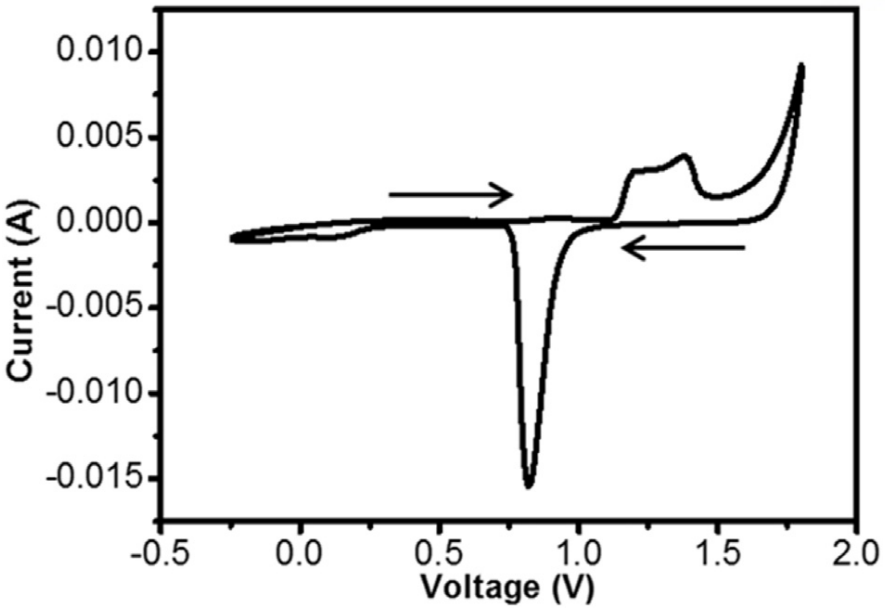

Figure 3.5 Cyclic voltammogram of NPG film in 0.5 M sulfuric acid.[20]

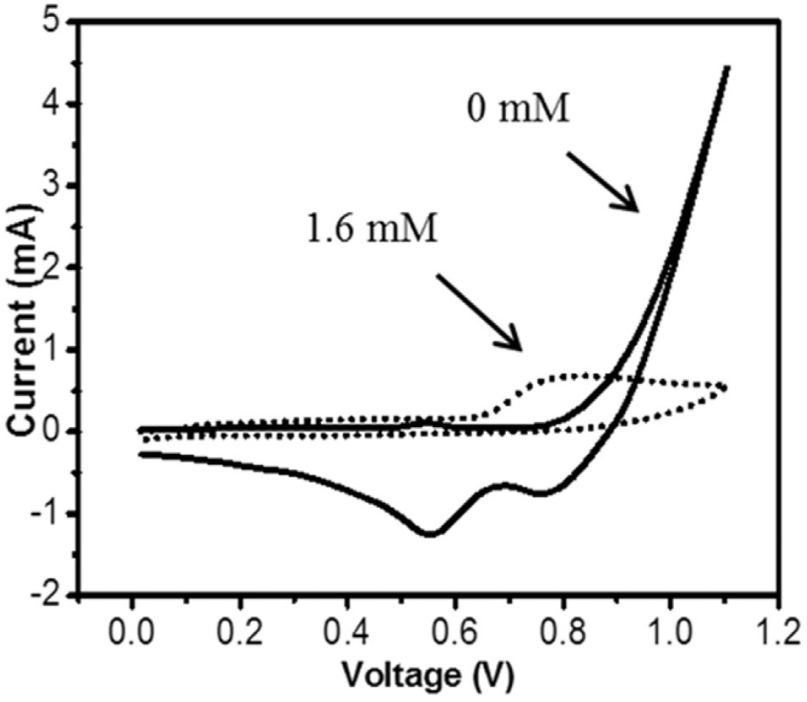

Figure 3.6 Cyclic voltammogram of NPG film absence and presence of 1.6 mM of aniline in PBS solution.[20]

Figure 3.7 (a) shows the amperometric sensing results of current–time response sensing in PBS solution. The current response was measured at the constant voltage of 0.8 V for successive additions of 10 μM aniline. In order to obtain a steady-state current response, we added the aniline at constant time intervals of 50 s. After the addition of 10 μM aniline, a rapid increase in current was observed, indicating oxidation of aniline on the NPG electrode surface. We added the 10 μM of aniline and obtained a step-like current increase. A highly linear correlation between the current and aniline concentration was obtained from 10 to 40 μM, with a correlation constant, R^2, of 0.978 and a sensitivity of 30 nA μM^{-1} (figure 3.7 (b)). We also performed the amperometric sensing experiments in the tap water to test the performance of the NPG sensor under more general conditions. Excellent aniline sensing performance was also confirmed (figure 3.8 (a)), with a linear current response from 0.5 to 60 μM with a sensitivity of 207 nA μM^{-1} (R^2 = 0.976; figure 3.8 (b)). The lower detection limit was 0.5 μM (S/N > 3) in tap water (figure 3.8 (c)). If the aniline was added more than 30 μM, the sensitivity was lightly decreased because of polymeric fouling of aniline on the NPG surface.[2] The fouling originating from polymeric accumulation at the electrode surface blocks the active sites for the electrochemical reaction, resulting deactivation of the electrode and lower sensitivity. When the aniline was added more than 70 μM, a poor linear response was obtained because of more serious fouling. Compared to previous results observed for NPG sensors made on Si wafers using HF solution (linear from 0.5 to 40 μM with a sensitivity of 350 nA μM^{-1} and R^2 = 0.995),[2] the NPG films on glass substrates fabricated here showed a lightly lower level of sensitivity; however, they showed a much wider linear sensing range because of the increased surface area of the NPG made by slow and moderate dealloying in KOH solution. The main advantages of our NPG films are the safe and simple preparation method, large roughness factor, and use of a glass substrate that is cheap and readily available. Our method will be very useful for producing NPG, not only for sensors but also for many other applications such as actuators and catalysis.

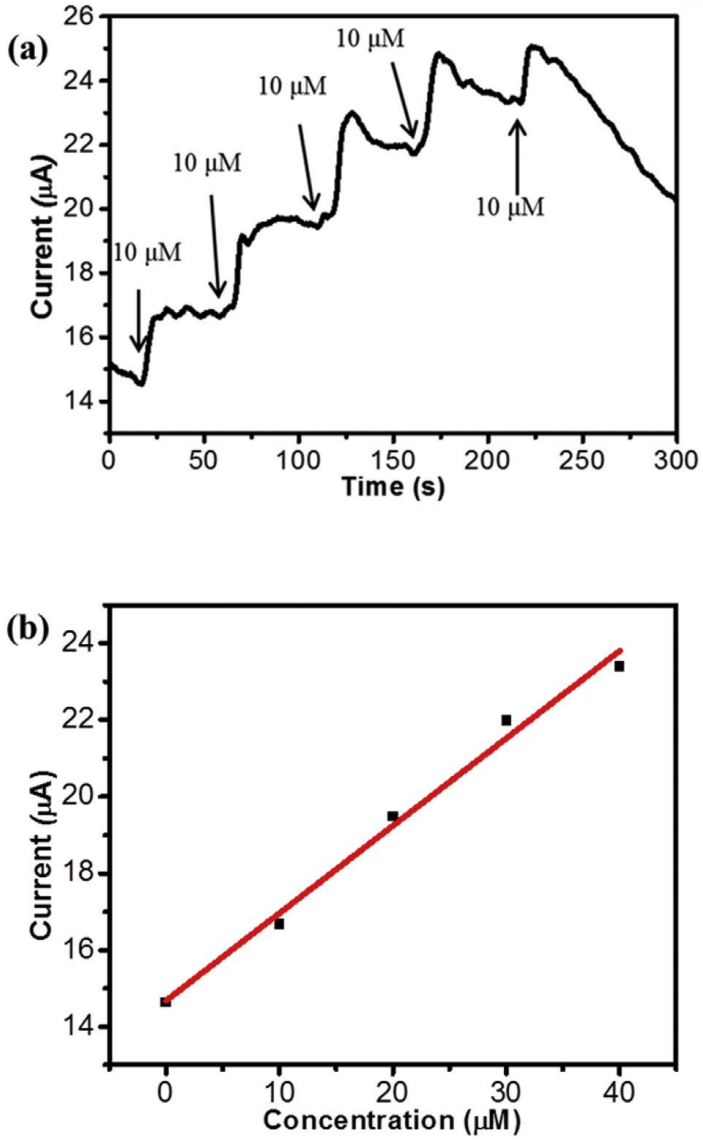

Figure 3.7 Sensing performance of NPG in PBS solution. (a) Time-current response at constant voltage of 0.8 V with successive additions of 10 mM aniline into PBS solution and (b) calibration curve of (a).[20]

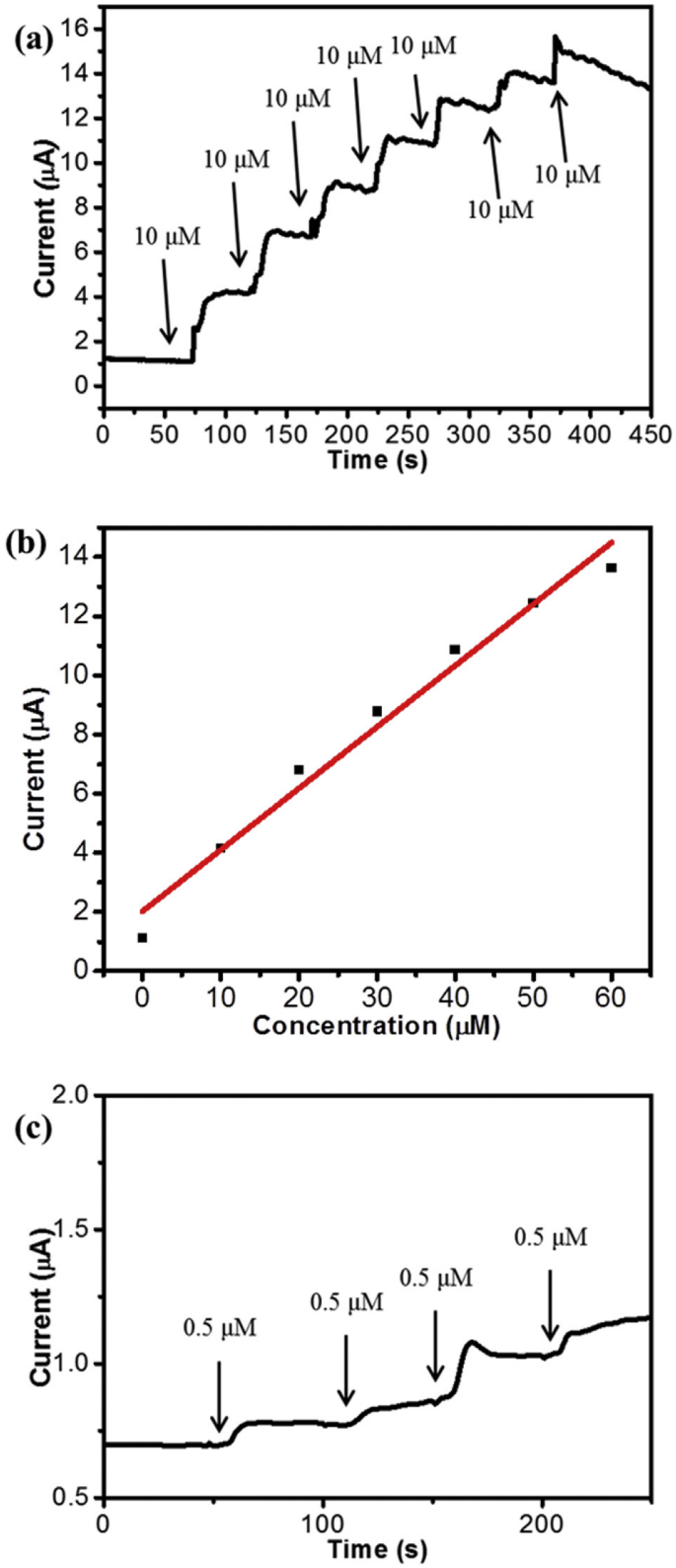

Figure 3.8 Sensing performance of NPG in tap water. (a) Time-current response at constant voltage of 0.8 V with successive additions of 10 mM aniline and (c) 0.5 mM aniline into tap water and (b) calibration curve of (a).[20]

3.4 Conclusion

We made NPG films on glass substrates by etching a co-sputtered Au–Si alloy. By optimized annealing treatment which reduces the residual stress in the films, we could solve the delamination of the NPG films from the glass substrates. A nanoporous structure was fabricated by etching the Au–Si films with heated KOH solution. The roughness factor of the NPG surface etched with KOH was much larger than that of NPG structures fabricated by fast HF dealloying. The slower dissolution rate of Si atoms in the heated KOH etchant prevented the delamination of films. As a results, thicker NPG films with a larger roughness factor was obtained. We tested the performance of NPG films as sensors for detecting aniline and confirmed that they exhibited a low detection limit and wide sensing range. We believe that our environmentally friendly and cost-effective way of fabricating NPG sensors can be applicable to other kinds of substrates, such as flexible polymeric substrates.

3.5 References

1. Yan, X.; Meng, F.; Cui, S.; Liu, J.; Gu, J.; Zou, Z., Effective and rapid electrochemical detection of hydrazine by nanoporous gold. *Journal of Electroanalytical Chemistry* **2011,** *661* (1), 44-48.
2. Quynh, B. T. P.; Byun, J. Y.; Kim, S. H., Nanoporous gold for amperometric detection of amino-containing compounds. *Sensors and Actuators B: Chemical* **2014,** *193*, 1-9.
3. Liu, Z.; Du, J.; Qiu, C.; Huang, L.; Ma, H.; Shen, D.; Ding, Y., Electrochemical sensor for detection of p-nitrophenol based on nanoporous gold. *Electrochemistry Communications* **2009,** *11* (7), 1365-1368.
4. Yudha S, S.; Kusuma, I.; Asao, N., Aerobic oxidation of hydroxylamines with nanoporous gold catalyst as an efficient synthetic method of nitrones. *Tetrahedron* **2015,** *71* (37), 6459-6462.
5. Wittstock, A.; Zielasek, V.; Biener, J.; Friend, C. M.; Bäumer, M., Nanoporous Gold Catalysts for Selective Gas-Phase Oxidative Coupling of Methanol at Low Temperature. **2010,** *327* (5963), 319-322.
6. Detsi, E.; Onck, P.; De Hosson, J. T. M., Metallic Muscles at Work: High Rate Actuation in Nanoporous Gold/Polyaniline Composites. *ACS Nano* **2013,** *7* (5), 4299-4306.
7. Detsi, E.; Chen, Z. G.; Vellinga, W. P.; Onck, P. R.; Hosson, J. T. M. D., Actuating and Sensing Properties of Nanoporous Gold. *Journal of Nanoscience and Nanotechnology* **2012,** *12* (6), 4951-4955.
8. Biener, J.; Wittstock, A.; Zepeda-Ruiz, L. A.; Biener, M. M.; Zielasek, V.; Kramer, D.; Viswanath, R. N.; Weissmüller, J.; Bäumer, M.; Hamza, A. V., Surface-chemistry-driven actuation in nanoporous gold. *Nature Materials* **2009,** *8* (1), 47-51.
9. Erlebacher, J.; Aziz, M. J.; Karma, A.; Dimitrov, N.; Sieradzki, K., Evolution of nanoporosity in dealloying. *Nature* **2001,** *410* (6827), 450-453.
10. Huang, J.-F.; Sun, I.-W., Fabrication and Surface Functionalization of Nanoporous Gold by Electrochemical Alloying/Dealloying of Au–Zn in an Ionic Liquid, and the Self-Assembly of L-Cysteine Monolayers. **2005,** *15* (6), 989-994.
11. Rouya, E.; Reed, M. L.; Kelly, R. G.; Bart-Smith, H.; Begley, M.; Zangari, G. Synthesis of Nanoporous Gold Structures via Dealloying of Electroplated Au-Ni Alloy Films. ECS, 2007.
12. Synthesis of Nanoporous Gold Structures via Dealloying of Electroplated Au-Ni Alloy Films. *ECS Meeting Abstracts* **2007**.
13. Gupta, G.; Thorp, J. C.; Mara, N. A.; Dattelbaum, A. M.; Misra, A.; Picraux, S. T., Morphology and porosity of nanoporous Au thin films formed by dealloying of AuxSi1−x.

2012, *112* (9), 094320.

14. Qiu, H.; Xue, L.; Ji, G.; Zhou, G.; Huang, X.; Qu, Y.; Gao, P., Enzyme-modified nanoporous gold-based electrochemical biosensors. *Biosensors and Bioelectronics* **2009,** *24* (10), 3014-3018.
15. Collinson, M. M., Nanoporous Gold Electrodes and Their Applications in Analytical Chemistry. *ISRN Analytical Chemistry* **2013,** *2013*, 692484.
16. Chen, L. Y.; Lang, X. Y.; Fujita, T.; Chen, M. W., Nanoporous gold for enzyme-free electrochemical glucose sensors. *Scripta Materialia* **2011,** *65* (1), 17-20.
17. El-Said, W. A.; Lee, J.-H.; Oh, B.-K.; Choi, J.-W., 3-D nanoporous gold thin film for the simultaneous electrochemical determination of dopamine and ascorbic acid. *Electrochemistry Communications* **2010,** *12* (12), 1756-1759.
18. Tang, Y. Y.; Kao, C. L.; Chen, P. Y., Electrochemical detection of hydrazine using a highly sensitive nanoporous gold electrode. *Analytica chimica acta* **2012,** *711*, 32-9.
19. Quynh, B. T. P.; Byun, J. Y.; Kim, S. H., Non-enzymatic amperometric detection of phenol and catechol using nanoporous gold. *Sensors and Actuators B: Chemical* **2015,** *221*, 191-200.
20. Lee, K.-U.; Tran, T. H.; Kim, S. H.; Shin, H.-J., Fabrication of nanoporous gold thin films on glass substrates for amperometric sensing of aniline. *Journal of Alloys and Compounds* **2017,** *713*, 132-137.
21. Hoogvliet, J. C.; van Bennekom, W. P., Gold thin-film electrodes: an EQCM study of the influence of chromium and titanium adhesion layers on the response. *Electrochimica Acta* **2001,** *47* (4), 599-611.
22. Husna, J.; Aliyu, M. M.; Islam, M. A.; Chelvanathan, P.; Hamzah, N. R.; Hossain, M. S.; Karim, M. R.; Amin, N., Influence of Annealing Temperature on the Properties of ZnO Thin Films Grown by Sputtering. *Energy Procedia* **2012,** *25*, 55-61.
23. Fang, W.; Lo, C.-Y., On the thermal expansion coefficients of thin films. *Sensors and Actuators A: Physical* **2000,** *84* (3), 310-314.
24. Burke, L. D.; Nugent, P. F., The electrochemistry of gold: I the redox behaviour of the metal in aqueous media. *Gold Bulletin* **1997,** *30* (2), 43-53.
25. Tan, Y. H.; Davis, J. A.; Fujikawa, K.; Ganesh, N. V.; Demchenko, A. V.; Stine, K. J., Surface area and pore size characteristics of nanoporous gold subjected to thermal, mechanical, or surface modification studied using gas adsorption isotherms, cyclic voltammetry, thermogravimetric analysis, and scanning electron microscopy. *Journal of Materials Chemistry* **2012,** *22* (14), 6733-6745.
26. Riggin, R. M.; Cole, T. F.; Billets, S., Determination of aniline and substituted derivatives in wastewater by gas and liquid chromatography. *Analytical Chemistry* **1983,** *55* (12), 1862-1869.

27. Mabbott, G. A., An introduction to cyclic voltammetry. *Journal of Chemical Education* **1983,** *60* (9), 697.

28. Cases, F.; Huerta, F.; Garcés, P.; Morallón, E.; Vázquez, J. L., Voltammetric and in situ FTIRS study of the electrochemical oxidation of aniline from aqueous solutions buffered at pH 5. *Journal of Electroanalytical Chemistry* **2001,** *501* (1), 186-192.

29. Mitadera, M.; Spataru, N.; Fujishima, A., Electrochemical oxidation of aniline at boron-doped diamond electrodes. *Journal of Applied Electrochemistry* **2004,** *34* (3), 249-254.

30. Spătaru, T.; Spătaru, N.; Fujishima, A., Detection of aniline at boron-doped diamond electrodes with cathodic stripping voltammetry. *Talanta* **2007,** *73* (2), 404-406.

CHAPTER 4
NANOPOROUS GOLD FOR SUPERCAPACITOR

4.1 Introduction

As to approaching huge need for electricity, a number of researchers have been studied next-generation energy systems such as battery[1], supercapacitor[2-4], fuel cell[5, 6], etc. Among these, supercapacitors are very attractive because of their high power density, fast charge-discharge rates and a long lifetime[7]. Supercapacitors store charges in two ways, using electric double layer capacitance(EDLC) and pseudocapacitor (figure 4.1). EDLC stores charges in an electric-double layer, which is similar to conventional capacitors. The stored charge of EDLC is proportional to the surface area of the electrode. EDLC has very long cycle life because of its principles. Pseudocapacitor stores charges by Faradaic reaction. Pseudocapacitive materials are oxidized and reduced by driven voltage, which is similar to a battery but its reaction rate is much faster. Pseudocapacitor has relatively lower cycle life than EDLC because pseudocapacitive materials are partially lost or degraded during the operation. Nevertheless, pseudocapacitors have 10-100 times higher capacitance than EDLC so that many researchers have been focused on pseudocapacitor[8-10]. Widely used materials for pseudocapacitor are metal oxides, such as RuO_2[11], MnO_2[8-10, 12], and metal sulfides, such as MnS[13], CoS[14], and conducting polymer such as polyaniline(PANI)[2, 15, 16], polypyrrole[4], etc. Generally, these pseudocapacitive materials are coated or deposited on conducting supports such as carbon materials[3, 4, 11], nickel foam[17], gold[18-20], etc, that work as current collector.

Among these pseudocapacitive materials, PANI is the very attractive materials because of its high capacitance, low cost, easy fabrication, manifold redox states, and environment-friendliness[18]. The electro-deposition of aniline monomer in acidic media is widely used for fabrication of PANI[21]. The low pH is essential for preparation of conductive PANI. Perchloric acid($HClO_4$), sulfuric acid(H_2SO_4), hydrochloric acid(HCl), phosphoric acid(HPO_4), and many other acids are commonly used as the acidic media and their anions highly affect the properties of PANI such as morphology, conductivity, and stability[22]. However, PANI suffers from stability issues like any other conducting polymers[2]. To improve a stability of PANI, a lot of methods were used such as changing the polymerization temperature, adding a small amount of additives during the polymerization process, making the porous structure of PANI, etc.[23, 24] Herein, we employed perchloric acid during the polymerization process to enhance the stability of PANI.

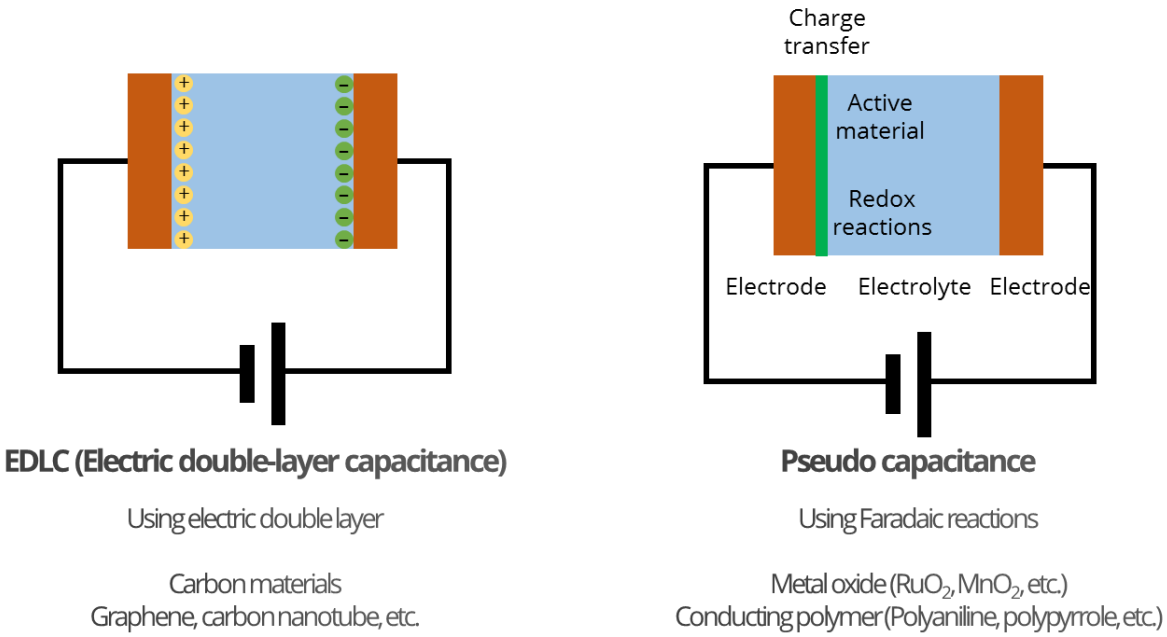

Figure 4.1 Schematic diagram of EDLC and pseudo capacitance

Nanoporous gold(NPG) which has a three-dimensional bi-continuous structures is a very promising and versatile material[25-27]. NPG is used in various field such as catalysis[28, 29], actuators[30], sensors[31-34], energy systems[5] and so on because of its great stability, high conductivity, large surface area, unique catalytic activity. Different from gold nanoparticles which are suffering from aggregation, leaching and losing their catalytic activity during chemical reactions, NPG save their catalytic activity during the reactions. There were various reports which use NPG as a support material for a pseudocapacitive material such as MnO_2[12], PANI[18], polypyrrole[19], and etc. In case of PANI/NPG, long-term stability was not reported and not known yet while NPG supercapacitor with metal oxides such as MnO_2 are highly stable even after 1000 cycles[35].

Herein, we fabricated PANI/NPG polymer-metal hybrid structures designed for greatly stable supercapacitor with high capacitance. NPG is commonly made by Au-Ag alloy using nitric acid, which is a toxic and expensive process[36]. We enhanced NPG fabrication process by first fabricating Au alloy using Magnesium (Mg) as the less noble element of the alloy and etching Mg from the binary alloy by diluted acetic acid. PANI was deposited on NPG by electrodeposition of aniline monomer in acidic media. To enhance the stability of the coated PANI, we compared sulfuric acid(H_2SO_4) and perchloric acid($HClO_4$) for the electropolymerization of PANI. PANI from sulfuric acid had low stability while PANI from perchloric acid had a much better stability. We optimized the influencing factors during electropolymerization procedure including the concentration of acid and aniline, the types of acid, applied voltage and polymerization time. Under optimum conditions, our PANI/NPG supercapaccitor showed an excellent performance with high capacitance and excellent long-term stability.

4.2 Experimental

Fabrication of NPG

We deposited Au-Mg alloy films on Si substrates by sputtering[32, 37]. Si substrates (1 cm × 2 cm) were successively cleaned by acetone, ethanol, and deionized water. Ti (5 nm), Au (40 nm), and Au-Mg alloys (200 nm) were sputtered on cleaned Si substrates. The base pressure of sputtering chamber was less than 2×10^{-6} Torr. We controlled the concentration of Au and Mg for high porosity of NPG. We immersed the as-deposited films into 5 wt% of acetic acid solution for making nanoporous structures. Mg was selectively removed within 30 min.

Coating the PANI on NPG

PANI was coated on NPG by electrodeposition with a conventional three electrode and potentiostat (Versastat 3, Princeton Applied Research). The counter electrode and reference electrode was platinum wire and Ag/AgCl(3 M), respectively. Dealloyed NPG films from Au-Mg alloy were used as working electrode. Only 1.2 cm^2 area of NPG is immersed into an electrolyte and coated with PANI. The electrolytes were 1 M sulfuric acid solution containing 10 mM aniline and 1 M perchloric acid solution containing 10 mM aniline. We altered the concentration of aniline (1 mM ~ 100 mM) and time for electro-deposition (30 min ~ 2 h) and optimized the coating condition (10 mM and 1 h). Cyclic voltammetry and chrono-potentiometry were carried out for coating the PANI. For cyclic voltammetry, potential window was -0.2 V to 1.5 V with scan rates of 50 mV and 100 mV. For chrono-potentiometry, constant current of 0.5 mA was applied for 60 min. After electro-deposition of PANI, the PANI/NPG samples were cleaned with deionized water and dried in the oven at 110 ^oC for 1 day.

Electrochemical methods

The PANI/NPG films were used as the working electrode in a conventional three electrode system (Versastat 3, Princeton Applied Research). The electrolyte was 1 M perchloric acid. We operated cyclic voltammetry(CV) with the voltage range of – 0.2 V to 0.8 V with the scan rate of 10 mV/s. Areal and volumetric capacitance was calculated from $\mathrm{C(F}/cm^2) = \frac{1}{2\upsilon S(V_2-V_1)}\int_{V_1}^{V_2} idV$ and $\mathrm{C(F}/cm^3) = \frac{1}{2\upsilon v(V_2-V_1)}\int_{V_1}^{V_2} idV$, where ν, S, V_2, V_1, i, v is potential scan rate, area of electrode, initial and final potential of CV, instant current, and volume of electrode, respectively. The galvanostatic charge-discharge experiments were also conducted with the same electrolyte and potential range. Areal capacitance was calculated from $\mathrm{C(F}/cm^2) = \frac{I\Delta t}{S\Delta V}$ and $\mathrm{C(F}/cm^3) = \frac{I\Delta t}{v\Delta V}$ where I, Δt, S, ΔV and v is discharging current, discharge time, the area of electrode, voltage range during the discharge process, and volume of electrode, respectively. In order to compare the capacitance reported by other researches in the literature, we used the equation $C_{th} = 4C_{tw}$, where the C_{th} and C_{tw} are the capacitance for the three-electrode cell and two-electrode cell, respectively[38, 39]. The energy density and power density are calculated from $\mathrm{E} = \frac{1}{2}C_{tw}V^2$, $\mathrm{P} = \frac{E}{\Delta t}$.

4.3 Results and discussions

Figure 4.2 shows the schematic of the fabrication process of our NPG substrates. The substrates comprise a NPG thin layer, an Au protection layer, and a Ti adhesion layer on a silicon substrate. Fabrication method is analogous to our previous study[32, 37], but in this study we used Mg as a sacrificial element of the alloy as Mg is much easier to etch out while similar alloy formation is expected between Au-Si and Au-Mg alloys. We etched the Au-Mg alloy by immersing the samples into 5 wt% acetic acid for 30 min. In general, nanoporous gold is fabricated from Au binary alloys that compose gold and sacrificial elements, typically silver. Toxic acids such a nitric acid are used for dealloying the sacrificial element while diluted acetic acid for dealloying Mg in this study is environmentally friendly and safe. Also, Mg is much economical than silver. Mg was rarely tried to prepare nanoporous gold structures[40].

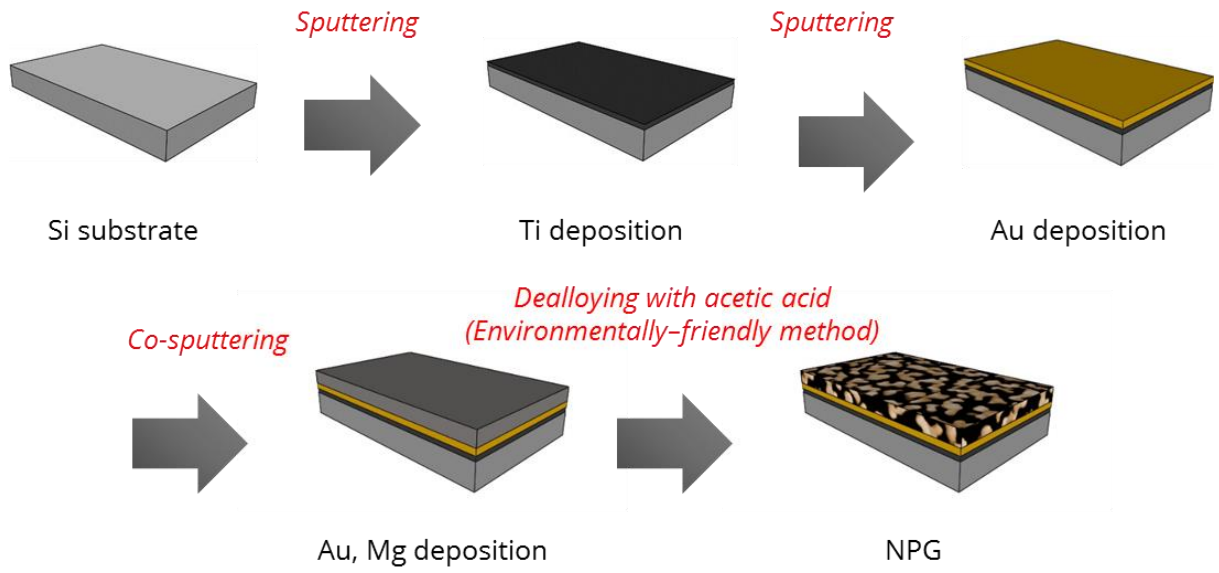

Figure 4.2 Schematic of fabrication process of NPG[41]

Figure 4.3 shows Auger electron spectroscopy (AES) depth profiles before and after dealloying the alloy samples. The atomic ratio of Au-Mg alloy was $Au_{20}Mg_{80}$. It can be seen that after etching, magnesium was almost extracted by diluted acetic acid with a little amount of magnesium remained as residue. X-ray diffraction(XRD) patterns indicated that three different phase in the Au-mg alloy, i.e., magnesium, gold-magnesium alloy, and gold (figure 4.4 (a)). After etching, only peaks from gold were observed, which coincide with AES data (figure 4.4 (b)). The intermetallic compound of gold and magnesium was made during the co-sputtering, and this intermetallic compound was easily dissolved by diluted acetic acid.

Figure 4.5 shows scanning electron microscopy(SEM) images of NPG samples from (a) Au-Mg alloy and (b) Au-Ag alloy. We prepared Au-Ag alloy films for comparison and Au-Ag alloy films were dealloyed in 70 % nitric acid. Comparing the two samples, NPG from Au-Mg alloy shows angular shape and NPG from Au-Ag alloy has rounded ligaments, however, difference is not that much. Figure 4.5 (c) shows cyclic voltammogram in 0.5 M H_2SO_4 solution which is a typical method for examining the surface area of nanoporous gold. Both results are almost same. Hence, we believed that NPG from Au-Mg alloy is similar to NPG from Au-Ag alloy and we used Au-Mg alloy for NPG. The size of the ligament and pore was around 80 nm both of NPGs from Au-Mg alloys and Au-Ag alloys.

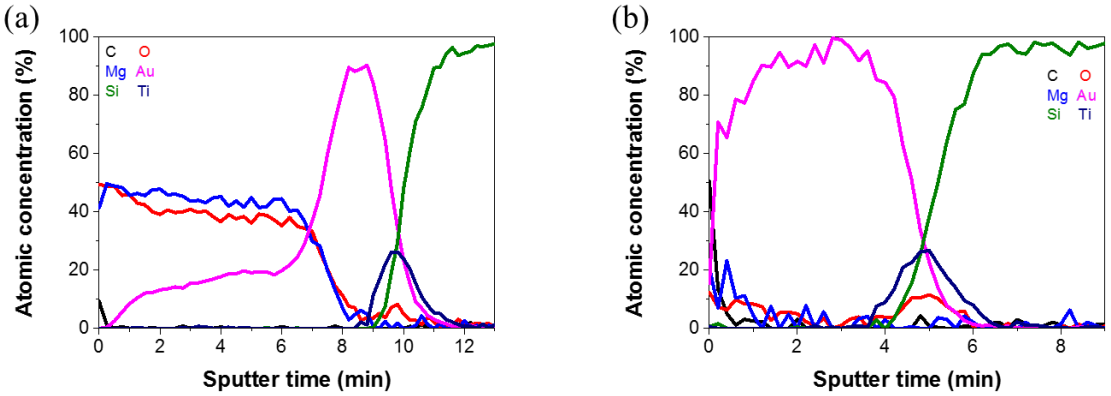

Figure 4.3 AES depth profiles of (a) Au-Mg alloy (before etching) and (b) NPG (after etching)[41]

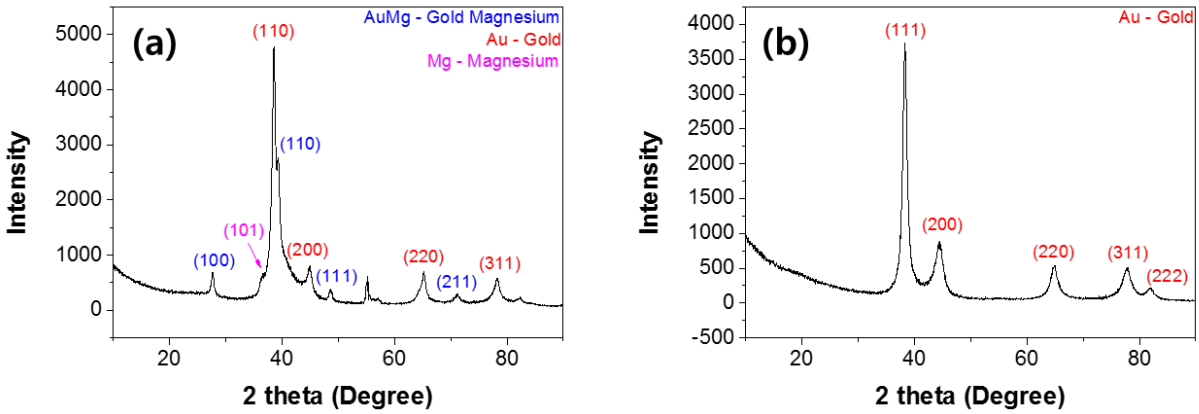

Figure 4.4 XRD results of an Au-Mg alloy (a) before and (b) after ethcing. In the alloy, three phases were observed while only Au peaks were observed in NPG.[41]

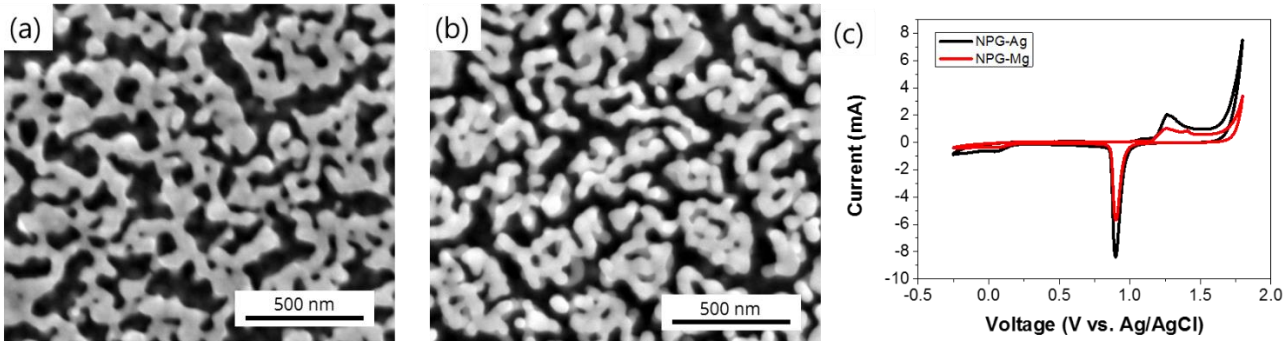

Figure 4.5 SEM images of NPG from (a) Au-Mg alloy and (b) Au-Ag alloy. (c) Cyclic voltammogram of NPGs in 0.5 M H_2SO_4 solution.[41]

After that, we deposited PANI on the NPG films from Au-Mg alloys. As described above, electro-polymerization of aniline is always performed in strong acidic electrolytes because the deposited films consist of a low chain of oligomers at high pH, not leading to polymerization[21]. For this reason, sulfuric acid (H_2SO_4) is widely used as the acidic media for electrodeposition of PANI because PANI layers prepared in sulfuric acid have high conductivities[42]. However, the PANI coated with sulfuric acid suffers from poor stability. To solve this issue, we used perchloric acid($HClO_4$) rather than sulfuric acid. We fabricated PANI/NPG films both in sulfuric acid and in perchloric acid and compared their stabilities. While PANI/NPG films from sulfuric acid were peeled off from the substrate in a few cycles of charge-discharge reactions, PANI/NPG films from perchloric acid exhibited much better stability after few hundred cycles. We will discuss this point later more in detail.

It is a great challenge to uniformly coat the PANI on the NPG because NPG has a number of curved and convoluted ligament and the charge can be easily concentrated to the topmost area of ligament and oxidation reaction of aniline monomer could be carried out only at the topmost area resulting partial coating of PANI on NPG. Indeed, when we tried to coat the PANI on the NPG by cyclic voltammetry (CV) with various scan rate, the PANI was only coated on the top area of NPG films not inside of the films. In order to solve this problem, we performed chrono-potentiometry with constant current of 0.5 mA. Chrono-potentiometry is maintain a constant current to working electrode so that the rate of electrochemical reaction will be controlled and PANI coating would be uniform. Using this technique, we could uniformly deposit the PANI on the entire surface in and out of NPG films. In addition, we optimized the coating time and concentration of aniline. The capacitance showed highest value at the coating time of 60 min and if the coating time was more than 60 min, the capacitance was rather decreased. This may because the PANI block the holes of ligament and active surface area was decreased. With a longer deposition time up to 120 min, the PANI/NPG structures became very weak and were peeled off from the substrate. In case of concentration of aniline, if the concentration was too low (1 mM), the capacitance was very low and when the concentration was high (100 mM), PANI was excessively coated and it blocked the pores of NPG structures (figure 4.6 (b)). In this way, we varied the concentration of aniline and coating times with the same current of 0.5 mA for chrono-potentiometry. The optimum coating condition was 10 mM of aniline and coating time of 60 min. We took SEM images and compared the before and after coating the PANI on NPG with optimum condition and they are shown in figure 4.7. It can be seen that even after electrodeposition of PANI, pores of NPG were still not blocked (figure 4.7 (b)). It demonstrates that PANI layer was not too thick and uniformly coated on NPG structures.

Coating the PANI with proper thickness in uniform is very important. It is ideal to load pseudo-capacitance material on the conducting support as much as possible to maximize the capacitance of the supercapacitor, which can be increasing the thickness of the pseudo-capacitance material. On the other

hand, when the thickness increases too much, the resistance of the electrode also increases and ions are prohibited from accessing the active sites inside the thick coating[43]. Therefore, it is highly recommended optimizing the thickness of a PANI considering this trade-off. For NPG, one more important thing to consider is that pores in NPG should not be blocked by polymer coating because they work as a passage of gas or liquid and help the mass transport during reaction.

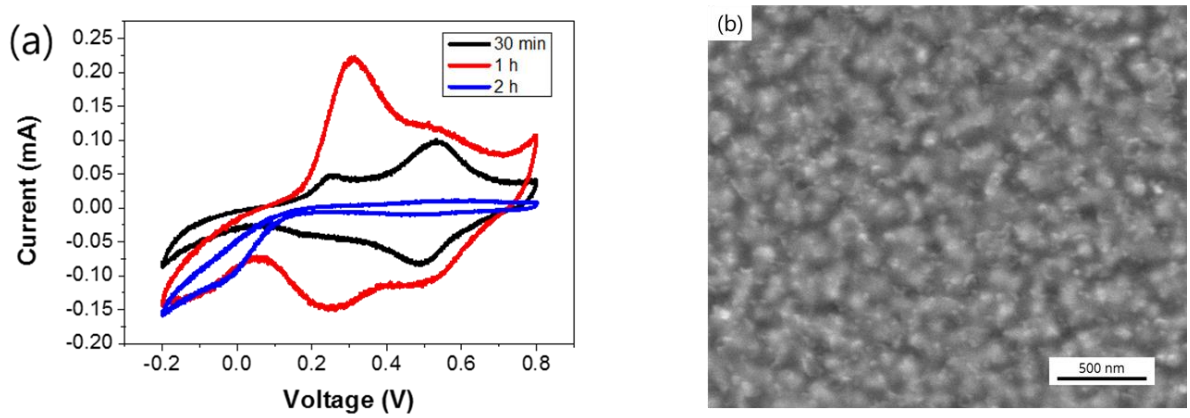

Figure 4.6 (a) Cyclic voltammogram of PANI/NPG with different coating times. (b) SEM image of PANI/NPG prepared in a high concentration of aniline (100 mM). The pores were blocked by PANI layer.[41]

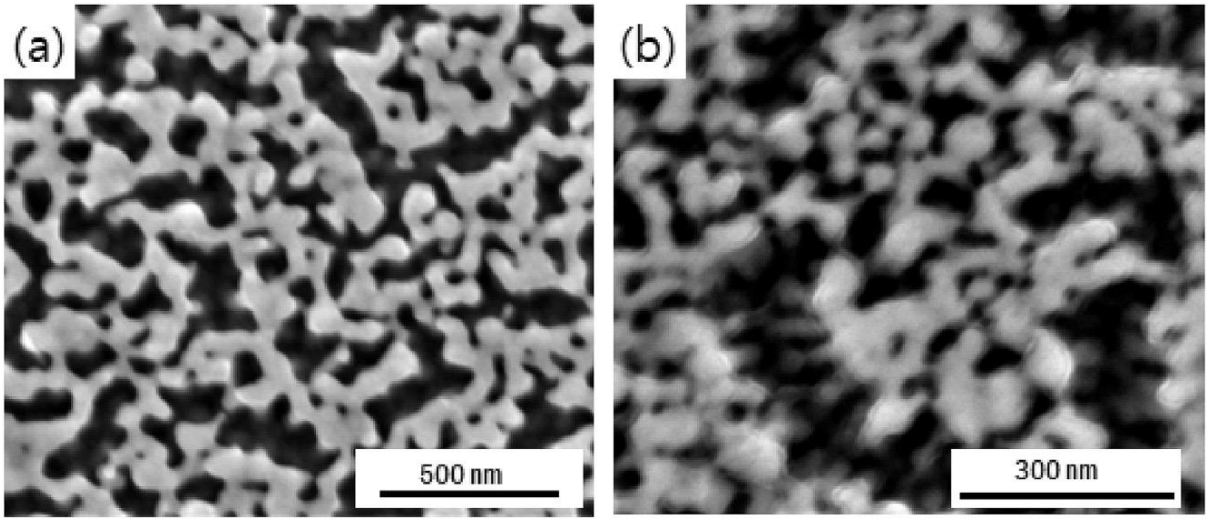

Figure 4.7 SEM images of (a) bare NPG from Au-Mg and (b) PANI/NPG[41]

To observe the PANI/NPG structure more deeply, we took transmission electron microscope(TEM). Figure 4.8 shows TEM images of PANI/NPG structures. To figure out the PANI film layer and epoxy layer used for preparation of TEM specimen, we deposited a thin (~ 40 nm) chrome layer on the nanostructure that is shown as a layer in gray color on the NPG ligaments. In figure 4.8 (a), we observe two layers on NPG ligaments. One is PANI layer which is shown as white and about 10 nm thick. On top of the PANI layer, a chrome layer is seen as gray and about 40 nm thick. It can be seen that PANI is homogeneously coated on the whole NPG ligaments with uniform thickness. Figure 4.8 (b) shows a zoom-in image of figure 4.8 (a) and it shows the PANI coating on NPG structures more in detail.

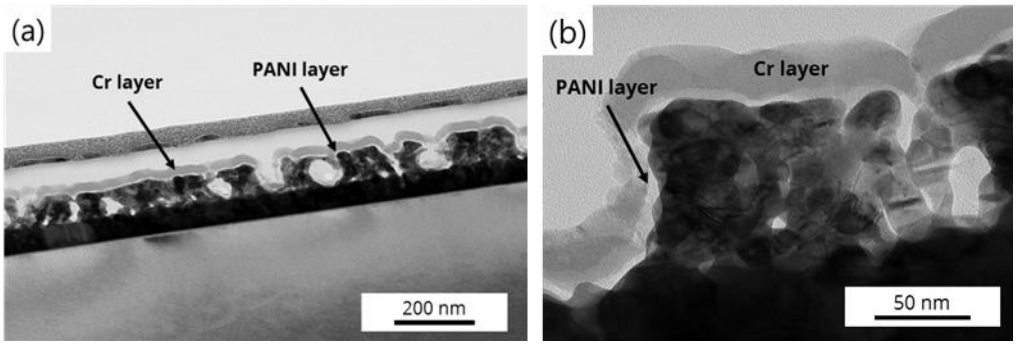

Figure 4.8 (a) Cross-sectional TEM images of PANI/NPG. (b) Zoomed-in image of (a). For the sample preparation, the chrome layer was deposited on the PANI/NPG structure. In the images, chrome layer was seen as gray. PANI layer was seen as white between the chrome layer and NPG structure.[41]

We also employed Fourier transform infrared reflectance (FTIR) to characterize the PANI/NPG structure. FTIR results of PANI/NPG is shown in figure 4.9. The peaks around 3300 cm^{-1} indicate the presence of N-H stretching of amine. C-N stretching of secondary aromatic amine was identified with 1302.13 cm^{-1} and 1253.41 cm^{-1}. The peaks of 1577.17 cm^{-1} and 1497.83 cm^{-1} correspond to quinoid and benzenoid rings. These peaks are very similar to the typical infrared spectrum of PANI.[2, 15, 43] The FTIR results confirm that PANI was successfully coated on the NPG structure.

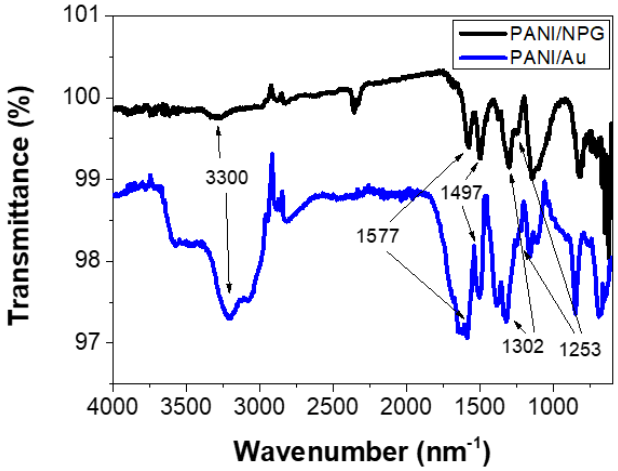

Figure 4.9 FTIR results of PANI/NPG (black line) and PANI on plane gold substrate (blue line).[41]

Electrochemical performance of our PANI/NPG samples was carried out in a potentiostat by cyclic voltammetry and galvanostatic charge-discharge. Figure 4.10 (a) shows cyclic voltammetry results of PANI/NPG and bare NPG in 1 M perchloric acid with a scan rate of 10 mV/s. While the bare NPG that shows only a electrochemical double layer (EDLC) capacitance, PANI/NPG shows distinct oxidation and reduction peaks which indicate pseudo-capacitance behavior, and the capacitance was much large. The oxidation and reduction mechanism of PANI is well known[44] and the areal capacitance calculated from the CV was 6.54 mF/cm^2 (327 F/cm^3). The areal capacitance(F/cm^2) and volumetric capacitance(F/cm^3) are more reliable values than specific capacitance(F/g) because errors in mass measurements can significantly inflate the specific capacitance. Detailed calculation methods were shown in Part 4.5. We conducted CV with different scan rates (figure 4.10 (b)). Our PANI/NPG sample showed pseudo-capacitor characteristics even at a fast scan rate of 100 mV/s. The galvanostatic charge-discharge experiments were also carried out with various current densities (figure 4.10 (c)). The areal capacitance of the PANI/NPG structures was calculated from galvanostatic charge-discharge. They were 5.25 mF/cm^2(262.5 F/cm^3), 4.17 mF/cm^2(208.3 F/cm^3), 3.61 mF/cm^2(180.8 F/cm^3), 3.23 mF/cm^2(161.3 F/cm^3), and 2.9 mF/cm^2(145 F/cm^3) at the current level of 0.3 mA, 0.5 mA, 0.7 mA, 0.9 mA, and 1.2 mA, respectively. Compared to other microscale supercapacitors, our supercapacitors showed high areal capacitance (0.51 mF/cm^2 for graphene oxide supercapacitor[45], 0.48 mF/cm^2 for MnOx based supercapacitor[46]). Our PANI/NPG supercapacitors had maximum energy density of 9.11 mWh/cm^3 at power density of 1.56 W/cm^3. This remarkable high capacitance of PANI/NPG supercapacitor based on the combination of the rational thickness of PANI and greatly conductive NPG with three-dimensional open pore structures which is effective for fast ion diffusions. Additionally, the broad surface area of NPG could load a large amount of PANI for high capacitance. We believe that the open porous structure still remaining after the coating of PANI greatly improved the performance of the supercapacitor.

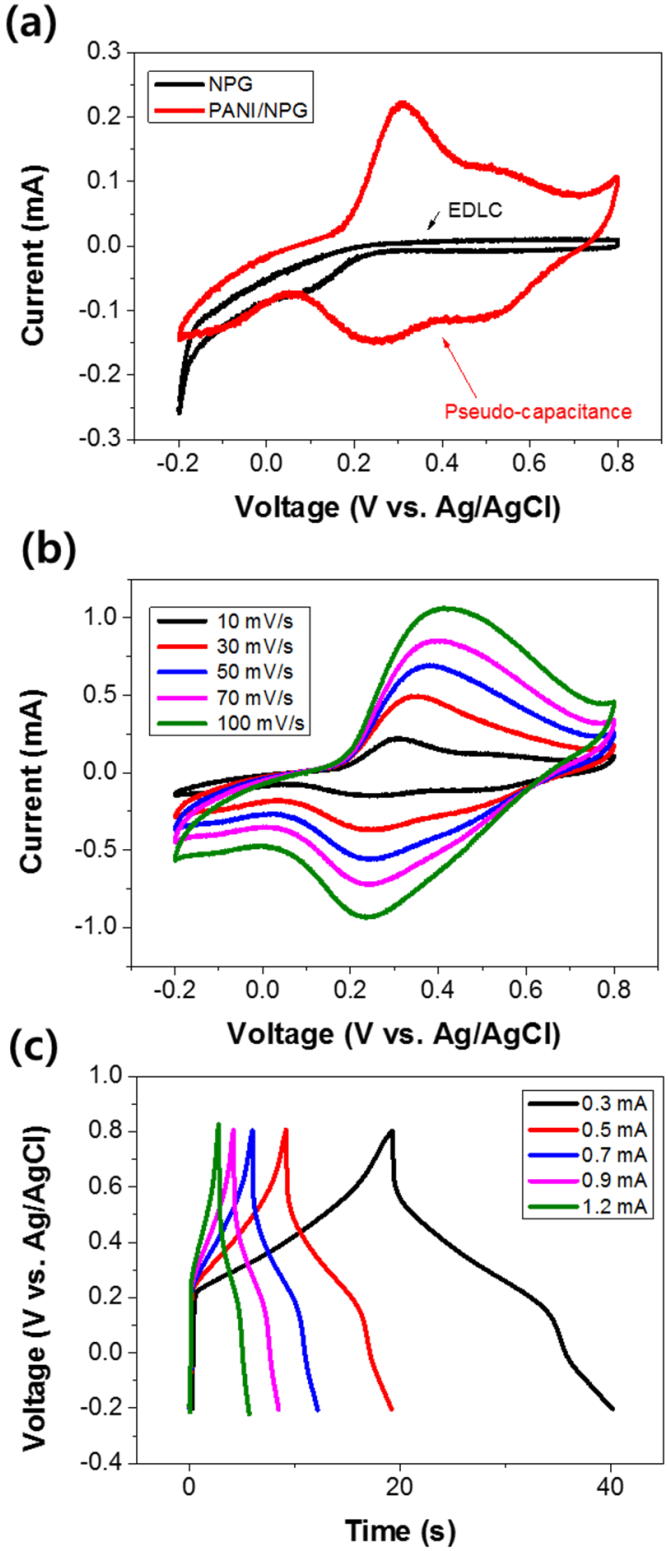

Figure 4.10 Electrochemical results of PANI/NPG supercapacitors. (a) Cyclic voltammogram of pure NPG and PANI/NPG, (b) Cyclic voltammogram of PANI/NPG with different scan rates, (c) Galvanostatic charge-discharge of PANI/NPG with diffreent currents.[41]

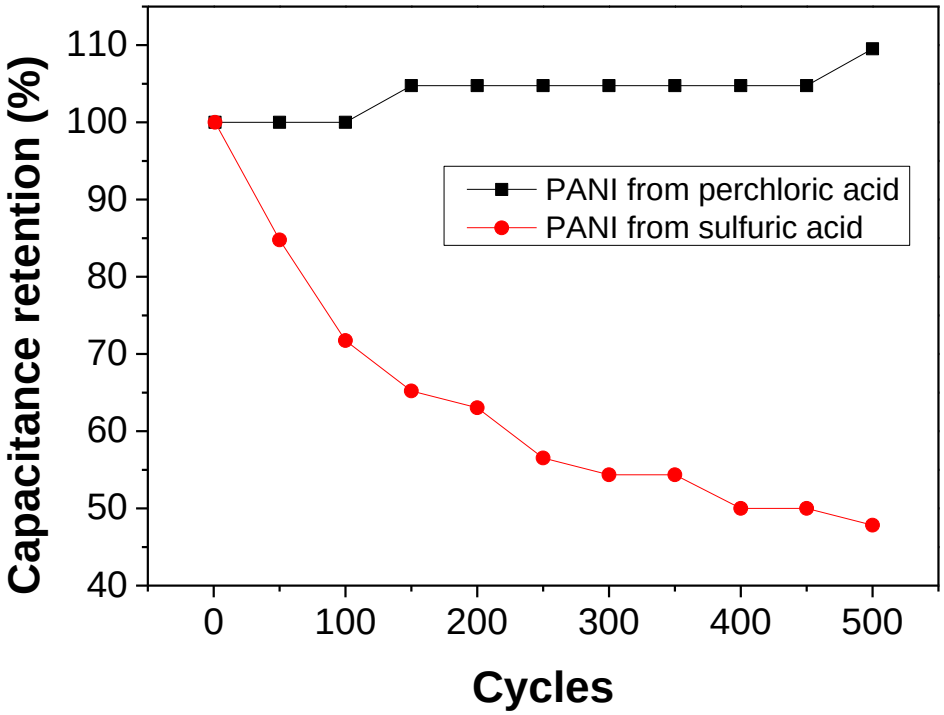

Figure 4.11 Cycling tests of PANI/NPG fabricated from different acids.[41]

Regarding the stability of our supercapacitors, Figure 4.11 shows the cycle life graph of PANI/NPG at the current density of 1.2 mA for 500 cycles. The capacitance was almost unchanged after 500 cycles. In contrast to this, PANI/NPG prepared in sulfuric acid was degraded within 100 cycles. This phenomenon can be understood as follows. 1) Using chrono-potentiometry, we could make uniform PANI on the whole ligaments of NPG including the inside of the pores. 2) During the polymerization, anions from acid were incorporated into PANI and affected properties of the PANI layers. In case of sulfuric acid, the deposited film is easily swelled so that it has a short lifespan because that its anion(SO_4^{2-}) is large. In contrast to this, ClO_4^- from perchloric acid is a relatively small anion and the deposited films have compact structures[47]. The much longer cycle lifespan of PANI/NPG prepared in perchloric acid was mainly due to the formation of compact PANI layer on the NPG structure that was possible by the optimized gentle chrono-potentiometry.

4.4 Conclusion

In summary, we have successfully fabricated the PANI/NPG structure for high-performance supercapacitor. NPG was made from Au-Mg alloy with etching in diluted acetic acid, which was environmentally-friendly and very simple. PANI was fabricated by electro-polymerization of aniline on NPG. Using chrono-potentiometry and perchloric acid, we made compact and uniform PANI. TEM showed that PANI layer was uniformly deposited on the whole ligaments of NPG with the thickness of around 10 nm. Prepared PANI/NPG supercapacitors showed great performance such as high capacitance of 6.54 mF/cm^2, maximum energy density of 9.11 mWh/cm^2 at power density of 1.56 W/cm^2, and a long lifespan. Combining highly conductive and large surface area of NPG which works as the remarkable current collector and compact and uniform PANI on it, the synergistic effect yielded a great supercapacitor with long term stability.

4.5 Calculations

1. Capacitance

a. Cyclic voltammetry

(1) Areal capacitance

$$C(F/cm^2) = \int \frac{IdV}{2Sv\Delta V}$$

Where, $\int IdV$ is area of CV curve

S is area of electrode surface (cm^2)

v is scan rate (V/s)

ΔV is voltage window

$$C(F/cm^2) = \frac{0.157\ mA \cdot V}{2 \times 1.2\ cm^2 \times 0.01\ V/s\ \times (0.8\ V - (-0.2\ V))} = 6.54\ mF/cm^2$$

(2) Volumetric capacitance

$$C(F/cm^3) = \int \frac{IdV}{2vv\Delta V}$$

Where, $\int IdV$ is area of CV curve

v is volume of electrode (cm^3)

v is scan rate (V/s)

ΔV is voltage window

$$C(F/cm^2) = \frac{0.157\ mA \cdot V}{2 \times 1.2\ cm^2 \times 200\ nm\ \times 0.01\ V/s\ \times (0.8\ V - (-0.2\ V))} = 327\ F/cm^3$$

b. Galvanostatic charge-discharge

(1) Areal capacitance

$$C(F/cm^2) = \frac{I\Delta t}{S\Delta V}$$

Where, I is current density

Δt is discharge time

S is area of electrode surface

ΔV is voltage window

$$C(F/cm^2) = \frac{0.3\ mA\ \times 21\ s}{1.2\ cm^2 \times 1\ V} = 5.25\ mF/cm^2$$

(2) Volumetric capacitance

$$C(F/cm^3) = \frac{I\Delta t}{v\Delta V}$$

Where, I is current density

Δt is discharge time

v is volume of electrode surface

ΔV is voltage window

$$C(F/cm^3) = \frac{0.3\ mA\ \times 21\ s}{1.2\ cm^2 \times 200\ nm\ \times 1\ V} = 262.5\ mF/cm^3$$

2. Energy density

$$E = \frac{1}{2}C_{tw}V^2 = \frac{1}{8}C_{th}V^2$$

Where, C_{tw} is capacitance of two electrode system

C_{th} is capacitance of three electrode system

V is voltage window

$$E = \frac{1}{8} \times 262.5\ F/cm^3 \times (1V)^2 = 32.812\ \ Ws/cm^3 = \ \ 9.11\ mWh/cm^3$$

3. Power density

$$P = \frac{E}{\Delta t}$$

Where, E is energy density

Δt is discharge time

$$P = \frac{E}{\Delta t} = 9.11 mWh/cm^3 \div 21\ s = 1.56\ W/cm^3$$

4.6 References

1. Guo, X.; Han, J.; Liu, P.; Chen, L.; Ito, Y.; Jian, Z.; Jin, T.; Hirata, A.; Li, F.; Fujita, T.; Asao, N.; Zhou, H.; Chen, M., Hierarchical nanoporosity enhanced reversible capacity of bicontinuous nanoporous metal based Li-O2 battery. *Scientific Reports* **2016,** *6* (1), 33466.
2. Ghasem Hosseini, M.; Shahryari, E., A Novel High-Performance Supercapacitor based on Chitosan/Graphene Oxide-MWCNT/Polyaniline. *Journal of Colloid and Interface Science* **2017,** *496*, 371-381.
3. Chen, T.; Tang, Y.; Qiao, Y.; Liu, Z.; Guo, W.; Song, J.; Mu, S.; Yu, S.; Zhao, Y.; Gao, F., All-solid-state high performance asymmetric supercapacitors based on novel MnS nanocrystal and activated carbon materials. *Scientific Reports* **2016,** *6* (1), 23289.
4. Kalambate, P. K.; Dar, R. A.; Karna, S. P.; Srivastava, A. K., High performance supercapacitor based on graphene-silver nanoparticles-polypyrrole nanocomposite coated on glassy carbon electrode. *Journal of Power Sources* **2015,** *276*, 262-270.
5. Guo, H.; Yin, H.; Yan, X.; Shi, S.; Yu, Q.; Cao, Z.; Li, J., Pt-Bi decorated nanoporous gold for high performance direct glucose fuel cell. *Scientific Reports* **2016,** *6* (1), 39162.
6. Barsuk, D.; Zadick, A.; Chatenet, M.; Georgarakis, K.; Panagiotopoulos, N. T.; Champion, Y.; Moreira Jorge, A., Nanoporous silver for electrocatalysis application in alkaline fuel cells. *Materials & Design* **2016,** *111*, 528-536.
7. Simon, P.; Gogotsi, Y.; Dunn, B., Where Do Batteries End and Supercapacitors Begin? **2014,** *343* (6176), 1210-1211.
8. Zhu, S.; Li, L.; Liu, J.; Wang, H.; Wang, T.; Zhang, Y.; Zhang, L.; Ruoff, R. S.; Dong, F., Structural Directed Growth of Ultrathin Parallel Birnessite on β-MnO2 for High-Performance Asymmetric Supercapacitors. *ACS Nano* **2018,** *12* (2), 1033-1042.
9. Zhu, S.; Shan, Q.; Dong, F.; Zhang, Y.; Zhang, L., Fabrication of mesoporous gold networks@MnO2 for high-performance supercapacitors. *Gold Bulletin* **2017,** *50* (1), 61-68.
10. Zhu, S. J.; Jia, J. Q.; Wang, T.; Zhao, D.; Yang, J.; Dong, F.; Shang, Z. G.; Zhang, Y. X., Rational design of octahedron and nanowire CeO2@MnO2 core–shell heterostructures with outstanding rate capability for asymmetric supercapacitors. *Chemical Communications* **2015,** *51* (80), 14840-14843.
11. Algharaibeh, Z.; Liu, X.; Pickup, P. G., An asymmetric anthraquinone-modified carbon/ruthenium oxide supercapacitor. *Journal of Power Sources* **2009,** *187* (2), 640-643.
12. Lang, X.; Hirata, A.; Fujita, T.; Chen, M., Nanoporous metal/oxide hybrid electrodes for electrochemical supercapacitors. *Nature Nanotechnology* **2011,** *6* (4), 232-236.

13. Tang, Y.; Chen, T.; Yu, S., Morphology controlled synthesis of monodispersed manganese sulfide nanocrystals and their primary application in supercapacitors with high performances. *Chemical Communications* **2015,** *51* (43), 9018-9021.
14. Song, X.; Tan, L.; Wang, X.; Zhu, L.; Yi, X.; Dong, Q., Synthesis of CoS@rGO composites with excellent electrochemical performance for supercapacitors. *Journal of Electroanalytical Chemistry* **2017,** *794*, 132-138.
15. Diggikar, R. S.; Ambekar, J. D.; Kulkarni, M. V.; Kale, B. B., Nanocrystalline silver vanadium sulfide (SVS) anchored polyaniline (PANI): new nanocomposite system for supercapacitor. *New Journal of Chemistry* **2013,** *37* (10), 3236-3243.
16. Wu, G.; Tan, P.; Wang, D.; Li, Z.; Peng, L.; Hu, Y.; Wang, C.; Zhu, W.; Chen, S.; Chen, W., High-performance Supercapacitors Based on Electrochemical-induced Vertical-aligned Carbon Nanotubes and Polyaniline Nanocomposite Electrodes. *Scientific Reports* **2017,** *7* (1), 43676.
17. Zhao, Y.-Q.; Zhao, D.-D.; Tang, P.-Y.; Wang, Y.-M.; Xu, C.-L.; Li, H.-L., MnO2/graphene/nickel foam composite as high performance supercapacitor electrode via a facile electrochemical deposition strategy. *Materials Letters* **2012,** *76*, 127-130.
18. Lang, X.; Zhang, L.; Fujita, T.; Ding, Y.; Chen, M., Three-dimensional bicontinuous nanoporous Au/polyaniline hybrid films for high-performance electrochemical supercapacitors. *Journal of Power Sources* **2012,** *197*, 325-329.
19. Hou, Y.; Chen, L.; Zhang, L.; Kang, J.; Fujita, T.; Jiang, J.; Chen, M., Ultrahigh capacitance of nanoporous metal enhanced conductive polymer pseudocapacitors. *Journal of Power Sources* **2013,** *225*, 304-310.
20. Zhang, C.; Xiao, J.; Qian, L.; Yuan, S.; Wang, S.; Lei, P., Planar integration of flexible micro-supercapacitors with ultrafast charge and discharge based on interdigital nanoporous gold electrodes on a chip. *Journal of Materials Chemistry A* **2016,** *4* (24), 9502-9510.
21. Stejskal, J.; Sapurina, I.; Trchová, M., Polyaniline nanostructures and the role of aniline oligomers in their formation. *Progress in Polymer Science* **2010,** *35* (12), 1420-1481.
22. Sari, B.; Talu, M.; Yildirim, F., Electrochemical Polymerization of Aniline at Low Supporting-Electrolyte Concentrations and Characterization of Obtained Films. *Russian Journal of Electrochemistry* **2002,** *38* (7), 707-713.
23. Guan, H.; Fan, L.-Z.; Zhang, H.; Qu, X., Polyaniline nanofibers obtained by interfacial polymerization for high-rate supercapacitors. *Electrochimica Acta* **2010,** *56* (2), 964-968.
24. Kuang, H.; Cao, Q.; Wang, X.; Jing, B.; Wang, Q.; Zhou, L., Influence of the reaction temperature on polyaniline morphology and evaluation of their performance as supercapacitor electrode. **2013,** *130* (5), 3753-3758.
25. Wittstock, A.; Biener, J.; Bäumer, M., Chapter 1 Introduction to Nanoporous Gold. In

Nanoporous Gold: From an Ancient Technology to a High-Tech Material, The Royal Society of Chemistry: 2012; pp 1-10.

26. Kim, S. H. J. C. A. o. N.-G. C., Nanoporous gold films as catalyst. **2016**, 1.
27. Kim, S. H., Nanoporous gold: Preparation and applications to catalysis and sensors. *Current Applied Physics* **2018,** *18* (7), 810-818.
28. Li, G. G.; Lin, Y.; Wang, H., Residual Silver Remarkably Enhances Electrocatalytic Activity and Durability of Dealloyed Gold Nanosponge Particles. *Nano Letters* **2016,** *16* (11), 7248-7253.
29. Qadir, K.; Quynh, B. T. P.; Lee, H.; Moon, S. Y.; Kim, S. H.; Park, J. Y., Tailoring metal–oxide interfaces of inverse catalysts of TiO2/nanoporous-Au under hydrogen oxidation. *Chemical Communications* **2015,** *51* (47), 9620-9623.
30. Wang, K.; Stenner, C.; Weissmüller, J., A nanoporous gold-polypyrrole hybrid nanomaterial for actuation. *Sensors and Actuators B: Chemical* **2017,** *248*, 622-629.
31. Lee, K.-U.; Tran, T. H.; Kim, S. H.; Shin, H.-J., Fabrication of nanoporous gold thin films on glass substrates for amperometric sensing of aniline. *Journal of Alloys and Compounds* **2017,** *713*, 132-137.
32. Quynh, B. T. P.; Byun, J. Y.; Kim, S. H., Non-enzymatic amperometric detection of phenol and catechol using nanoporous gold. *Sensors and Actuators B: Chemical* **2015,** *221*, 191-200.
33. Tran, H. T.; Byun, J. Y.; Kim, S. H., Nanoporous metallic thin films prepared by dry processes. *Journal of Alloys and Compounds* **2018,** *764*, 371-378.
34. Quynh, B. T. P.; Byun, J. Y.; Kim, S. H., Electrochemical Behavior of Aromatic Compounds on Nanoporous Gold Electrode. *Journal of The Electrochemical Society* **2018,** *165* (10), B414-B421.
35. Chen, L. Y.; Kang, J. L.; Hou, Y.; Liu, P.; Fujita, T.; Hirata, A.; Chen, M. W., High-energy-density nonaqueous MnO2@nanoporous gold based supercapacitors. *Journal of Materials Chemistry A* **2013,** *1* (32), 9202-9207.
36. Wittstock, A.; Zielasek, V.; Biener, J.; Friend, C. M.; Bäumer, M., Nanoporous Gold Catalysts for Selective Gas-Phase Oxidative Coupling of Methanol at Low Temperature. **2010,** *327* (5963), 319-322.
37. Quynh, B. T. P.; Byun, J. Y.; Kim, S. H., Nanoporous gold for amperometric detection of amino-containing compounds. *Sensors and Actuators B: Chemical* **2014,** *193*, 1-9.
38. Stoller, M. D.; Ruoff, R. S., Best practice methods for determining an electrode material's performance for ultracapacitors. *Energy & Environmental Science* **2010,** *3* (9), 1294-1301.
39. Zhang, S.; Pan, N., Supercapacitors Performance Evaluation. **2015,** *5* (6), 1401401.
40. Wang, L.; Briot, N. J.; Swartzentruber, P. D.; Balk, T. J., Magnesium Alloy Precursor

Thin Films for Efficient, Practical Fabrication of Nanoporous Metals. *Metallurgical and Materials Transactions A* **2014,** *45* (1), 1-5.

41. Lee, K.-U.; Byun, J. Y.; Shin, H.-J.; Kim, S. H., A high-performance supercapacitor based on polyaniline-nanoporous gold. *Journal of Alloys and Compounds* **2019,** *779*, 74-80.
42. Li, H.; Wang, J.; Chu, Q.; Wang, Z.; Zhang, F.; Wang, S., Theoretical and experimental specific capacitance of polyaniline in sulfuric acid. *Journal of Power Sources* **2009,** *190* (2), 578-586.
43. Chen, G. Z., Understanding supercapacitors based on nano-hybrid materials with interfacial conjugation. *Progress in Natural Science: Materials International* **2013,** *23* (3), 245-255.
44. Mohd, Y.; Ibrahim, R.; Zainal, M. F. In *Electrodeposition and characterization of Polyaniline films*, 2012 IEEE Symposium on Humanities, Science and Engineering Research, 24-27 June 2012; 2012; pp 1301-1306.
45. Gao, W.; Singh, N.; Song, L.; Liu, Z.; Reddy, A. L. M.; Ci, L.; Vajtai, R.; Zhang, Q.; Wei, B.; Ajayan, P. M., Direct laser writing of micro-supercapacitors on hydrated graphite oxide films. *Nature Nanotechnology* **2011,** *6* (8), 496-500.
46. Moon, Y. S.; Kim, D.; Lee, G.; Hong, S. Y.; Kim, K. K.; Park, S. M.; Ha, J. S., Fabrication of flexible micro-supercapacitor array with patterned graphene foam/MWNT-COOH/MnOx electrodes and its application. *Carbon* **2015,** *81*, 29-37.
47. Nunziante, P.; Pistoia, G., Factors affecting the growth of thick polyaniline films by the cyclic voltammetry technique. *Electrochimica Acta* **1989,** *34* (2), 223-228.

CHAPTER 5
NANOPOROS GOLD PALLADIUM FOR FUEL CELL

5.1 Introduction

Nanoporous gold (NPG) is known as a three dimensional continuous material which also exhibits corrosive property. NPG has drawn significant attention in many research fields, including catalysis, sensors, actuators, and energy systems, among others because of its high conductivity, large surface area, abundance of low-coordinated atoms, and excellent stability. [1-3]

To enhance the catalytic activity and/or functionalize an NPG structure, other materials are commonly deposited or coated onto NPG ligaments. The catalytic activity of the bimetal alloy catalyst is often to be several times higher than that of the pure metal or metal-oxide catalyst's counterpart.[4, 5] Pt,[6] Cu,[7] and several metal and oxide materials[8, 9] have been mixed into NPG. Particularly, Pd is a very promising material due to its high catalytic activity and it is comparable to that of Pt, though with a lower price and higher abundance.[10] The Pd-NPG alloy has shown excellent catalytic activity in a number of reactions. Kiani and coworkers reported oxygen reduction reaction of Pd coated NPG by underpotential deposition.[11] Additionally, Ke and coworkers manufactured a Pd-decorated NPG electrode for enhancing the catalytic activity toward H_2O_2 reduction reaction.[12] However, the synthesis processes and the required sequential deposition are very sophisticated and quite cumbersome. The tuning the composition and porosity of the resulting NPG structures are also very difficult.

The ternary systems have been introduced for the fabrication of binary nanoporous gold-palladium (NP-AuPd) structures, with Al, Zn, and Ni which are used as sacrificial elements during the preparation of NP-AuPd to resolve this drawback.[13-15] Most of these works tried with electrochemical alloying/dealloying through using NaOH or H_2SO_4. However, using these methods, it is very difficult to control the porosities of the nanoporous structures and these procedures are not suitable for the fabrication of multiple samples. In contrary, the ternary alloy thin film deposition by magnetron sputtering on a substrate provides a possible solution for the preparation of binary porous structures with controlled compositions and porosities. However, as ternary alloy thin films made by magnetron sputtering can easily peel off during etching with typical basic etchants and strongly acidic, discovering suitable etchants and dealloying conditions is a very essential objective.

The NPG thin films from Au-Mg alloys with dilute acetic acid is recently reported by us, which is a very moderate etching process.[16] In this study, we applied this gentle method to 100-nm-thick Au-Pd-Mg thin films and the NP-AuPd thin films were successfully manufactured with controlled compositions and porosities. In addition, Mg and acetic acid are very attractive because they are economical and environmentally friendly. Furthermore, they are readily integrated into electrochemical systems because the NP-AuPd structures are prepared on conducting adhesive substrates, while nanoporous metallic structures fabricated from alloys first should be adherent on the substrates to integrate into an electrochemical system.

Herein, NP-AuPd thin films were used to the electrochemical ethanol oxidation reaction (EOR) in alkaline media of a direct ethanol fuel cell (DEFC). The schematic diagram of fuel cell is shown in figure 5.1. To date, nanoparticle-based catalysts have generally been fixed on conducting substrates e.g. glassy carbon electrode in order to use it for DEFC applications.[17] However, nanoparticle-based catalysts suffer from leaching and aggregation during the chemical reactions.[18, 19] Moreover, these synthesis processes are quite complicated and manufacture steps are lengthy. On the other hand, NP-AuPd thin films are not only manufactured in a short-step method excluding leaching/aggregation concerns, but are also ready for integration and exhibit durable high catalytic activities.

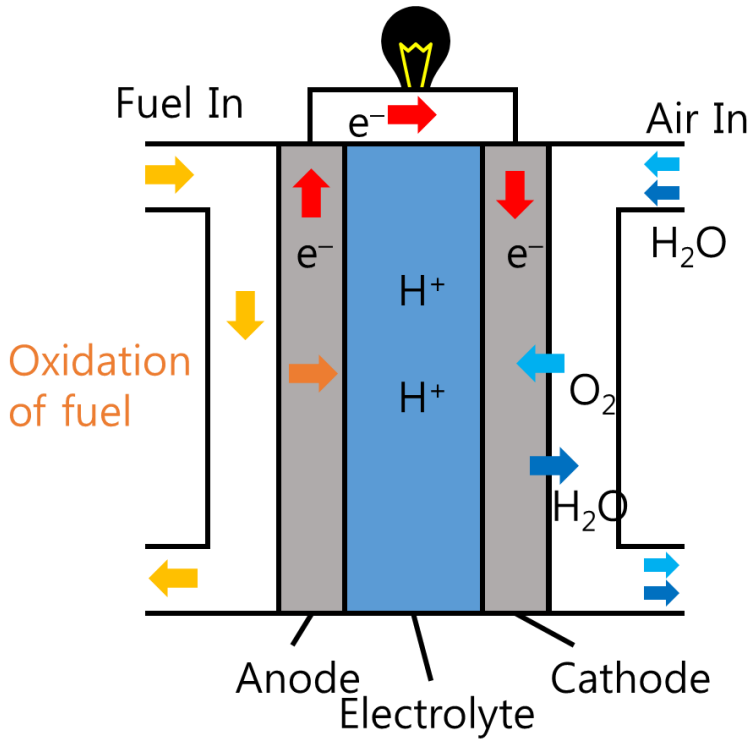

Figure 5.1. Schematic diagram of fuel cell

5.2 Experimental Section

Fabricating NP-AuPd

We sputter-deposited Ti films (5 nm) and Au films (70 nm) on 1 × 2 cm silicon substrates as adhesion and protection layers, respectively. Au (5 W), Pd (8 W), and Mg (150 W) were then co-deposited as alloy layers (100 nm). We controlled the composition of the alloy by regulating the sputtering power of each element. The base pressure of sputtering system was set to 2×10^{-6} Torr. After preparing the ternary alloy films, they were immersed in acetic acid (5 wt %) for 30 min to dealloy the Mg from the films. The overall fabrication process is shown in figure 5.2.

Characterization

SEM and TEM were used to examine the morphologies and structures of the samples in this study, and AES (PHI 700, ULVAC–PHI, Japan) was used to investigate the compositions of the alloys and NP-AuPd films. The ternary-alloy and NP-AuPd films subjected to XRD, and XPS data were acquired for determining the chemical states of the NP-AuPd films (PHI 5000 VersaProbe, ULVAC–PHI, Japan).

Electrochemical methods

Electrochemical experiments were conducted at room temperature using a conventional three electrode system (Versastat 3, Princeton Applied Research). NP-AuPd film, platinum wire, and Ag/AgCl (3 M NaCl) were used as the working, counter, and reference electrodes, respectively. The electrolyte was 1 M KOH containing 1 M ethanol solution. A 0.5-cm^2 area of the working electrode was immersed in the electrolyte, and CV was conducted from -0.6 V to 0.7 V at a scan rate of 50 mV s^{-1}.

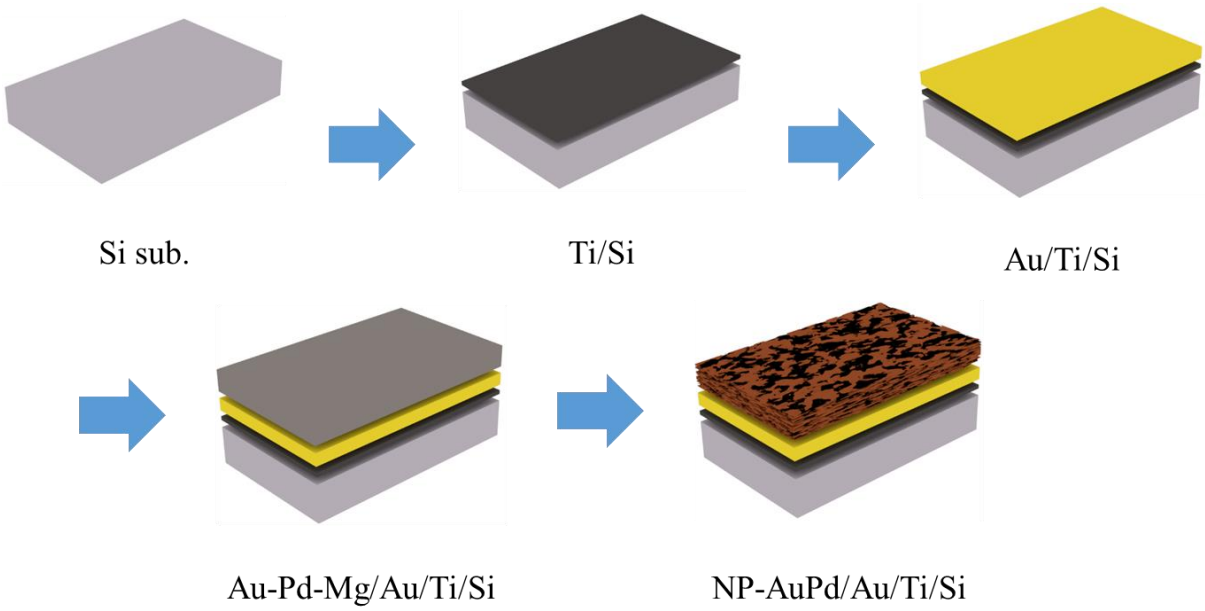

Figure 5.2. Schematic of fabrication process of our sample

5.3 Results and discussions

Nanoporous structures were successfully formed using Mg, which is a remarkable sacrificial element for fabricating nanoporous structures.[16] Mg is easily dissolved by dilute acetic acid, which is a very safe and environmentally friendly reagent. Figure 5.3 shows the microstructures and elements distribution of NP-AuPd; panel (a) shows a top-view scanning electron microscopy (SEM) image of the NP-AuPd sample; its pores and ligaments are around 20–30 nm in size. In addition, the ligaments contain very tiny holes that contribute to its large surface area and fast mass transfer. The fine structure of our NP-AuPd was further investigated by transmission electron microscopy (TEM). Figure 5.3 (b) and (c) show a cross-sectional TEM image of NP-AuPd and the corresponding energy-dispersive X-ray spectroscopy (EDS) map, respectively. The Au-protection and NP-AuPd layers are around 70-nm and 100-nm thick, respectively, with the surface as well as the entire alloy layer showing highly porous structures. The TEM EDS image in figure 5.3 (c) reveals that both Au and Pd are uniformly distributed in the entire NP-AuPd layer; Mg was mostly removed and not detected by EDS. The Auger depth profiles of the ternary alloy film (before etching) and the NP-AuPd thin film (after etching) are shown in figure 5.3 (d) and (e), respectively. Au, Pd, and Mg are observed to be uniformly sputter-deposited on the substrate. After etching, Auger electron spectroscopy (AES) revealed that the Mg was mostly removed, from a level of about 55% before etching to less than 20% following etching. The Au:Pd:Mg composition ratio in the ternary alloy and the Au:Pd ratio in NP-AuPd are around 20:25:55 and 40:60, respectively. We employed X-ray photoelectron spectroscopy (XPS) to investigate the chemical states of our NP-AuPd, with pure Au and pure Pd films used as references. Figure 5.4 (a) and (b) show the Au 4f and Pd 3d spectra of NP-AuPd, which reveal that the Au 4f binding energy is slightly shifted to a lower value in the spectrum of NP-AuPd compared to that of pure gold (figure 5.4 (a)). This shift is mainly ascribable to the fact that Au is highly electronegative; consequently, the Au in the film is negatively charged, which decreases the binding energy.[20] On the other hand, the Pd 3d peaks of NP-AuPd coincide with those of pure Pd. We speculate that the amount of Pd is higher than that of Au in the film; hence Pd is less oxidized.

Figure 5.5 (a) shows an X-ray diffraction (XRD) pattern for NP-AuPd. We calculated the lattice spacing of the (111) facet of NP-AuPd to be 2.29 Å, which lies between that of Pd (2.25 Å) and Au (2.36 Å) and confirms that Au and Pd are fully alloyed in the NP-AuPd sample. We acquired selected area diffraction (SAED) data and calculated the lattice spacing to be 2.3 Å by fast Fourier transform (FFT), which is consistent with the XRD result (figure 5.5 (b), (c)).

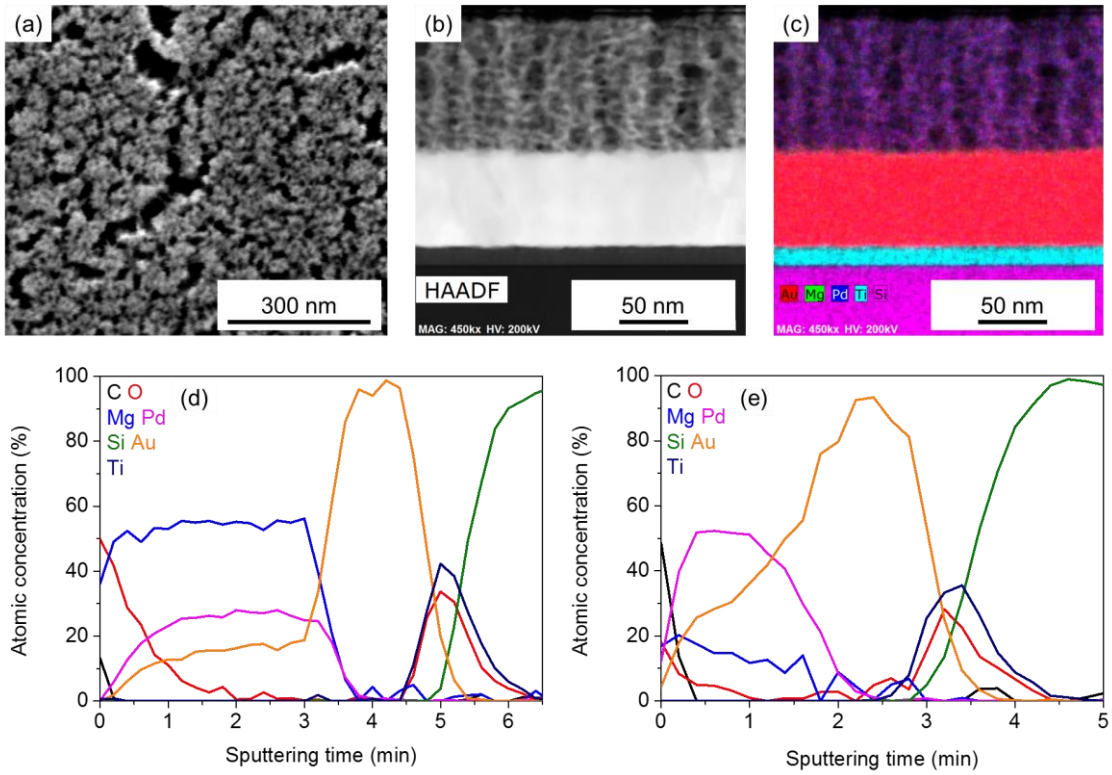

Figure 5.3. Microstructures and elements distribution of NP-AuPd (a) SEM image of top view, (b) cross-sectional TEM image, and (c) corresponding TEM EDS map. (d) Auger electron spectroscopy results of ternary alloy and (e) NP-AuPd[21]

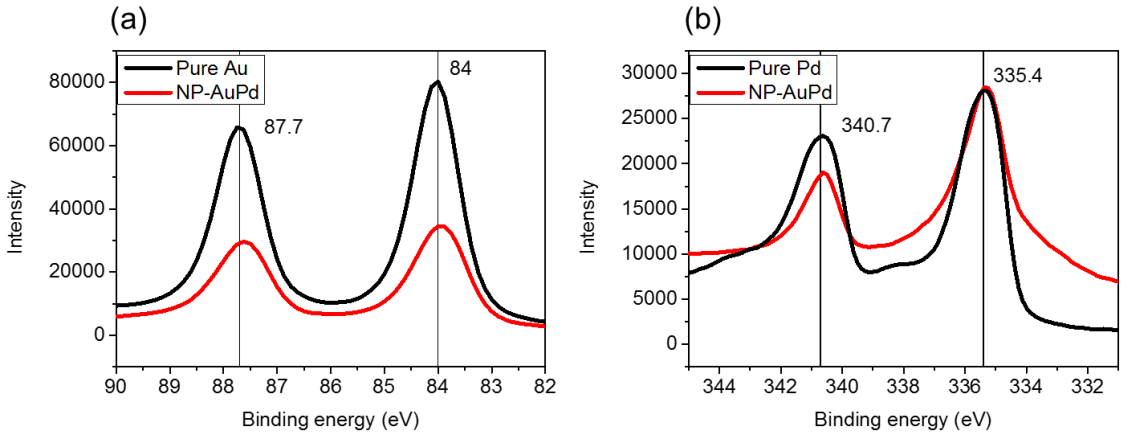

Figure 5.4. XPS results of (a) Au 4f and (b) Pd 3d.[21]

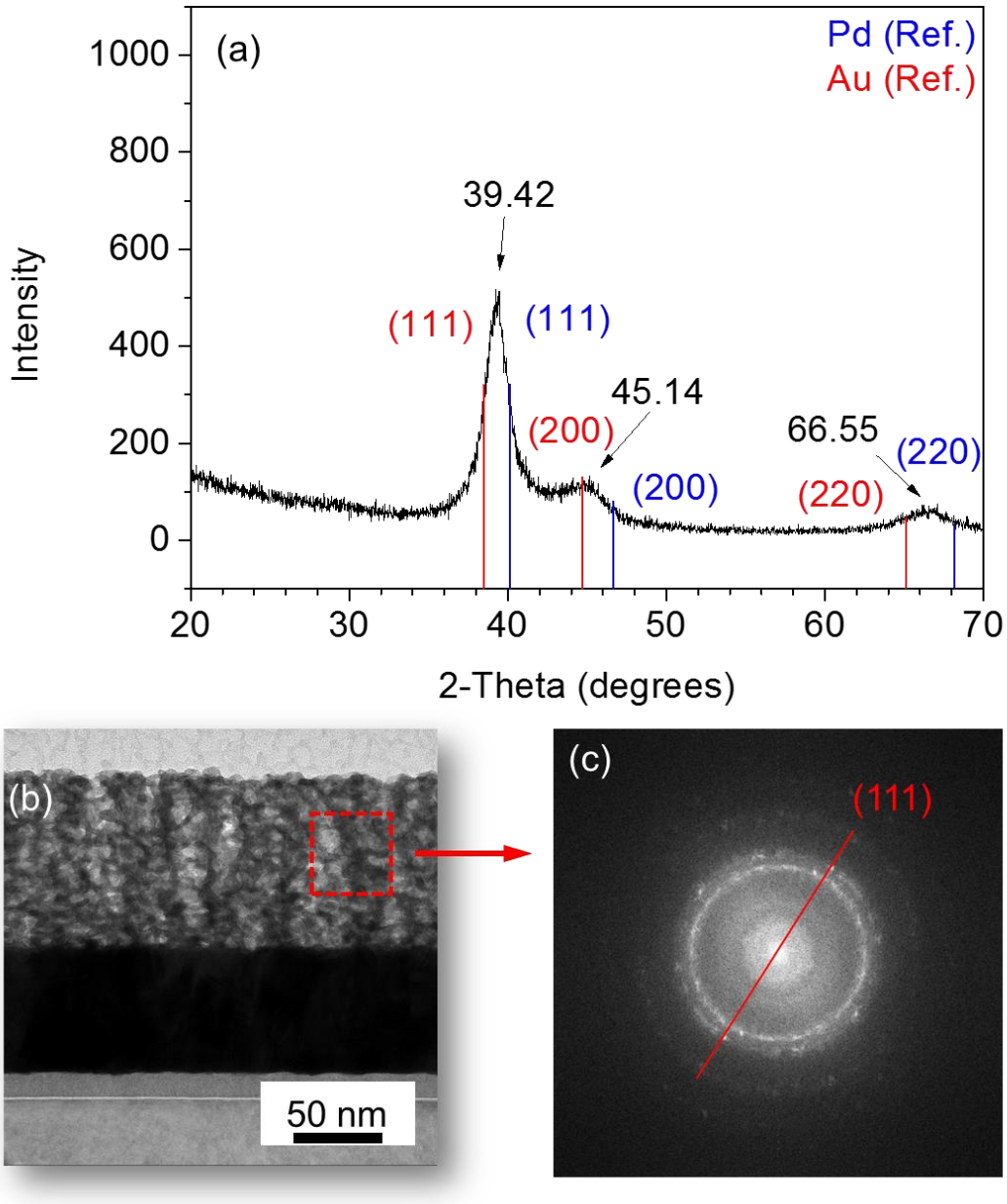

Figure 5.5. Crystal analysis of NP-AuPd. (a) XRD profiles of NP-AuPd. (b) Cross-sectional TEM image of NP-AuPd. (c) TEM selected area diffraction (SAED) results of NP-AuPd. The red square is the selected area.[21]

The catalytic activity of NP-AuPd toward the electrochemical oxidation of ethanol in alkaline media was evaluated by cyclic voltammetry (CV) in 1 M KOH containing 1 M ethanol solution at a scan rate of 50 mV s^{-1}, the results of which are shown in figure 5.6 (a). Our NP-AuPd electrode exhibited a high peak current density of 212.2 mA cm^{-2} at 0.31 V (vs. Ag/AgCl). We also tested NPG and nanoporous Pd (NP-Pd) electrodes as references, which verified that NP-AuPd is highly catalytically active. Our NP-AuPd also showed very high current values compared to those reported for other anodes used in DEFC applications (Table 1). The peak current ratio (I_f/I_b) is a measure of the resistance of a catalyst to poisoning by carbonaceous intermediates, where I_f and I_b are the peak currents of the forward and backward scans, respectively.[18, 22] The I_f/I_b value for NP-AuPd was determined to be 2.16, which is quite high compared to previously reported values that are generally under 2.[18, 22, 23] To explore its stability, NP-AuPd was subjected to CV for 100 cycles, which took over 5000 s to complete. The relationship between peak current and cycle number is shown in figure 5.6 (b), which reveals that the peak current decreases slightly with increasing cycle number. The peak current at the 100th cycle was around 70% that of the first cycle. This stability is excellent compared to those of other materials reported in the literature.[18, 23]

We can easily tune the composition of the alloy by controlling the sputtering method. Consequently, we evaluated how the Au and Pd composition of the NP-AuPd affects catalytic activity. By simply regulating the sputtering power of each target, we prepared a Au-rich sample (A sample) and a Pd-rich sample (P sample); these samples were subjected to SEM and AES with the results for the A and P samples shown in figure 5.7 and 5.8, respectively. The Au:Pd ratio in the A sample was 70:30, while it was 25:75 in the P sample. We compared the catalytic activities of the A and P samples with that of the NP-AuPd sample described earlier (D sample, Au:Pd ratio = 40:60); the CVs of the three samples are shown in figure 5.6 (c). The D sample exhibited a much higher current density than the A or P sample. The peak position in the CV trace of the D sample is rightward shifted, which implies that Au and Pd oxidation is delayed, enabling reactions at high potential. The optimum ratio of Au to Pd (i.e., the ratio that provides the highest catalytic activity) in the AuPd alloy is still a matter of debate.[10, 20, 24-26] Our NP-AuPd showed the highest catalytic activity at a ratio of 40:60, which is close to 1:1.

We also controlled the porosity of our NP-AuPd by controlling the amount of Mg used. We explored Mg-sputtering powers of 50 W, 100 W, and 150 W at a fixed Au:Pd ratio of 40:60 (D sample). The SEM image of each sample and its cyclic voltammogram are shown in figure 5.9 and 5.10, which reveal that porosity increases with increasing Mg-sputtering power (amount of Mg). In particular, the D sample prepared with 150 W of Mg exhibited both large pores as well as very tiny holes in its ligaments; these tiny holes are not observed in the samples prepared at 50 W or 100 W. We believe that these holes are a major reason for the dramatic increase in peak current.

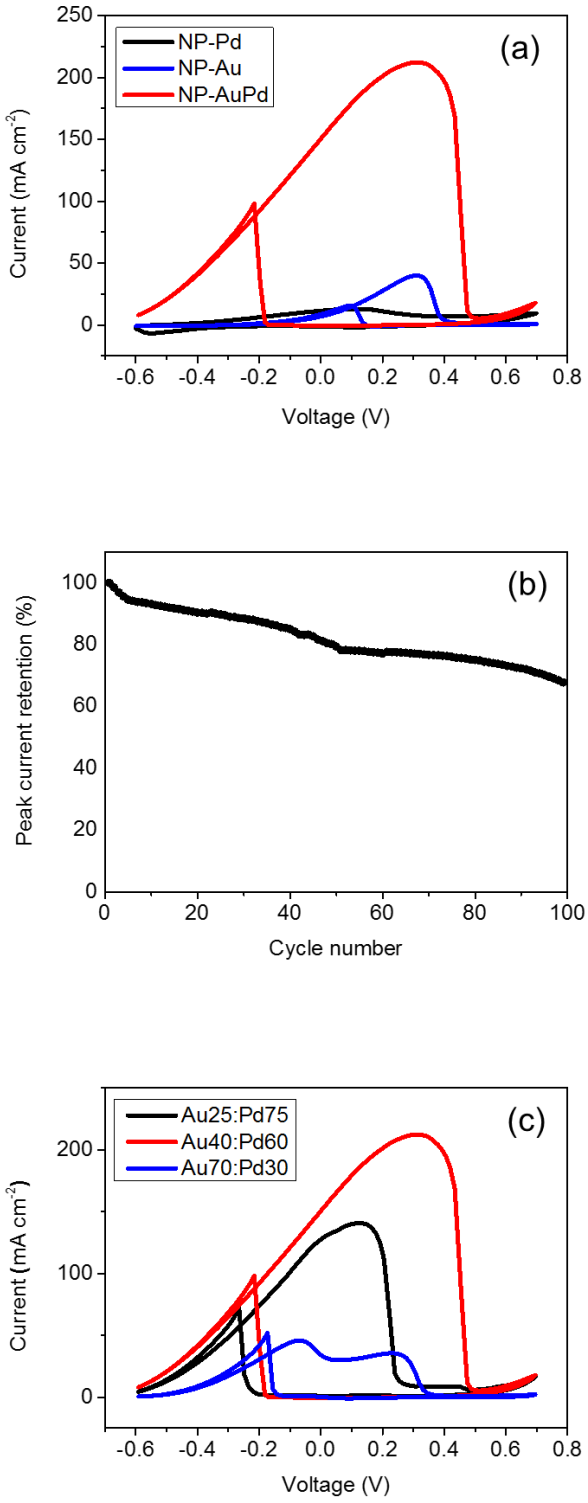

Figure 5.6. Electrochemical results of NP-AuPd. (a) Cyclic voltammogram of NP-AuPd, NP-Au, and NP-Pd electrodes. (b) Peak current retention to 100 cycles during successive cyclic voltammetry. (c) Cyclic voltammogram of NP-AuPd with different compositions.[21]

Table 1. Summarizing recent studies of alkaline DEFC data.[21]

Materials	Electrolyte (1 M)	Scan rate ($mV\ s^{-1}$)	Peak current ($mA\ cm^{-2}$)	Reference
AuPd/C	KOH + EtOH	50	84.16	[10]
Pd-Ni alloy	KOH + EtOH	50	117.3	[27]
Pd-Co-RGO/GC	KOH + EtOH	50	64.2	[28]
PdP_2/RGO	(0.5 M) KOH + (0.5 M) EtOH	50	51.4	[22]
Pd_3Au	KOH + EtOH	50	167	[20]
PdCuPb/C	KOH + EtOH	50	105.3	[29]
Pd nanowire	KOH + EtOH	50	70	[30]
NP-AuPd	KOH + EtOH	50	212.2	Our work

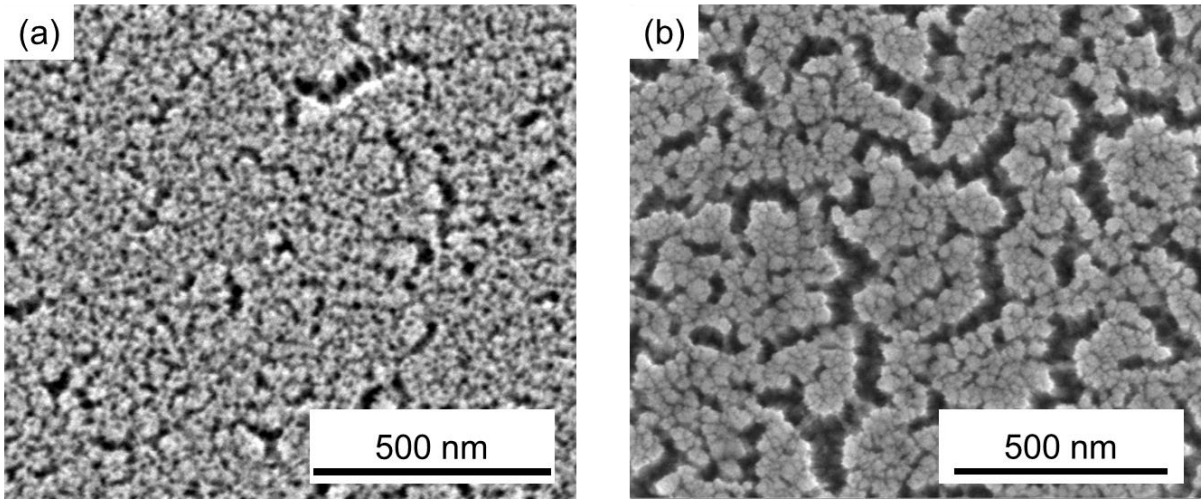

Figure 5.7. SEM images of Au rich samples (a), and Pd rich sample (b).[21]

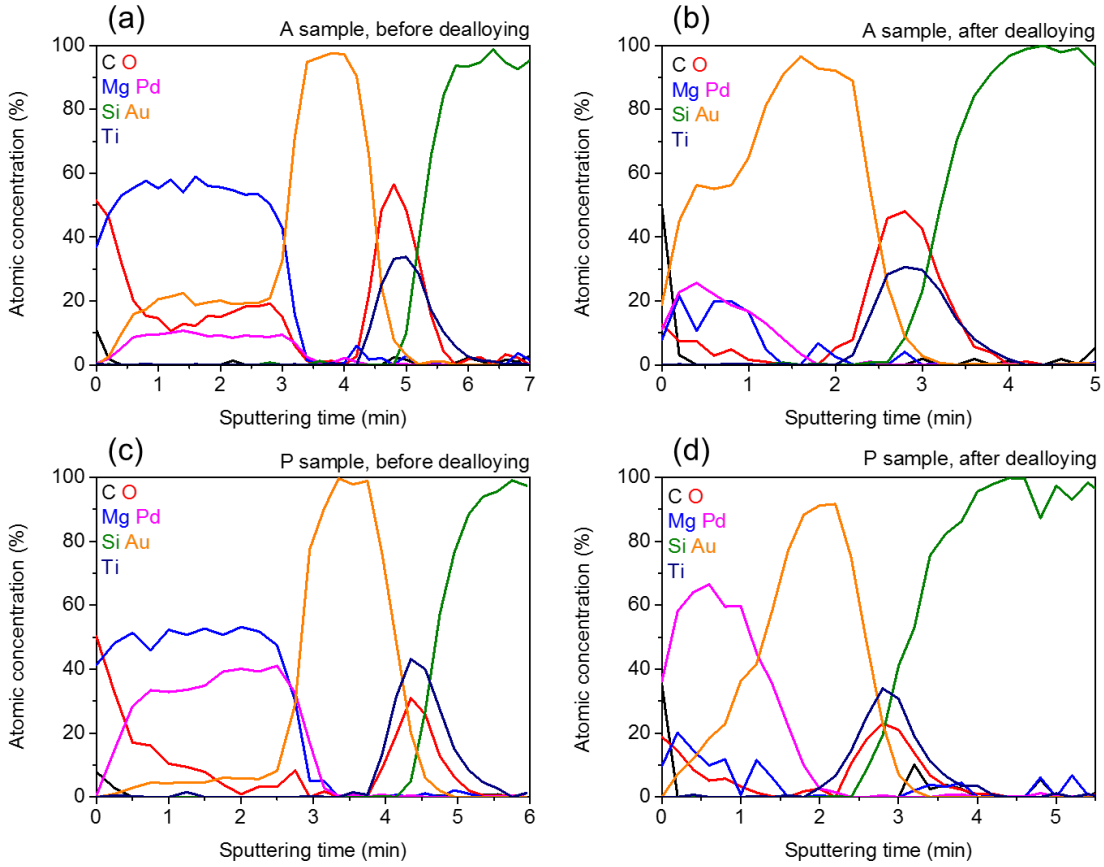

Figure 5.8. Auger depth profiles of before and after dealloying of Au rich samples and Pd rich samples.[21]

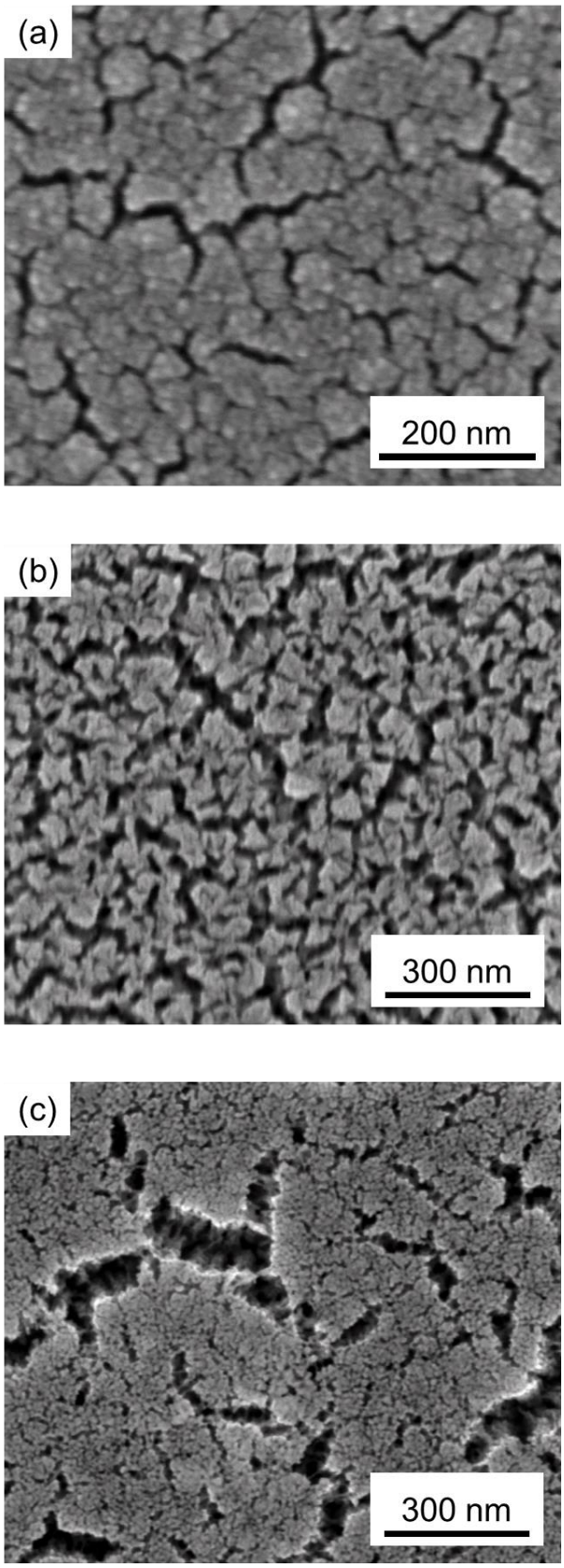

Figure 5.9. SEM images of samples with various porosity.
(a) Mg 50 W, (b) Mg 100 W, (c) Mg 150 W[21]

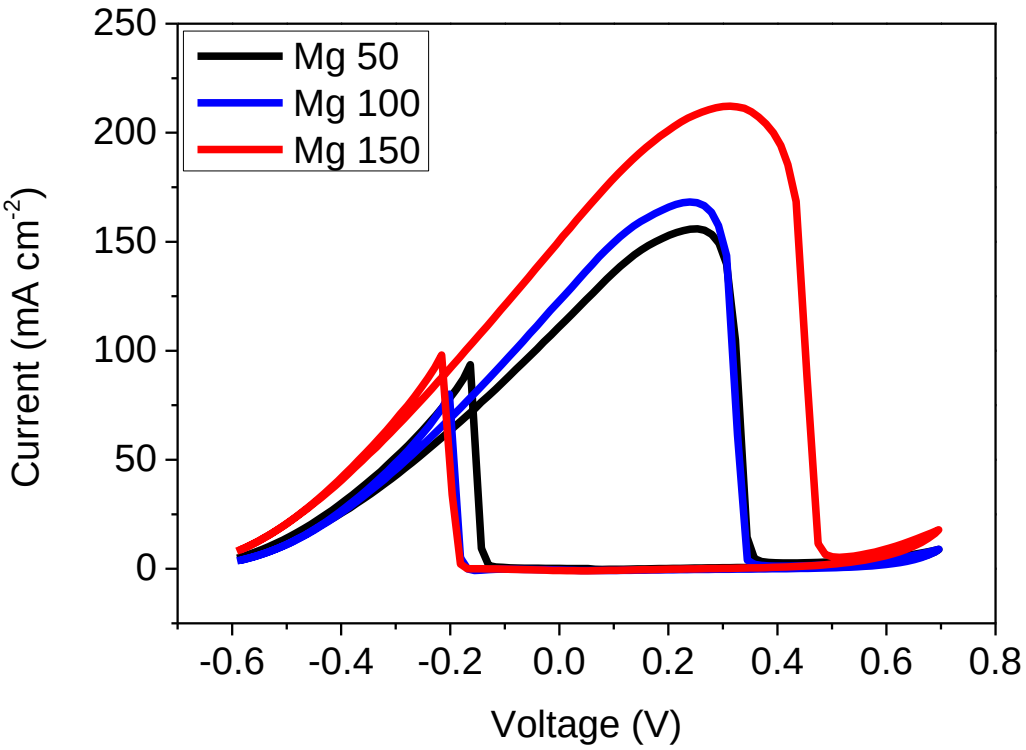

Figure 5.10. Cyclic voltammogram of NP-AuPd with various porosity in 1 M KOH containing 1 M ethanol[21]

The electro-oxidation mechanism of ethanol on Pd in an alkaline medium is described by:[31]

$$Pd + OH^- \rightarrow Pd - OH_{ads} + e^- \quad (1)$$

$$Pd + CH_3CH_2OH + 3OH^- \rightarrow Pd - (CH_3CO)_{ads} + 3H_2O + 3e^- \quad (2)$$

$$Pd - (CH_3CO)_{ads} + Pd - OH_{ads} \rightarrow Pd - CH_3COOH + Pd \quad (3)$$

$$Pd - CH_3COOH + OH^- \rightarrow Pd + CH_3COO^- + H_2O \quad (4)$$

The reaction of CH_3CO_{ads} and OH_{ads} to form CH_3COOH is the rate-determining step (Equation (3)) in the overall process. The adsorbed hydroxide ions are very important during the EOR because they remove reaction intermediates that result in surface poisoning. Au on Pd has been reported to improve the opportunity for hydroxide ion adsorption, which promotes the rate-determining step and enhances the entire EOR process.[25]

The remarkable electro-catalytic activity of NP-AuPd toward ethanol oxidation in alkaline media is based on two factors. Firstly, the binary-composed three-dimensional open-porous structure is advantageous because it offers a high surface area with a number of low-coordinated atoms and interfaces between Pd and Au, which act as active sites.[32] Additionally, there is no contact resistance between the active material and the current collector for the one-body nature nanoporous structure, which results in high conductivity; furthermore, the superior stability of the catalyst increases its lifespan.[19] Secondly, Au plays a highly important role in these Au-Pd alloy structures. As described above, Au helps hydroxide ions to adsorb onto the catalyst surface, which promotes the rate-determining step of the EOR in alkaline media; this effect is proposed on the basis of d-band center theory.[25, 26] Because the Au and Pd lattice parameters are different, the alloy lattice is strained, causing the Pd d-band center to shift upwards. Furthermore, the presence of Au in the Pd structure has a stabilizing effect, which delays Pd oxidation and enables reactions to occur at high potential, leading to a high current density.[10, 20] These are the two main factors responsible for the remarkable electro-catalytic activity of NP-AuPd.

5.4 Conclusion

We prepared NP-AuPd thin films by co-sputtering Au, Pd, and Mg, and fabricated nanoporous structures by extracting Mg in dilute acetic acid. The Pd and Au compositions in alloy were controlled by adjusting the sputtering power of each target, and porosity was controlled by adjusting the Mg-sputtering power. We optimized the Au/Pd composition and porosity; the optimum NP-AuPd sample exhibited remarkable electro-catalytic activity toward the electro-oxidation of ethanol in alkaline media. The high surface area and the optimized composition that provides the maximum number of active sites are the main reasons for the observed high catalytic activity. Additionally, NP-AuPd showed impressive stability, and sustained a peak current retention of 70% after 100 cycles of CV. This notable stability is believed to be the result of one-body structures in the Au-Pd binary alloy. Finally, we prepared a high-performance anode material for DEFC applications. We fabricated NP-AuPd from ternary Au-Pd-Mg alloy films with Mg as the sacrificial element; this method could be applicable to designed binary alloy with desired properties.

5.5 References

1. Biener, J.; Wittstock, A.; Zepeda-Ruiz, L. A.; Biener, M. M.; Zielasek, V.; Kramer, D.; Viswanath, R. N.; Weissmüller, J.; Bäumer, M.; Hamza, A. V., Surface-chemistry-driven actuation in nanoporous gold. *Nature Materials* **2009,** *8* (1), 47-51.
2. Lang, X.; Hirata, A.; Fujita, T.; Chen, M., Nanoporous metal/oxide hybrid electrodes for electrochemical supercapacitors. *Nature Nanotechnology* **2011,** *6* (4), 232-236.
3. Quynh, B. T. P.; Byun, J. Y.; Kim, S. H., Non-enzymatic amperometric detection of phenol and catechol using nanoporous gold. *Sensors and Actuators B: Chemical* **2015,** *221*, 191-200.
4. Evangelisti, C.; Schiavi, E.; Aronica, L. A.; Caporusso, A. M.; Vitulli, G.; Bertinetti, L.; Martra, G.; Balerna, A.; Mobilio, S., Bimetallic Gold–Palladium vapour derived catalysts: The role of structural features on their catalytic activity. *Journal of Catalysis* **2012,** *286*, 224-236.
5. Pizzutilo, E.; Freakley, S. J.; Geiger, S.; Baldizzone, C.; Mingers, A.; Hutchings, G. J.; Mayrhofer, K. J. J.; Cherevko, S., Addressing stability challenges of using bimetallic electrocatalysts: the case of gold–palladium nanoalloys. *Catalysis Science & Technology* **2017,** *7* (9), 1848-1856.
6. Guo, H.; Yin, H.; Yan, X.; Shi, S.; Yu, Q.; Cao, Z.; Li, J., Pt-Bi decorated nanoporous gold for high performance direct glucose fuel cell. *Scientific Reports* **2016,** *6* (1), 39162.
7. Guo, M.-m.; Wang, P.-s.; Zhou, C.-h.; Xia, Y.; Huang, W.; Li, Z., An ultrasensitive non-enzymatic amperometric glucose sensor based on a Cu-coated nanoporous gold film involving co-mediating. *Sensors and Actuators B: Chemical* **2014,** *203*, 388-395.
8. Qadir, K.; Quynh, B. T. P.; Lee, H.; Moon, S. Y.; Kim, S. H.; Park, J. Y., Tailoring metal–oxide interfaces of inverse catalysts of TiO2/nanoporous-Au under hydrogen oxidation. *Chemical Communications* **2015,** *51* (47), 9620-9623.
9. Shi, J.; Schaefer, A.; Wichmann, A.; Murshed, M. M.; Gesing, T. M.; Wittstock, A.; Bäumer, M., Nanoporous Gold-Supported Ceria for the Water–Gas Shift Reaction: UHV Inspired Design for Applied Catalysis. *The Journal of Physical Chemistry C* **2014,** *118* (50), 29270-29277.
10. Shen, S.; Guo, Y.; Luo, L.; Li, F.; Li, L.; Wei, G.; Yin, J.; Ke, C.; Zhang, J., Comprehensive Analysis on the Highly Active and Stable PdAu/C Electrocatalyst for Ethanol Oxidation Reaction in Alkaline Media. *The Journal of Physical Chemistry C* **2018,** *122* (3), 1604-1611.
11. Kiani, A.; Fard, E. N., Fabrication of palladium coated nanoporous gold film electrode via underpotential deposition and spontaneous metal replacement: A low palladium loading electrode with electrocatalytic activity. *Electrochimica Acta* **2009,** *54* (28), 7254-7259.
12. Ke, X.; Xu, Y.; Yu, C.; Zhao, J.; Cui, G.; Higgins, D.; Chen, Z.; Li, Q.; Xu, H.; Wu, G., Pd-decorated three-dimensional nanoporous Au/Ni foam composite electrodes for H2O2 reduction. *Journal of Materials Chemistry A* **2014,** *2* (39), 16474-16479.
13. Chen, L. Y.; Chen, N.; Hou, Y.; Wang, Z. C.; Lv, S. H.; Fujita, T.; Jiang, J. H.; Hirata, A.; Chen, M. W., Geometrically Controlled Nanoporous PdAu Bimetallic Catalysts with Tunable Pd/Au

Ratio for Direct Ethanol Fuel Cells. *ACS Catalysis* **2013,** *3* (6), 1220-1230.

14. Wang, X.; Tang, B.; Huang, X.; Ma, Y.; Zhang, Z., High activity of novel nanoporous Pd–Au catalyst for methanol electro-oxidation in alkaline media. *Journal of Alloys and Compounds* **2013,** *565*, 120-126.
15. Chiu, H.-Y.; Liu, Y.-C.; Hsieh, Y.-T.; Sun, I. W., Some Aspects on the One-Pot Fabrication of Nanoporous Pd–Au Surface Films by Electrochemical Alloying/Dealloying of (Pd–Au)–Zn from a Chlorozincate Ionic Liquid. *ACS Omega* **2017,** *2* (8), 4911-4919.
16. Lee, K.-U.; Byun, J. Y.; Shin, H.-J.; Kim, S. H., A high-performance supercapacitor based on polyaniline-nanoporous gold. *Journal of Alloys and Compounds* **2019,** *779*, 74-80.
17. Shen, S. Y.; Zhao, T. S.; Xu, J. B.; Li, Y. S., Synthesis of PdNi catalysts for the oxidation of ethanol in alkaline direct ethanol fuel cells. *Journal of Power Sources* **2010,** *195* (4), 1001-1006.
18. Yazdan-Abad, M. Z.; Noroozifar, M.; Alfi, N., Investigation on the electrocatalytic activity and stability of three-dimensional and two-dimensional palladium nanostructures for ethanol and formic acid oxidation. *Journal of Colloid and Interface Science* **2018,** *532*, 485-490.
19. Kim, S. H., Nanoporous Gold Films as Catalyst. In *Catalytic Application of Nano-Gold Catalysts*, IntechOpen: 2016.
20. Xu, J. B.; Zhao, T. S.; Shen, S. Y.; Li, Y. S., Stabilization of the palladium electrocatalyst with alloyed gold for ethanol oxidation. *International Journal of Hydrogen Energy* **2010,** *35* (13), 6490-6500.
21. Lee, K.-U.; Byun, J. Y.; Shin, H.-J.; Kim, S. H., Nanoporous gold-palladium: A binary alloy with high catalytic activity for the electro-oxidation of ethanol. *Journal of Alloys and Compounds* **2020,** *842*, 155847.
22. Liu, J.; Luo, Z.; Li, J.; Yu, X.; Llorca, J.; Nasiou, D.; Arbiol, J.; Meyns, M.; Cabot, A., Graphene-supported palladium phosphide PdP2 nanocrystals for ethanol electrooxidation. *Applied Catalysis B: Environmental* **2019,** *242*, 258-266.
23. Alfi, N.; Yazdan-Abad, M. Z.; Rezvani, A.; Noroozifar, M.; Khorasani-Motlagh, M., Three-dimensional Pd-Cd nanonetwork decorated on reduced graphene oxide by a galvanic method as a novel electrocatalyst for ethanol oxidation in alkaline media. *Journal of Power Sources* **2018,** *396*, 742-748.
24. Geraldes, A. N.; da Silva, D. F.; Pino, E. S.; da Silva, J. C. M.; de Souza, R. F. B.; Hammer, P.; Spinacé, E. V.; Neto, A. O.; Linardi, M.; dos Santos, M. C., Ethanol electro-oxidation in an alkaline medium using Pd/C, Au/C and PdAu/C electrocatalysts prepared by electron beam irradiation. *Electrochimica Acta* **2013,** *111*, 455-465.
25. Hong, W.; Wang, J.; Wang, E., Facile Synthesis of Highly Active PdAu Nanowire Networks as Self-Supported Electrocatalyst for Ethanol Electrooxidation. *ACS Applied Materials & Interfaces* **2014,** *6* (12), 9481-9487.
26. Feng, Y.-Y.; Liu, Z.-H.; Xu, Y.; Wang, P.; Wang, W.-H.; Kong, D.-S., Highly active PdAu alloy catalysts for ethanol electro-oxidation. *Journal of Power Sources* **2013,** *232*, 99-105.
27. Chang, C.-M.; Hsieh, M.-T.; Kang, W.-C.; Whang, T.-J., Study of the Co-Electrodeposited Pd-Ni Alloy Thin Film and Its Performance on Ethanol Electro-Oxidation. *Journal of The Electrochemical*

Society **2014,** *161* (10), D552-D557.

28. Rostami, H.; Rostami, A. A.; Omrani, A., Investigation on ethanol electrooxidation via electrodeposited Pd–Co nanostructures supported on graphene oxide. *International Journal of Hydrogen Energy* **2015,** *40* (33), 10596-10604.
29. Huang, Y.; Guo, Y.; Wang, Y.; Yao, J., Synthesis and performance of a novel PdCuPb/C nanocatalyst for ethanol electrooxidation in alkaline medium. *International Journal of Hydrogen Energy* **2014,** *39* (9), 4274-4281.
30. Xu, C. W.; Wang, H.; Shen, P. K.; Jiang, S. P., Highly Ordered Pd Nanowire Arrays as Effective Electrocatalysts for Ethanol Oxidation in Direct Alcohol Fuel Cells. **2007,** *19* (23), 4256-4259.
31. Lv, H.; Wang, Y.; Lopes, A.; Xu, D.; Liu, B., Ultrathin PdAg single-crystalline nanowires enhance ethanol oxidation electrocatalysis. *Applied Catalysis B: Environmental* **2019,** *249*, 116-125.
32. Wittstock, A.; Biener, J.; Bäumer, M., Nanoporous gold: a new material for catalytic and sensor applications. *Physical Chemistry Chemical Physics* **2010,** *12* (40), 12919-12930.

CHAPTER 6
SUPPLEMENTARY INFORMANTION

6.1 Nanoporous gold from Au-Ag, Au-Si, and Au-Mg

We fabricated nanoporous gold(NPG) with Au-Ag, Au-Si, and Au-Mg. We took SEM images of each samples for comparison. Figure 6.1 shows the SEM images of Au-Ag alloy and NPG. The typical sputtered structures with small grains are observed in figure 6.1 (a). Figure 6.1 (b) shows the cross sectional SEM image of Au-Ag alloy and columnar grains with thickness of ~ 200 nm are observed. Figure 6.1 (c) and (d) show NPG from Au-Ag alloy with concentrated nitric acid. This NPG is widely and typically used in many reserch group. The size of ligaments and pores are around ~ 100 nm. We can observe the curved ligaments and smooth ligament surfaces.

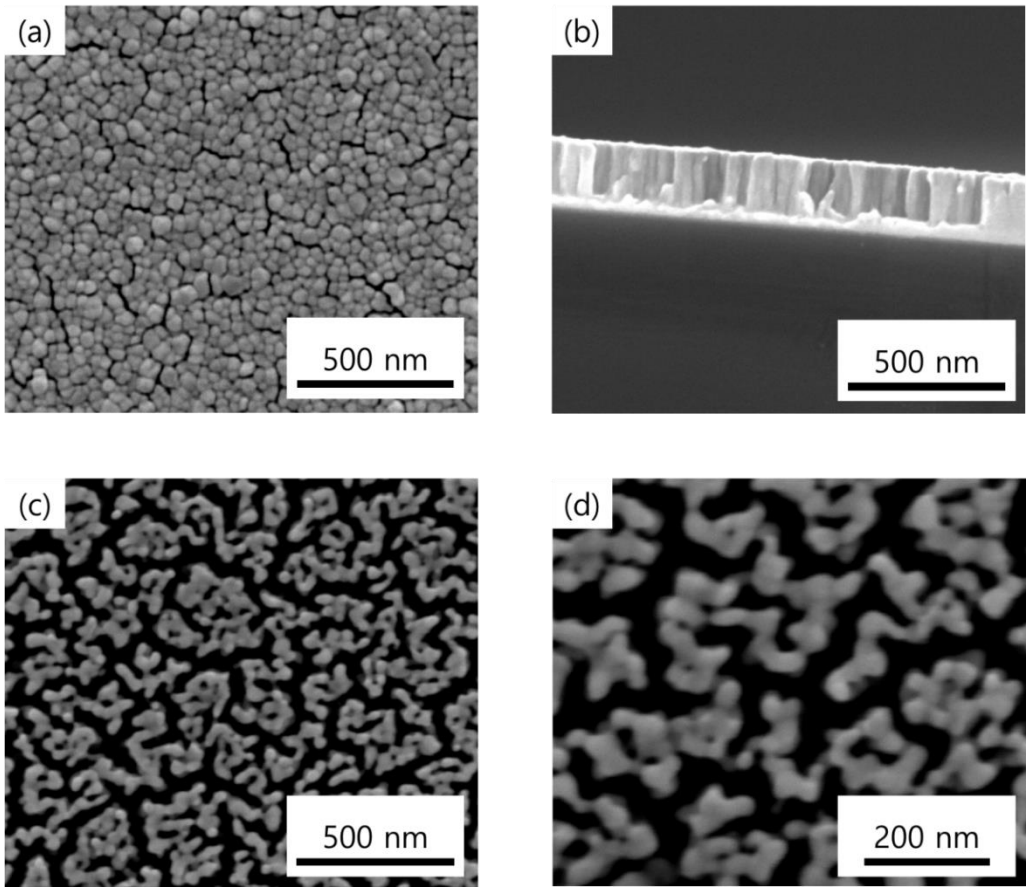

Figure 6.1. SEM imgaes of Au-Ag alloy and NPG from Au-Ag alloy. (a) Top view and (b) Cross sectional view of Au-Ag alloy. (c) NPG from Au45Ag55 (d) High resolution of (c).

The Au-Si alloy and NPG from Au-Si are shown in figure 6.2 (a) and (b), respectively. The Au-Si alloy was dealloyed by 30 wt% of potassium hyderoxide solution of 50°C for 2 h 30 min. The size of ligaments, holes, and overall shapes are very similar to Au-Ag systems. However, we can observe the different shapes in NPG from Au-Mg alloy (figure 6.3). The Au-Mg alloy was dealloyed by 5 wt% acetic acid in room temperature for 30 min. The SEM image of alloy is almost same while the ligaments in NPG are angled. We speculate that these discrepancy is mainly due to the alloy phases. Figure 6.4 shows the phase diagrams of Au-Ag, Au-Si, and Au-Mg. The Au-Ag system is a solid solution, Au-Si system is a simple eutectic, while Au-Mg system has a number of solid phases. In case of Au-Ag and Au-Si, the sacrificial elements are atomically dissolved from the alloy, however, in Au-Mg system, grains will be dissolved so that NPG from Au-Mg has angled ligaments. In case of Au-Mg system, though there are several intermetallic compounds in Au-Mg phase diagram, the magnesium was always easily dissolved in diluted acetic acid (part 4, part5). We believed that the magnesium is an excellent sacrifical element and it is applicable to other alloy systems.

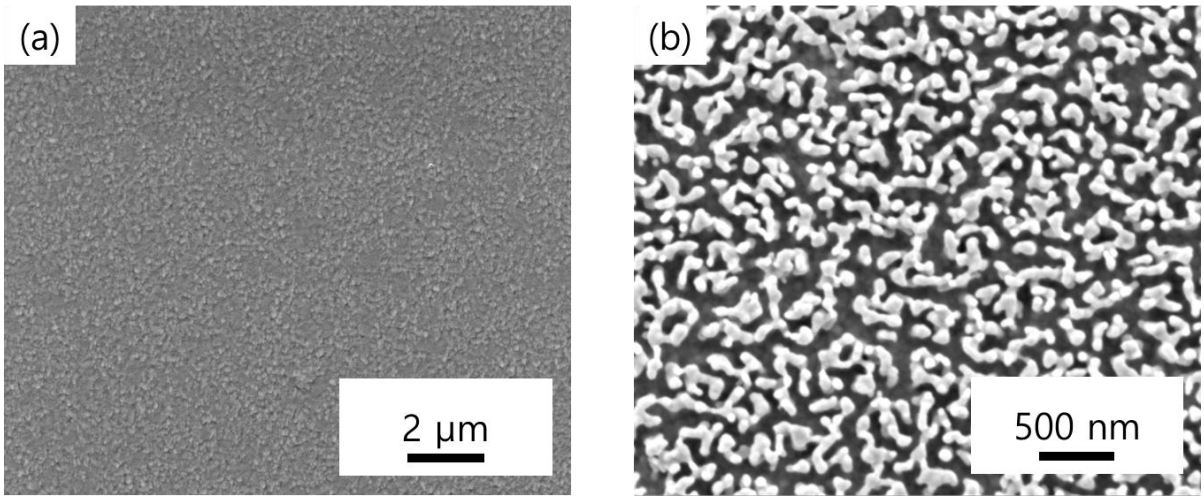

Figure 6.2. SEM images of Au-Si alloy and NPG from Au-Si

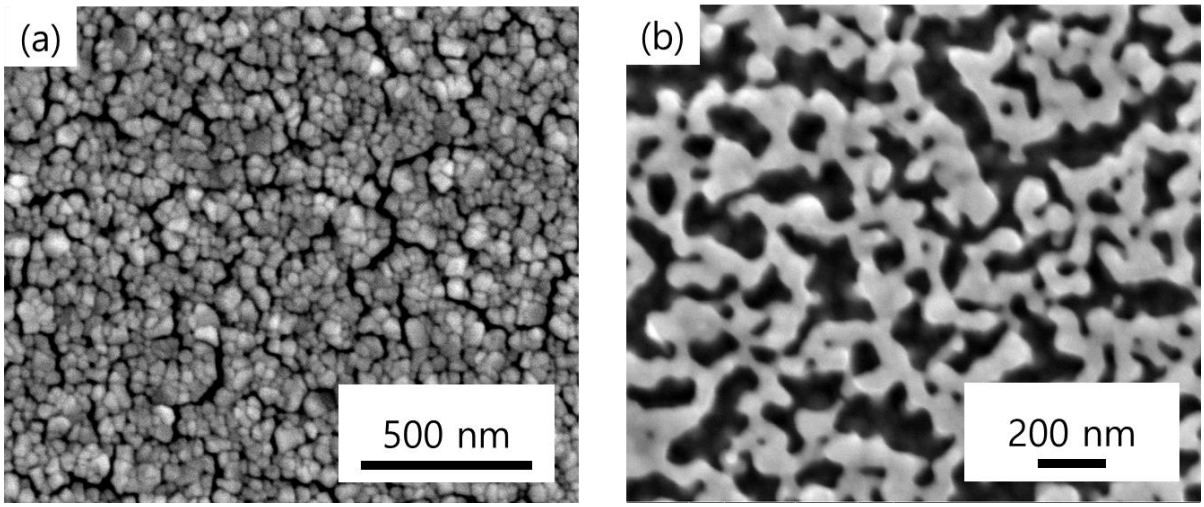

Figure 6.3. SEM images of Au-Mg alloy and NPG from Au-Mg

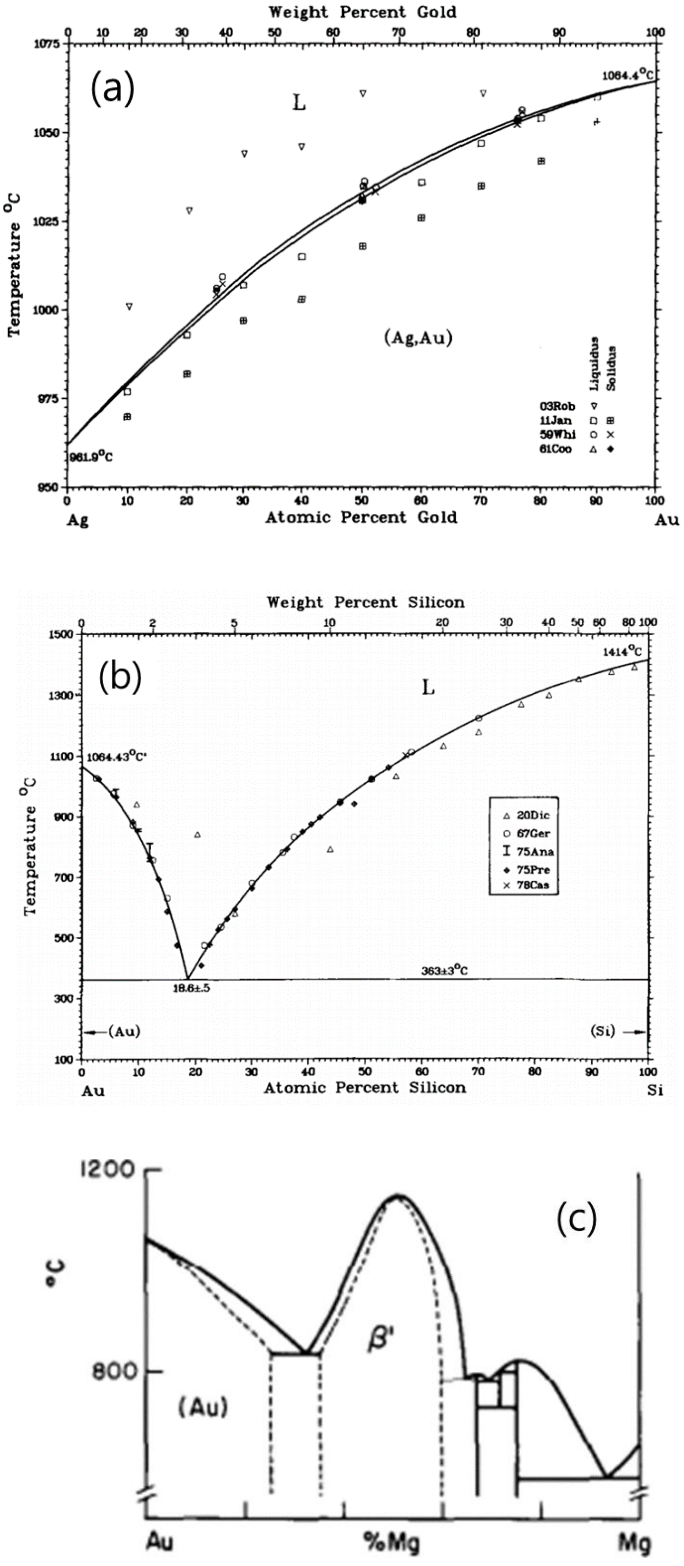

Figure 6.4. Phase diagrams of (a) Au-Ag system[1], (b) Au-Si system[2], and (c) Au-Mg system[3]

6.2 Cyclic voltammtery for nanoporous structures

During the cyclic voltammtery(CV), the surface atoms are oxidized and reduced because of the applied volatge. Figure 6.5 shows cyclic voltammogram of NPG in 0.5 M sulfuric acid with scan rate of 100 mV/s. In forward scan, the multiple oxidation peaks are observed, while only one huge reduction peak is observed in backward scan. Because the shape of this reduction peak is simple and easy to calcuate the area of peak, it is used to estimate the surface area by dividing the area of reduction peak of flat gold, which is roughness factor. Typically, 450 μc/cm^2 is used for reference.[4] Generally, our NPG samples show the roughness factor as around 30.

In addition, the CV affct the nanoporous structures. During the redox process, the gold atoms will be rearranged and it can change the structures. Figure 6.6 shows NPG from Au-Mg before and after CV. It can be seen that the angled structureswas changed to curved structures by CV. We speculate that during the CV, low-coordinated atoms prefer to aggregate themselves and overall strcutres were changed. Indeed, Ming et al. reported that they could change the surface facet of NPG by CV and enhance the catalytic activity by increasing the facet which is more active for chemical reactions.[5] However, we could not observe the dramatic increasement of catalytic activity by tunning the surface facet.

Besides, we can test its strctural staiblity by consecutive CV. The structure of NPG would be gradully collapse due to the successive redox reaction. NPG with small ligaments will collapse rapidly and show fast decreasing peaks of oxidation and reducion while large ligament NPG will collapse relatively slowly. Comparing the first and 100 cycles or recording the cyclic numbers up to reduction area of 50 %, we can compare the stability of each nanoporous structures. Figure 6.7 shows the comparision of first cycle and 101th cycle of cyclic voltammogram of NPG-palladium in 1 M potassium hydroxide containing 1 M ethanol. We could observed that the peak current is decrased in 101th cycle. Comparing the peak current, we could estimate the stability of our NPG palladium structures.

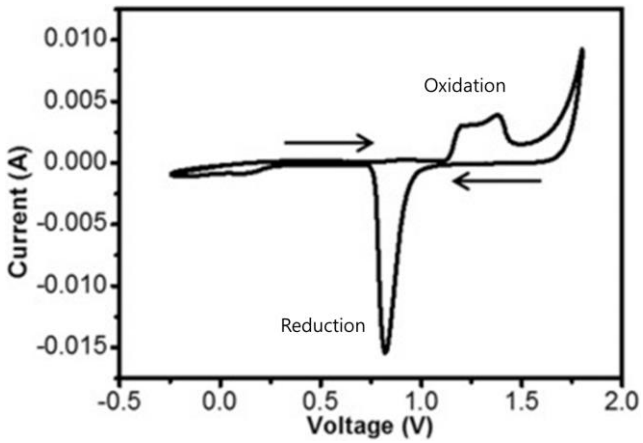

Figure 6.5. Cyclic voltammogram of NPG in 0.5 M H_2SO_4 with scan rate of 100 mV/s

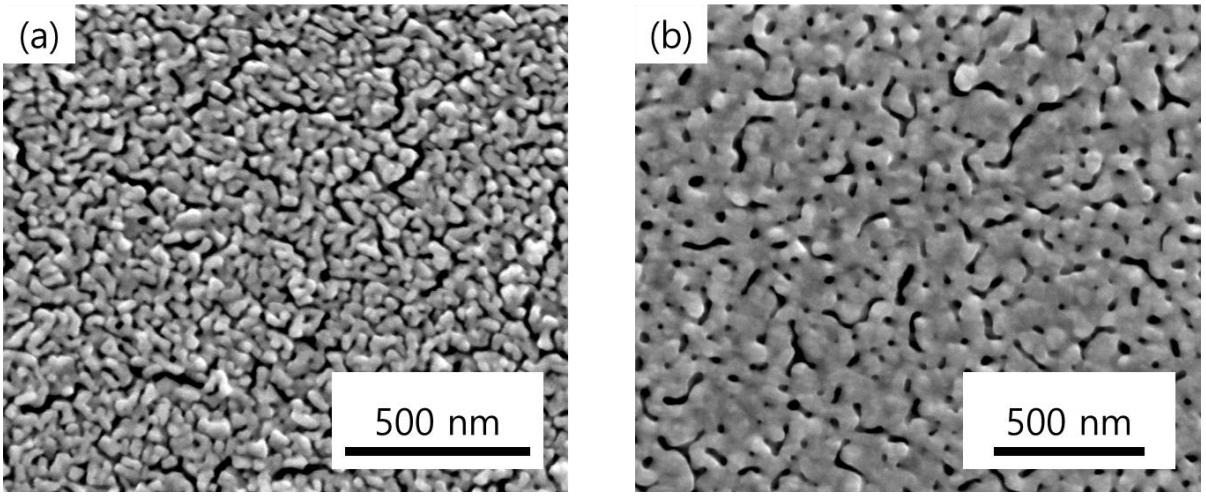

Figure 6.6. SEM images of NPG from Au-Mg. (a) Before CV and (b) after CV

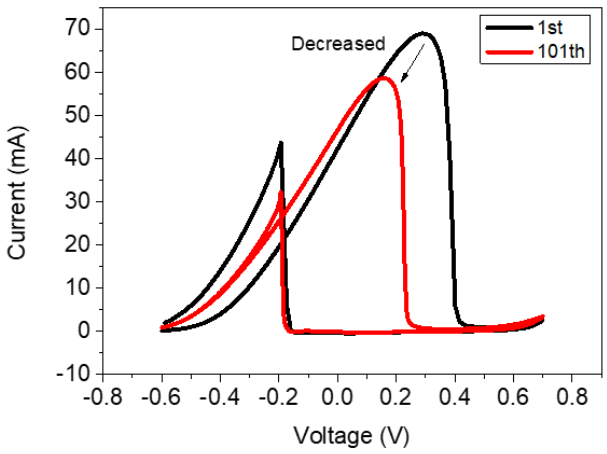

Figure 6.7. Comparison of 1st cycle and 101th cycle of cyclic voltammogram of NPG palladium in 1 M potassium hydroxide containing 1 M ethanol solution.

6.3 Tuning the facet of nanoporous gold

As mentioned above, Ming et al. reported that the catalytic activity of NPG(from Au-Ag alloy) toward electro oxidation of ethanol in alkaline media was enhanced by tunning the surface factet.[5] Using underpotential deposition(UPD) of lead in an alkaline media, we can precisely identify different surface facet of electrode.[5-7] We conducted the same experiment with our NPG sample from Au-Mg alloy and compared(We also made NPG from Au-Ag for the reference). The UPD was conducted in 0.1 M NaOH containing 1 mM $Pb(NO_3)_2$ solution with scan rate of 50 mV/s. The voltage range was –0.7 V to 0.2 V vs Ag/AgCl. According to the references, the peak current at –0.61 V, –0.5 V, –0.45 V, and –0.31 V are corresponding to kink and step(KS) sites, (111) facet, (100) facet, and (110) facet, respectively.[5-7]

We made and compared three samples of NPG from Au_{40}-Ag_{60}, and Au_{20}-Mg_{80} as an as dealloyed sample, annealed sample(100°C oven, 20h), and after slow CV sample(in H_2SO_4 solution, 10 cycles, 5 mV/s). We took SEM images of these samples(figure 6.8) however, we could not find any significant differece in features. Figure 6.8 shows the UPD results, CV and chrono amperometry(CA) results for ethanol oxidation. In as dealloyed sample,abundant KS sites are observed and after slow CV, the KS sites decreased and (110) facet increased. After annealing, we could not find any peaks(figure 6.9 (a)). The CV results in alkaline media(figure 6.9 (b)) show that the slow CV sample has the highest current density while annealed sample has the lowest current density. We could observe the same tendency in CA results(figure 6.9 (c)). In case of NPG from Au-Mg(figure 6.10), high peak at (100) facet and little peak at KS sites are observed in as dealloyed sample. After annealing, only one broad peak is observed, indicating (111) facet. Suprisingly, we could not detect any peak in slow CV sample. The CV and CA results showed that the catalytic activity for the electrooxidation of ethanol decreases in the following order: As dealloyed > Annealed > Slow CV. It has been reported that the catalytic activity of gold for electrooxidation of ethanol in alkaline media is sensitive to surface facet and follows the order: (110) > (100) > (111)[8], which is coincide with our CV and CA retults. It is noticable that NPG from Au-Mg has a number of (100) facet without any treatment while NPG from Au-Ag has (100) facet after slow CV. We speculate that this is mainly due to the alloy phases(figure 6.4). Further research is need and this topic will be an important key for enhancing the catalytic activity of NPG.

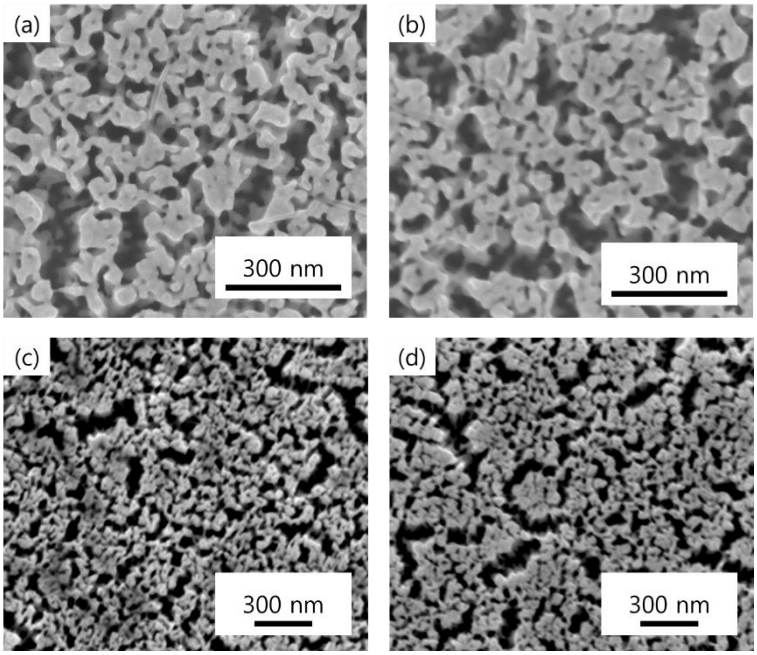

Figure 6.8. SEM images of NPG (a) As dealloyed from AuAg (b) Annealed from AuAg (c) As dealloyed from AuMg (d) Annealed from AuMg

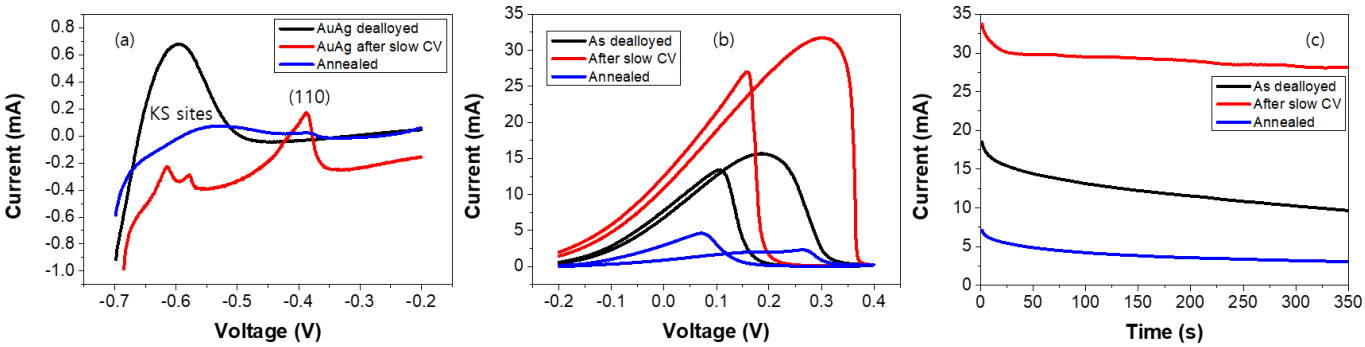

Figure 6.9. Electrochemical properties of NPG from Au-Ag. (a) UPD profiles, (b) CV, and (c) CA results of electrooxidation of ethanol

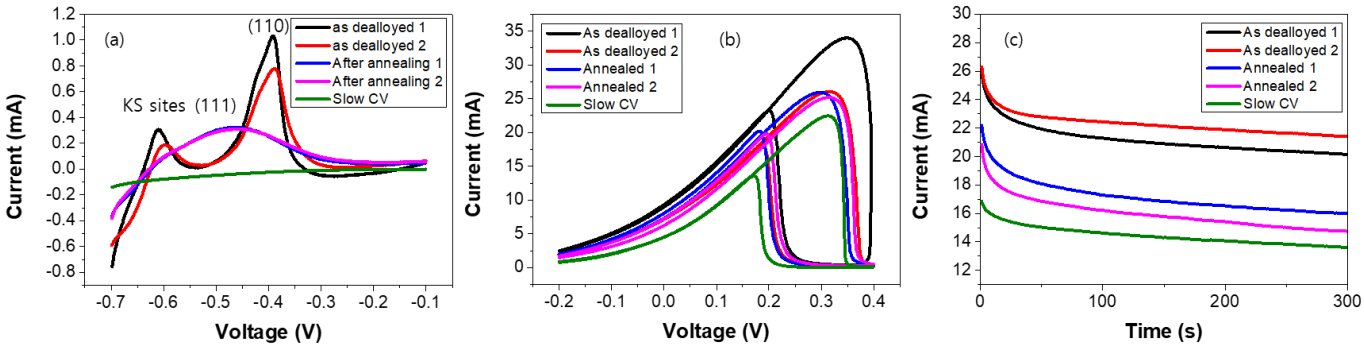

Figure 6.10. Electrochemical properties of NPG from Au-Mg. (a) UPD profiles, (b) CV, and (c) CA results of electrooxidation of ethanol

6.4 References

1. Okamoto, H.; Massalski, T. B., The Ag−Au (Silver-Gold) system. *Bulletin of Alloy Phase Diagrams* **1983,** *4* (1), 30.
2. Okamoto, H.; Massalski, T. B., The Au−Si (Gold-Silicon) system. *Bulletin of Alloy Phase Diagrams* **1983,** *4* (2), 190-198.
3. Kogachi, M., Alloying behaviors of Ag−Mg, Au−Mg and Ag−Al alloys. *Journal of Physics and Chemistry of Solids* **1974,** *35* (1), 109-115.
4. Tan, Y. H.; Davis, J. A.; Fujikawa, K.; Ganesh, N. V.; Demchenko, A. V.; Stine, K. J., Surface area and pore size characteristics of nanoporous gold subjected to thermal, mechanical, or surface modification studied using gas adsorption isotherms, cyclic voltammetry, thermogravimetric analysis, and scanning electron microscopy. *Journal of Materials Chemistry* **2012,** *22* (14), 6733-6745.
5. Wang, Z.; Ning, S.; Liu, P.; Ding, Y.; Hirata, A.; Fujita, T.; Chen, M., Tuning Surface Structure of 3D Nanoporous Gold by Surfactant-Free Electrochemical Potential Cycling. **2017,** *29* (41), 1703601.
6. Hebié, S.; Cornu, L.; Napporn, T. W.; Rousseau, J.; Kokoh, B. K., Insight on the Surface Structure Effect of Free Gold Nanorods on Glucose Electrooxidation. *The Journal of Physical Chemistry C* **2013,** *117* (19), 9872-9880.
7. Hernández, J.; Solla-Gullón, J.; Herrero, E., Gold nanoparticles synthesized in a water-in-oil microemulsion: electrochemical characterization and effect of the surface structure on the oxygen reduction reaction. *Journal of Electroanalytical Chemistry* **2004,** *574* (1), 185-196.
8. Beyhan, S.; Uosaki, K.; Feliu, J. M.; Herrero, E., Electrochemical and in situ FTIR studies of ethanol adsorption and oxidation on gold single crystal electrodes in alkaline media. *Journal of Electroanalytical Chemistry* **2013,** *707*, 89-94.

CHAPTER 7
CONCLUSION AND SUGGESTIONS

In this thesis, we address the nanoporous gold and its electrochemical applications. The sputtering system is suitable for making an alloy precursor. Our delloying method which uses potassium hydroxide solution and diluted acetic acid is not only effective but also environmentally friendly. We developed the adhesion between a glass substrate and a titanium adhesion layer by annealing treatment. In this way, we made nanoporous gold film on a glass substrate and applied it to the electrochemical sensor for aniline. Also, we applied the nanoporous gold as a supercapacitor by homogeneously coating a few nanometers of polyaniline on the nanoporous gold. Because nanoporous gold has high conductivity and great stability, we could make high performance superacapacitor. Furthermore, we also prepared binary nanoporous structures for electro-catalyst. Basically, nanoparticles have been used for electro-catalyst, however, they should be fixed on the conducting substrate (e.g. glassy carbon electrode), so that they suffer from aggregation, leaching, and contact resistance between nanoparticles and substrates. The nanoporous structures are free to aggregation and leaching, and it has one-body nature so that there is no contact resistance. The bimetallic catalysts have been developed in various types of nanoparticles. In present study, we made binary nanoporous structures from ternary alloy of gold, palladium, and magnesium to overcome the drawbacks of nanoparticles. Moreover, these nanoporous structures can directly be used as a working electrode in electrochemical system. The magnesium in ternary alloy is very important because it has tendency to be dissolved easily in diluted acetic acid even it makes intermetallic compound with gold or palladium. We could make nanoporous gold palladium and it showed high electrochemical catalytic activity toward ethanol oxidation reaction in alkaline media.

A lot of topics related to nanoporous gold have been extensively researched such as finding reaction sites in nanoporous gold, tuning the facets of nanoporous gold for enhancing the catalytic activity, investigating the effect of residual silver, tuning the mechanical properties, etc. Our co-sputtering method can easily adjust the composition of an alloy precursor so that it is suitable for investigating the composition effect. In addition, the mechanical properties of nanoporous gold highly depend on the microstructures. We could easily control the microstructures of nanoporous gold by adjusting the composition of the sacrificial elements. Moreover, not only gold based material, silver, copper, nickel, and other metals can be made as nanoporous structure by our method. These materials also can be applied to anywhere. Besides, the bimetallic catalysts recently have attracted huge attention in extensive applications due to their tunable composition and properties. We already showed that nanoporous gold palladium was successfully fabricated with tunable composition and high stability. It can be applied to

other bimetallic catalysts with designed composition and desired properties.

We suggest that combining the nanoporous gold with other funtional nanoparticles (e.g. TiO_2, CoOx, etc.) will be an interesting topics for enhancing the potentials of nanoporous gold. As gold is very expensive materil, finding an alternative material (copper, silver, etc.) could be a good topic. Furthermore, the various combination of binary alloy with nanoporous structures can be easily fabricated and it will be a compelling subject.

감사의 글

아무것도 모르는 저를 가르치시고, 마음껏 연구할 수 있는 기회를 주신 신형준 교수님께 깊은 감사와 존경의 말씀을 드립니다. 연구에 대한 깊고도 날카로운 통찰과 예리한 직관으로 항상 핵심적인 부분들을 짚어 지도해 주시고 연구 외 다른 부분들까지 섬세하게 배려해주신 덕에 졸업을 할 수 있었습니다. 아직 부족한 부분들이 많지만 교수님께서 알려주신 것들을 더욱 갈고 닦아서 훌륭한 연구자가 되겠습니다. KIST 에서 연구할 수 있도록 도와주시고 지도해주신 김상훈 박사님께도 깊은 감사의 말씀을 드립니다. 제가 계획하고 말씀드리는 것들을 항상 긍정적으로 생각해 주시며 지원해주시고, 연구에 대한 아이디어를 발전시키고 응용하는데 큰 도움을 주셨습니다. 그리고 언제나 인자한 미소로 "잘 되어가냐" 라고 물어 보시며 격려와 조언을 아끼지 않으신 변지영 박사님께도 깊은 감사를 드립니다. 또한, 논문 디펜스의 심사위원으로 좋은 말씀들을 해주신 유정우 교수님과 이종훈 교수님께도 감사를 드립니다.

학부생때부터 대학원에 대한 꿈을 꾸게 해주셨던 창원대학교 이 웅 교수님과 대학원 입학에 여러 가지 조언을 주신 재료연구소 강주희 박사님 에게도 깊은 감사를 드립니다. 또한, 실험실 생활에 대한 전반적인 것들을 알려주었을 뿐 아니라 인생에 대한 조언까지 해주신 선배 정민복 박사님, 같이 연구하며 많은 이야기를 나누고 서로 돕고 도왔던 Rahman 박사님, 최윤정, 영문 작성에 도움을 준 Eunike 에게도 감사의 인사를 전합니다.

6 년이라는 긴 시간 동안 항상 응원하고 지원해주며 기다려 주셨던 가족들에게도 감사의 인사를 전합니다. 그리고 언제나 좋은 말씀과 따뜻한 격려를 해주셨던 남포교회 윤철규 목사님과 철없는 동생을 잘 달래며 응원해주신 남포교회 장나라 형님, 정 한 형님, 그리고 여러 남포교회 지체들에게도 깊은 감사의 말씀을 드립니다.

마지막으로 이 모든 것들을 계획하시고 주관하시며 저를 이 자리까지 이끄시고 앞으로도 이끌어 가실, 시간 속에서 일하시는 살아계신 우리 주 하나님께 모든 영광과 찬송을 드립니다.